Spring 5-15-2016

The Murine Accessory Olfactory Bulb as a Model Chemosensory System: Experimental and Computational Analysis of Chemosensory Representations

Gary Francis Hammen
Washington University in St. Louis

WASHINGTON UNIVERSITY IN ST. LOUIS

Division of Biological and Biomedical Sciences
Neurosciences

Thesis Examination Committee:
Timothy E. Holy, Chair
Paul A. Gray
Daniel Kerschensteiner
Steven J. Mennerick
Baranidharan Raman
Bradley L. Schlaggar

The Murine Accessory Olfactory Bulb as a Model Chemosensory System: Experimental and Computational Analysis of Chemosensory Representations

by
Gary Francis Hammen

A dissertation presented to
the Graduate School of Arts and Sciences
of Washington University in
partial fulfillment of the
requirements for the degree of
Doctor of Philosophy

May 2016
St. Louis, Missouri

Table of Contents

List of Figures

List of Tables

Acknowledgments

Explicitly, I would like to acknowledge both human body donors to the Anatomy and Neurobiology human anatomy program and the large number of laboratory animals that have been an integral part of advancing my own personal understanding of biological and neural organization and function.

Timothy E. Holy, Ph.D., was an exceptional mentor who willing took on a student with very modest computational experience and let that student roam as freely and as far as he so desired. I still have his copy of Numerical Recipes and continue to appreciate what I learned during my time in his lab.

The Thesis Committee, Steven J. Mennerick, PhD, Bradley L. Schlaggar, M.D., Ph.D., Paul A. Grey, Ph.D., Daniel Kerschensteiner, M.D., and Barani Raman, Ph.D., who have all contributed great ideas, challenging discussion, and important feedback or training at different times.

Julian Meeks, Ph.D., was a wonderful collaborator and impromptu mentor for many different things.

Xiaoyan Fu, Ph.D., contributed support, advice, and help with mass spectrometry and steroid chromatography.

This work was supported by National Institutes of Health, National Institute for Deafness and Communication Disorders, Awards F30 DC011673 (Hammen GF), F32DC009352 (Meeks JP), K99/R00DC011780 (Meeks JP), R01DC010381 (Holy TE), R01NS068409 (Holy TE), and National Science Foundation IGERT: Cognitive, Computational, and System Neuroscience Award DGE-0548890 (Hammen GF).

Gary Francis Hammen

Washington University in St. Louis

May 2016

Dedications

To my family, both born and acquired: you have taught me how to work hard, how to beat my head against the wall, and to try, at least occasionally, to recognize the difference.

To my daughter Ashlyn, who has, through no yet to be determined fault of her own, been subjected to each step of my educational. These have involved absences, both physical (my tour in the Army) and mental (my occasional, near manic pursuit of some particular minutia).

To my wife, Alecia Vogel-Hammen, a gifted physician scientist, a wonderful companion, and clever conversation all wrapped up neatly in one. She has supported me and engaged with my ideas throughout the course of my time in the Neuroscience Program. I have to credit her intense passion for the brain as inspiring my own during the times in which it waned.

ABSTRACT OF THE DISSERTATION

The Murine Accessory Olfactory Bulb as a Model Chemosensory System: Experimental and Computational Analysis of Chemosensory Representations

by

Gary Francis Hammen

Doctor of Philosophy in Biological & Biomedical Sciences

Neurosciences

Washington University in St. Louis, 2016

Professor Timothy E. Holy, Chair

A common challenge across sensory processing modalities is forming meaningful associations between the neural responses and the outside world. These neural representations of the world must then be integrated across different sensory systems contributing to each individual's perceptual experience. While there has been considerable study of sensory representations in the visual system of humans and multiple model organisms, other sensory domains, including olfaction, are less well understood. In this thesis, I set out to better understand the sensory representations of the mouse accessory olfactory system (AOS), a part of the olfactory system. The mouse AOS, our model chemosensory system, comprises peripheral vomeronasal sensory neurons (VSNs), the accessory olfactory bulb (AOB), and downstream effectors. Our work describes the neural representations of multiple sensory inputs in the AOS, specifically the representations of odorants in high dimensional chemical sensory space in the AOB, and how these representations are shaped by interactions within the circuit. Given the complex nature of olfactory chemosensory representations, the features of our model system may give new perspectives on the neural representation of the outside world.

In a neural representation of olfactory information, both the interactions between each receptor and odor compounds as well as the circuit mediated interactions could potentially affect the neural representations of the outside world. The initial neural response comprises component interactions between each receptor and the odor; chemical signals must interact with physical receptors. However, chemosensory processing, such as olfaction, requires interpreting a large variety of potentially overlapping chemical cues from the environment with only a finite number of receptor types. This means that each chemical cue does not necessarily activate only one receptor type or region of the circuit, but rather the cue is likely to be represented by multiple receptor and odor component interactions. Also, the component parts of odors may be processed differently when presented in isolation versus in a more complex mixture, thus allowing the response to a particular odor to vary with chemical context. Moreover, once these component representations exist, interactions within the neural circuit may further shape these responses. For example, one might expect component parts of a complex odor to specifically inhibit other component parts. In the case of the accessory olfactory system this inhibition could be at the receptor level or at the level of the sensory representation in the accessory olfactory bulb (AOB).

In Chapter 3, I describe the overall organization of chemosensory representations in the accessory olfactory bulb (AOB), which is found to be a modular map in which the primary associations of functional sensory responses are spatially organized relative to one another. I find these primary associations are condensations of the first order sensory neuron axon terminals, which form population response pooling structures called glomeruli. In these glomeruli, similar response types from those sensory neurons expressing one of the approximately 300 receptor types in the vomeronasal organ (VNO) co-converge. One purpose of converging inputs of neurons expressing the same receptor is likely to minimize noise, and I demonstrate that pooling of like receptor responses into glomeruli does increase neural signal relative to noise. However, I also observed a modular organization among and between glomeruli in which certain types or patterns of chemosensory responses are always spatially adjacent to one another, while others are much farther apart than would be expected by chance. I found this spatial modularity for both ethological stimuli (urine

collected from conspecifics with widely divergent physiological endocrine status) and individual sulfated steroids.

In Chapter 4, I explore the consequences of changing sensory context, specifically the presentation of multiple compounds, and the role that inhibition plays in the neural representation of the sensory stimuli. First, I tested whether the circuit responds differently to demands to represent a single odor than to demands to represent multiple odors by using odors that activate glomeruli both inside and outside of modules. I found that responses to mixtures rapidly diverge from the responses of individual component parts. Moreover, there was an effect of inhibition in modulating the response to preferred stimuli in all glomeruli. However, initial analysis of one type of pregnanolone responsive glomeruli demonstrated that the divergent response to mixtures in this type of glomerulus was not mediated by inhibition at the glomerular level, but was rather attributable to bottom-up effects from the interactions of multiple ligands with chemosensory receptors in the VNO. Nonetheless, I also demonstrated that in the AOB, the axon terminals of the same sensory neurons (glomeruli) are organized into modules that allow for feedback inhibition. Significant ionotropic glutamate receptor signal modulation was observed within modules, demonstrating that there are inhibition mediated effects in the representation of complex mixtures when glomeruli are co-locally arranged. Specifically, at both the level of the VSNs and also in AOB glomeruli, the response to allopregnanolone sulfate is inhibited by co-presentation with estradiol sulfate. This both significantly increases the relative representation of estradiol sulfate and shifts representation of allopregnanolone primarily within modules. These types of context dependent interactions depend on the spatial organization described in Chapter 3 as well as mixture context, and have the potential to optimize the representation of some chemical cues in a context specific manner.

Chapter 1

Introduction

"The brain is not an organ for representing truth: the brain is an organ for survival."

Charles Zorumsky, MD

Samuel B. Guze Professor of Psychiatry and Professor of Neurobiology
Head of the Department of Psychiatry at Washington University in Saint Louis

Remark from a presentation at the annual Neuroscience Retreat,

Pere Marquette Lodge, Grafton, IL, September 27, 2013.

The olfactory system is one of the chemical senses. The components of the system allow the brain to acquire and represent chemical information from the outside world. Like all information gathered by the nervous system we presume that the information is used to guide or modify some behavior.

The mechanism of neural modification are many. One basic physiological example is the physical stretch receptors in the lungs [13] form an integral negative feedback loop that modifies

breathing [67].[1] Conversely, the breathing rate is increased by chemosensation of increased carbon dioxide levels in the blood drive the rate of breathing to increase (reviews[34, 101]).

Another example, more reflective of olfactory connections to the limbic system, is that the olfactory detection of androstadienone, a steroid metabolite in humans, seems to have a number of potential effects on behavior. The odorant has been reported to increase circulating cortisol (another steroid hormone), bias the visual perception of masculinity and femininity, and increase activity in the hypothalamus [108, 117, 15]. Variability in ability to detect the odor appears dependent on which genetic variants of a single odor receptor is present in an individual [51].

However, though there is a clear connection between chemical stimulation of receptors and odor detection, it should be noted that this still only results in the perception of a smell, which is then leading to behavior. By analogy, it may seem that inquiring into how one smell or odorant is different from another is akin to asking how hot is different from cold– intuitively different perceptions. Yet when olfaction is coincident with taste (bitter, sour, salty, sweet, and umami), the perception is indelibly altered (at least in those who are not actively thinking about the neurobiology [81]), though as an aside even this basic conception is more complicated than initially believed, with at least twenty-five bitter receptors now known [7]. Indeed, the more philosophical among us may expound ad nauseum upon why one odor "is" different from another, or hot from cold, or red from green, but those differences are a perception. It is those differences in perception, though, that underscore neurobiological origin of perception. In vision the ability to discriminate the broad palette of colors, tones, and features experienced in our lives begins in the retina of the eye with essentially three color receptors: red, green, and blue. In people missing one of those receptors, a form of color blindness results. A simple, relatively common, single gene example of this is red-green color blindness.

Similarly, taste provides an interesting example of known neurobiological origins of the chemical senses, though there has been divergence from model organisms such as rodents to humans. In

[1]Vagal afferent nerves to the nucleus of the solitary tract (NST) generate dual negative feedback via NST inhibitory cells which synapsing onto both parasympathetic nervous system efferents in the nucleus ambiguous and efferent somatic motor neurons in the nucleus paraambiguous[94, 84, 99, 74].

the rat, after forming synapses in the nucleus of the solitary tract (NTS), neurons carry the sensory representation to the parabrachial nucleus (PBN), after which the signals bifurcate, being directed to ventral forebrain structures and the other through the parvocellular ventral posterior medial nucleus of the thalamus (VPM) and on to insular gustatory regions. In humans projections from NST bypass the PBN and go directly to the thalamus and on to gustatory cortex [78]. Despite these differences, the model systems have continued to provide both new information, even in the most basic terms of discovering the aforementioned many bitter tastant receptors, as well as checks on hypotheses of neural function and organization.

Measuring Olfactory Space

Interestingly, while there is some known about the taste system, as described above, and a considerable amount known about the visual system, there is comparatively less known about the olfactory system. For simplicity, I am predicating that statement on the relative number of receptors in each system, but there are also significantly divergent views on the constraints limiting utilization of olfactory information (see[111, 87, 53]). Thus, the topic of how we should measure olfaction and how to interpret those measurements is germane to understanding chemical sensation, neural circuits, and in general the brain/behavior relationship.

While I performed all of my experiments and analyses in a specialized part of the mouse olfactory system called the accessory olfactory system, we shall, for the initial discourse, place the accessory olfactory system and the main olfactory system together and refer to them generically as olfaction.

If I were to naively construct a space for olfaction, similar to the red/green/blue space for vision, then I might want to consider the number of receptors used to detect airborne volatile chemicals and the ligands for many of these receptors. In the human, one recent estimate of the number of genetic loci for human olfactory receptors is 413 [72].

However, as further detailed in that estimate [72], olfactory receptors are thought to be expressed at a the level of single allele via a process of allelic exclusion. This process would then

technically allow for upwards of 826 individual olfactory receptors (ORs) within each individual. The actual detected upward limit was 600 allelic variants, but this is further complicated by the finding of up to 271 of 413 intact OR loci being affected by nonfunctional single nucleotide polymorphisms and copy number variants, resulting in even higher diversity. For comparison to other olfactory systems, the mouse main and accessory olfactory system appear to contain, respectively, about 1000 receptors and about 300 receptors [14, 79, 9]. I will not dwell on comparisons of spatial and intensity information encoded in vision nor on comparisons of the combinatorial or intensity information encoded in olfaction, but rather state that in regards to our "naively" constructed olfactory space, we now have a quite large space to fill, even "just" in humans.

Attempts to define the range of that perceptual space have ranged from essentially two to one trillion. The dual axis theory[54] has received thoughtful criticism [30], but at the other end of spectrum (still awaiting thoughtful criticism) is the estimate of one trillion [16]. In order to avoid such extreme conclusions, I shall attempt to keep my independent variables cleanly separate from my dependent variables and to temper my enthusiasm (respectively, to each of the two preceding examples).

A neurobiological approach to deciding how to both measure and interpret olfaction could be based on the multi-level conceptual organization laid out by Churchland and Sejnowski [20]. As motivation, they outline a remarkably case study of development of our understanding of the visual system. Two competing theories described both red/green/blue light receptors [112, 113, 114, 115] as well as a conflicting description of the receptors based on psychophysical detection of blue-yellow and red-green opponency along with seemingly independent intensity scaling through putative black-white receptors ([42]). These two conflicting paradigms of visual processing are reconciled over the proceeding centuries as experimental evidence was gathered across multiple levels of organization.

Our current understanding incorporates receptor level evidence, local circuit considerations, and region-specific functions in cortex. This evolution in understanding the visual system un-

derscores importance of considering the neurobiology at multiple levels, from the receptors, to local circuits and maps, through systems, and even across the central nervous system as a whole. With those insights from Churchland and Sejnowski in mind, I proceed with outlining my specific consideration of olfaction at the level of receptors, neurons, local circuits, and maps.

The Accessory Olfactory System

The full gamut of chemosensory systems in mammals have the ability to detect chemicals in the environment, within the alimentary canal, and even within the parenchyma of various tissues (a small set of primary examples [11, 23, 64, 34]). I have focused on a single chemosensory modality, olfaction, and in a single model olfactory system, the aforementioned mouse accessory olfactory system (AOS).

Chemosensation in AOS begins at the periphery in the vomeronasal sensory neurons (VSNs) and proceeds to the accessory olfactory bulb (AOB). These VSNs express one of a number of receptor types (similar the main olfactory system, as described briefly above), and the afferent fibers of neurons expressing the same receptor type converge into regions of neuropil called glomeruli. The term glomerulus is used across many olfactory systems from fruit flies to mammals, referring to the structures resulting from this process of a converging population of sensory neurons expressing one receptor type. The glomeruli of the AOS are contained in the AOB which is found on the posterior face of the olfactory bulb, separated from raustral telencephalic neocortex by just arachnoid mater. It is from the AOB, that excitatory neurons (mitral cells) send axons to downstream targets in the amygdala and bed nucleus of the stria terminalis both of which subsequently project directly (and indirectly) to the hypothalamus [77, 33, 68]. [2]

The first stages of organization and processing of chemosensory information both occur within the AOB. Within the AOB are several general layers: the vomeronasal nerve layer, the glomerular layer, and two deeper external and internal cellular layers. In the glomerular layer, glomeruli are formed from incoming converging glutamatergic VSN axon terminals, processes from local in-

[2] The general pattern of having amygdalar and hypothalamic connections, although different in the exact details, is common feature of both of these mammalian olfactory subsystems [24].

terneurons, and the dendrites from mitral cells (for an exquisitely detailed anatomical reference see [55]). These glomeruli contain at least two signals: the presynaptic VSN sensory representation at the axon terminal and the postsynaptic representations in mitral cells or interneurons. Within the glomerular layer each receptor type forms multiple glomeruli, and while the approximate regional localizations and size variability have been described for a handful of the approximately 300 receptor loci, those studies were fundamentally limited in scope [105, 9]. At this stage of glomerular inputs and outputs there is a rich potential substrate for investigating chemosensory processing: converging signals from many VSNs expressing the same receptor, multiple glomeruli representing the same signals, as well as the postsynaptic transformation of those signal representations.

There are three major features of the AOS that make it an attractive subject for studying olfactory neural processing: the ability to record from the entire structure while preserving peripheral sensory neuron connections, the distance isolating the sensory neurons from their axon terminals and circuit components within the AOB, and finally the physiological salience of many of the known stimuli.

The first feature is that we can record from almost the entire circuit at one time. The peripheral sensory neurons of the AOS project to a relatively discrete region at the posterior face of the olfactory bulb. In contrast to the main olfactory bulb which has glomeruli on virtually all sides of the bulb, the AOB glomeruli are amenable to recording as a population. The ability to record from all glomeruli greatly enhances the ability to interpret stimulus responses.

The anatomical separation of the sensory neurons within the bony VNO capsule from the AOB provides an advantage to compare raw sensory axon terminal signals with the circuit modified inputs. The VNO which can be superfused and stimulated separately from the superfusion of the olfactory bulb, allows the delivery of pharmacological agents that can block circuit mediated feedback either selectively or very broadly block all post-synaptic glutamate driven activity, whether that glutamate drives excitatory or inhibitory targets.

The third attractive feature is that a number of the ligands are sulfated steroids, [3] which are

[3]Technically in the context of the types of sulfate moieties to which we are usually referring, the presumptive biological steroid metabolites are correctly referred to as sulfonates in respect to the metabolic product of

either metabolites or derivatives of the known structural families of steroid hormones that regulate physiology [70, 61, 3]. These span a range of structures that include examples of the broad classes of glucocorticoids, estrogens, progesterone metabolites, and androgens. The suggests that there may be a finite list of enumerable features that are detected by the system, further increasing our ability understand how that information is processed.

The combination of recording from the entire circuit, knowing both the inputs and circuit modified responses, and having a potentially enumerable set of physiological features represented among ligands may facilitate both interpreting our observations and testing further hypotheses.

Neural Processing in the AOB

Within the AOB, there are several testable hypotheses regarding neural organization and circuit processing.

My first hypothesis is regarding whether there is a pattern organizing locations of glomeruli within the AOB. We set out to functionally define glomeruli by building up maps of stimulus responses to a battery of stimuli. We segment those maps into glomerular regions based on those patterns of responses, and then used those regions to test the spatial relationships within those maps. Organization between regions could have implication for local processing within the glomerular layer, either postsynaptically or presynaptically. The occurrence of such patterns could serve basic functions such as decreasing the stochastic noise in the signal, which would be particularly useful given that VSNs fire in a bursting pattern even at "rest" [44, 3] or organizing inputs onto the dendrites of the mitral cell projection neurons.

My second hypothesis was that interactions could occur between the glomeruli representing components of mixtures. By comparing responses to both individual chemical stimuli as well as mixtures of those stimuli, we tested whether there was a difference between representation of the individual components of the mixture and the mixture. It is possible that mixture responses would

the substrate (whether steroid, catecholamines, tocopherols, or any other biomolecule) and an activated sulfate (3'-phosphoadenosine 5'-phosphosulfate or PAPS for short) [88, 31]. The regulation of both sulfatases and sulfotransferases is an essential to many steroid related aspects of homeostasis and development, from cancer to placental maintenance [32, 26, 37].

be the sum of the responses to components of the mixture, or alternatively activity in some regions representing the mixture components might affect activity in other regions during co-presentation of the components as a mixture indicating some circuit level processing.

A necessary third hypothesis was that interactions could occur between components of mixtures, that is that the interaction of each component of a mixture with a given receptor/glomerulus type might be different. If such an interaction between stimuli occurred, it would be independent of circuit feedback as it's origins would be in the VNO at the VSN chemosensory receptors.

In the main olfactory bulb MOB), there is ample evidence for multiple inhibitory pathways within the glomerular layer alone [6, 2], and if presynaptic lateral inhibition was present in response to axon terminal glutamate release, the evidence suggests that axon terminal $GABA_B$ (and possibly to a lesser extent D_2 [29]) receptors activated glutamate driven periglomerular cells would be the likely mechanism [107][5]. One class of interneurons interconnects more than a dozen glomeruli at a time [52]. The complexity of the picture only increases when other neuronal populations such as the deeper mitral cells and granule cells are considered[47].

While it is well documented that presynaptic inhibition occurs in at the olfactory sensory neuron axon terminals within the glomeruli [5, 103], there has been significant controversy over whether there is lateral presynaptic inhibition in mammalian olfaction. Slice physiology and *in vivo* recordings utilizing found that there was a large effect of $GABA_B$ receptor mediated inhibition that required ionotropic glutamate signaling [104]. A second set of similar experiments, both *in vivo* and utilizing tangential glomerular slices to preserve lateral connections between glomeruli, came to a similar conclusion, observing glutamate dependent $GABA_B$ mediated intraglomerular inhibition but not interglomerular inhibition [60]. In direct contrast, a conflicting report described experiments in anesthetized mice that measured a large effect of presynaptic inhibition that was strongly correlated with the activity in the surround, independent of activity in the center. [102]. Finally, *in vivo* investigation into tonic presynaptic inhibition regulation of olfactory axon terminal neurotransmitter (glutamate) release, but the group again found no dependence on spatial organization, no lateral inhibition [76]. This work effectively neatly divided the field into a pair of

hypotheses, each put forward by different groups of researchers.

While complete imaging of the main olfactory bulb is not currently possible, we do currently have the ability to record from nearly the entire AOB circuit, and the previously enumerated features make the AOB an attractive target for expanding the study of both neural organization and computation. Such global circuit recordings make it possible to test both for the presence of lateral inhibition in the accessory olfactory system as well as the role of presynaptic inhibition across the circuit, as our observations of the the neuronal processes occurring can be made across all AOB glomeruli.

Experimental Approach

We planned to use a series of methods, outlined extensively in Chapter 2, in our approach but we will cover them briefly here. We utilize a genetically encoded calcium indicator, expressed in the VSNs and present in the axon terminals to detect stimulus driven changes in calcium fluorescence and record that fluorescence at the axon terminals in the AOB as a marker for stimulus evoked glutamate release [39]. We utilize a hemi-head preparation which preserves connections between sensory neurons and the AOB, as well as local circuit connections [62, 27]. To record activity in experimental preparations, we use OCPI scanning microscopy to acquire one frame (1003 x 1004 pixels) every 50 ms, and we deliver various stimuli (synthetic ligands as well various urine stimuli) dissolved in Ringer's saline through a small cannula placed into the vomeronasal organ, contained in a bony capsule at the base of the nasal cavity. Pharmacological agents can be then applied separately along with superfusion of the experimental preparation, such that we are able to record both the raw inputs signals to the circuit and the circuit modified inputs signals.

Summary

The AOB presents a compact and accessible model for chemosensory and neuronal processing, which provide an attractive model for understanding brain circuits and later brain/behavior relationships. In this dissertation I hope to answer some specific as well as general questions about

neuronal processing in this system.

With regard to the organization of glomeruli within the AOB, Chapter 3 describes a modular map resulting from specific patterns of reliable separation and adjacency between types of regions. This modular association could be measured by both a complex ethological stimulus set and a synthetic sulfated steroid stimulus set. In both sets, we observed both types of spatial relationships between types of glomeruli, with some being reliably closer to or farther away from other types of glomeruli. These multiple spatial relationships appear to be the basis of a modular map in which relative locations are a defining feature.

While organization suggests the an arrangement potentially useful for neural processing, it does not demonstrate function. More concrete evidence regarding whether these regions interact, that is if activity in one glomerulus or region influences activity in the other. In Chapter 4, I describe a series of experiments meant to probe whether olfactory representations exert lateral modulatory effects. Glomeruli with strong spatial relationships, both those occurring in modules defined by a set of stimuli and those occurring in relative isolation, were tested for the presence of interactions when responding to individual component chemical stimuli and to multiple component mixtures. The presence of these interactions along with the ability to abolish them using pharmacological agents strongly supports the idea that there are some regions of chemical space that are represented as interacting.

Together, the data presented in this dissertation argue not only for a specific organization to the accessory olfactory system but also for organization that supports specific types of neural processing between local regions.

Chapter 2

Methods

2.1 Illustration

Illustrations for Chapter 3 were performed in Adobe Illustrator and Photoshop. All illustrative image processing for Chapter 4 was performed in the freely available software packages Inkscape and GNU Image Manipulation Program. For anatomical reference points, we utilized MRI images available online from MRTE (http://www.mrtechnology.co.jp/date/2008/04/13/) and dissection images from published dissection methods articles [27, 62].

2.2 Experimental Preparations

Animals

For GCamP2 accessory olfactory bulb (AOB) experiments, driver mice with an OMP-IRES-tTA (C57Bl/6 background) transgene were mated with transgenic effector mice harboring a tetracycline transactivator response element and minimal promoter 5' of the coding region for the Ca2+ protein GCaMP2[39]. 14 adult (>60 days postnatal) male mice were used as experimental animals for the functional mapping (n=10) and concentration series (n=4) experiments described in Chapter 3. 18 adult (> 60 days postnatal) female mice were used as experimental animals for time/vehicle

pharmacology controls (n=3), ionotropic glutamate receptor blockade (n=4), $GABA_B$ receptor blockade (n=6), $GABA_A$ receptor blockade (n=5), and cross-gender validating steroid modules (n=2) experiments as described in Chapter 4. Only one AOB was imaged per animal as hemi-section requires intact sagittal structures be removed from the contralateral side.

For GCaMP3 vomeronasal sensory neuron (VSN) imaging experiments, driver mice with an OMP-Cre (C57Bl/6 background) were mated with transgenic effector mice harboring a GCaMP3 knock-in[92, 116]. Three adult (>60 days postnatal) female mice were used as experimental animals (single conditions stimulus delivery to an isolated preparation) with only one vomeronasal organ (VNO) neuroepithelium imaged per animal[109][93].

All mice were housed in single-sex cages of no more than 5 animals from weaning until experimental use with *ad libitum* access to food and water. Animals were housed on a standard 12 hour – 12 hour light/dark cycle. All BALB/c mice used for urine collection were purchased from The Jackson Laboratory. All animal procedures were approved by the Washington University Animal Studies Committee.

AOB Preparation

The AOB hemi-head dissection were performed as described previously[27, 62]. Briefly, mice were deeply anesthetized with isofluorane anesthesia, and quickly reduced via gross dissection in ice-cold, oxygenated (5% CO_2/95%O_2) artificial cerebrospinal fluid (aCSF): phosphate/bicarbonate buffers (from sodium bicarbonate as $CHNaO_3$ 25 mM and sodium phosphate monobasic as H_2NaO_4P 1.25 mM); additional essential ions (sodium chloride as $ClNa$ 125mM; potassium chloride as ClK 2.5 mM; and calcium chloride as $CaCl_2$ 2 mM; and magnesium chloride as $Cl_2H_{12}MgO_6$ 1 mM); and metabolic substrates (glucose as $C_6H_{12}O_6$ 25 mM; sodium pyruvate $C_3H_3NaO_3$ 2 mM; myo-inositol $C_6H_{12}O_6$ 3 mM; and sodium ascorbate $C_6H_8NaO_6$ 0.4 mM). During the gross dissection, an addition 7 mM magnesium chloride is present to limit excitotoxicity. The reduced prep allows the peripheral vomeronasal organ (VNO), afferent nerves, and the central AOB circuit to be rapidly cooled for subsequent micro dissection.

The subsequent micro dissection is performed to minimize imaging artifacts by clearing the surface of the bulb from arachnoid mater and vessels, and to place a small 0.005 inch inner diameter cannula inside the vomeronasal organ (VNO). We maximize superfusion efficiency by removing midline cartilage, bone, and dura mater.

After the initial gross hemi-head dissection, the prep was adhesed, using a cyanoacrylate glue (such as Vetbond, 3M, St. Paul, MN, USA), to a small delrin plastic plank. This mounted prep was then adhered with silicon vacuum grease (Dow Corning, Midland, MI) to the base of a dissection chamber. Micro dissection follows immediately, and the preparation was superfused rapidly (25 mL/min) with room temperature (22–25° C) oxygenated aCSF. The vomeronasal nerves were exposed via micro dissection and remove the septal cartilage and septal bone. The dura (anterior most portion of *falx cerebri*) separating the olfactory bulbs was removed. Arachnoid mater and vasculature at the imaging surface of the AOB were removed.

After micro dissection, within the dissection chamber the final reduced hemi-head prep thus included the ipsilateral bony nasal structures, ipsilateral septal mucosa with afferent vomeronasal nerves sans septal cartilage and bone, and the ipsilateral olfactory bulb. This preparation was moved to a customized tissue imaging chamber, and the 0.005" inner diameter polyimide cannula was carefully placed inside the vomeronasal organ (VNO) lumen while VNO Ringer's saline is flowing. We delivered a steady stream (0.2 mL/min) of a Ringer's saline (pre-bubbled with 5% CO_2/95%O_2 at 40 ºC and cooled to 35 ºC, from which aliquots were taken, into which all stimuli and controls were diluted. Stimulus order is randomized for injection into the VNO. We estimate the volume within the VNO lumen (approximately 2 µL in volume) was replaced approximately every 0.5–1 s by fresh VNO Ringer's saline: bicarbonate/HEPES buffer system (from sodium bicarbonate as$CHNaO_3$25 mM and HEPES as $C_8H_{18}N_2O_4S$ 10 mM); additional essential ions (sodium chloride as $ClNa$ 115 mM; potassium chloride as ClK 5 mM; calcium chloride as $CaCl_2$ 2 mM; and magnesium chloride as$Cl_2H_{12}MgO_6$ 2 mM); and metabolic substrate (glucose as $C_6H_{12}O_6$ 10 mM).

VNO Dissection

VNO dissection and whole mount preparations were performed as previously described [109]. In brief, mice were deeply anesthetized with isofluorane and immediately decapitated. The bony VNO capsules containing the neuroepithelium were removed and placed into ice-cold, oxygenated VNO Ringer's. The VNO bony capsule was perforated with a forceps and separated from the soft tissue but left intact. The transition from the lateral vascular epithelium is grossly distinguishable from the medial neural epithelium, and an incision is made along the transition zone and then the tissue is bisected and lateral vascular epithelium discarded. The neuroepithelium, in just a drop of solution, is then carefully transferred to a clean Sylguard coated dish, basal layer facing up. A nitrocellulose membrane is placed onto the neuroepithelium, so that the basal layer adheses to the nitrocellulose. The now mounted tissue is transferred to a custom imaging chamber, clamping the mounting membrane between the base and top half of the chamber. A continuous stream of VNO Ringer's solution (0.5 mL/min) is delivered directly onto the tissue via a temperature controlled probe at 35 ºC (pre-bubbled with 5% CO_2/95%O_2 at 40 ºC and cooled to 35 ºC), from which aliquots were taken, into which all stimuli and controls were diluted. Stimulus order is randomized for injection into the VNO. VNO Ringer's saline matches that described for the AOB.

Pharmacology:

On the day of each experiment, drugs and/or vehicle were diluted from frozen stocks (stored at -20 ºC) to their final concentrations in aCSF. Although each experiment had an internal control or baseline, we also tested some animals in a series of time/vehicle control experiments in which vehicle was administered during the second "condition" (0.015% DMSO). The vehicle solvent concentration during "blockade" was 0.0001 during ionotropic glutamate blockade, 0.015% for 0.00015 parts or 0.015% for controls and for $GABA_B$ blockade, and 0.03% for $GABA_A$ blockade. Ionotropic glutamate blockade of post-synaptic targets was achieved by using D-AP5 (D-(-)-2-Amino-5-phosphonopentanoic acid as $C_5H_{12}NO_5P$ 50 µM) in com-

bination with NBQX (2,3-Dioxo-6-nitro-1,2,3,4-tetrahydrobenzo[f]quinoxaline-7-sulfonamide as $C_{12}H_8N_4O_6S$ 10 μM) diluted into aCSF from 100 mM aqueous and DMSO stocks, respectively. Metabotropic blockade of $GABA_B$ receptors was achieved using a single compound, CGP 55845 ((2S)-3-[[(1S)-1-(3,4-Dichlorophenyl)ethyl]amino-2-hydroxypropyl](phenylmethyl)phosphinic acid hydrochloride as $C_{18}H_{22}Cl_2NO_3P.HCl$ 15 μM) diluted into aCSF from 100 mM DMSO stocks. Ionotropic blockade of $GABA_A$ receptors was achieved using SR 95531 (gabazine or 6-Imino-3-(4-methoxyphenyl)-1(6H)-pyridazinebutanoic acid hydrobromide as $C_{15}H_{17}N_3O_3.HBr$ 30 μM) diluted into aCSF from 100 mM DMSO stocks. All drugs were purchased from Tocris Bioscience and stored at -20 ºC as dry powders until stocks were made, at which time they were aliquoted into single use vials to be used within in the proceeding two months.

Stimuli

On the day of each experiment, VNO stimuli were dissolved to their final concentrations (0.1 μM – 10 μM) in Ringer's solution. Sulfated steroids were purchased from Steraloids, Inc. (Newport, RI, USA), and stock solutions (100 mM, stored at -20 ºC) were produced by dissolving steroids into methanol, both to maintain solubility and to limit hydrolysis demonstrable during storage (chromatographic analysis by ourselves). This process is theoretically limited by methanol storage[98]. Although neither AOB imaging nor VNO recordings have demonstrated sensitivity of vomeronasal sensory neurons to the methanol vehicle at 2,000–10,000-fold dilutions, control Ringer's stimuli (to which other responses were compared) always contained the maximum methanol concentration applied across all stimuli. The sulfated steroids applied are listed in Table 2.2.

BALB/c urine was collected as described previously[70]. All animals were co-housed in groups of five age, gender, and gonadal status animals and all collections were performed with multiple cages of each type, each group having ten contributing sources. For adult male and female urine (intact or gonadectomized), single-sex cages of intact adult (>P60) BALB/c male or female mice were suspended in wire mesh bottom cages above liquid nitrogen. For juvenile males and females, P21-23 male or female mice were suspended in a wire mesh bottom cage. Frozen urine from

several cages was pooled across several days' collections (limited to 60 hours for P21 mice), then centrifuged and filtered to remove particulates, aliquoted, and stored at -80 °C. Pooling intact adult female mouse urine likely incorporated substances found in female urine at various stages of the estrous cycle, and averaged them over time.

Sulfated Steroid Stimulus Table

Stimulus Referent	Steraloids Catalog #	Full chemical name	Common name
List A1	A6940-000	4-androsten-17α-ol-3-one 17-sulfate	epitestosterone sulfate
A2	A7010-000	4-androsten-17β-ol-3-one 17-sulfate	testosterone sulfate
A3	A7864-000	5-androsten-3β, 17β-diol 3,17-disulfate	3β-androstanediol disulfate
E1	E0893-000	1, 3, 5(10)-estratrien-3, 17α-diol 3-sulfate	17α-estradiol sulfate
E2	E1050-000	1, 3, 5(10)-estratrien-3, 17β-diol 3,17-disulfate	17β-estradiol disulfate
E3	E4105-000	4-estren-17β-ol-3-one 3-sulfate	nandrolone sulfate
P1	P3817-000	5α-pregnan-3α-ol-20-one 3-sulfate	allopregnanolone sulfate
P3	P3865-000	5α-pregnan-3β-ol-20-one 3-sulfate	epiallopregnanolone sulfate
P2	P8200-000	5β-pregnan-3β-ol-20-one 3-sulfate	epipregnanolone sulfate
Q1	Q1570-000	4-pregnen-11β, 21-diol-3, 20-dione 21-sulfate	corticosterone 21-sulfate
Q2	Q3910-000	4-pregnen-11β, 17, 21-triol-3, 20-dione 21-sulfate	hydrocortisone 21-sulfate

2.3 Urine Biochemistry

We followed protocols for sulfatase treatment of female urine previously reported [70] with changes in duration to minimize sample degradation. Analysis by thin layer chromatography (7:3:1 chlo-

roform:methanol:water) and mass spectroscopy confirmed near total cleavage of sulfate groups in a modestly position dependent manner, with 3- and 17-alkyl positions poorly cleaved in single compound test reactions. Yet no sulfated steroids of similar size were detectable in mass spec analysis of urine samples (data not shown) and was indescriminable from the reported 24 incubation protocol. Thus all samples were treated at validated enzyme activity levels for 2 hours to limit off target reactions and degradation.

BALB/c female urine was diluted 1:1 in 0.25 M sodium acetate buffer (pH adjusted at 37 °C) and 1000 Units per mL urine H1 sulfatase extracted from *H. pometia* (Sigma Aldrich) was added to the first dilatation. Both sulfatase and control reactions were incubated for 2 hours at 37 °C. In order to prepare the treated samples for physiology and mass spectroscopy, we ran both reactions over a Phenomenex Strat-X polymeric reverse phase chromatography column. Columns were washed with 1 volume methanol and 1 volume H_2O before the buffered reactions were applied.

After applying reactions to the column, the resin was washed with one volume water/methanol/acetic acid mixture at a 78:20:2 ratio. One column volume of methanol was then used to extract soluble compounds from the resin and these were dried under nitrogen gas. Samples were subsequently dissolved in 1:2000 methanol to their original urine volume in order to match the methanol volume in sulfated steroid stimuli.

Mass spectrometry was utilized to measure the loss of sulfate precursor ions in the sulfatase treated sample compared to the control sample [70]. We observed that compounds in the range of m/z 300 to 350 were lost in the sulfatase treated but not control treated urine.

2.4 Imaging Procedures

AOB GCaMP2 Ca2+ imaging

Volumetric images of the mouse AOB were reconstructed from a smooth scanning acquisition with serial readout of optical sections of the reduced hemi-head preparation using an objective-coupled planar illumination (OCPI) microscope[43]. The imaging was performed in a custom

imaging and superfusion chamber, such that the cannulated VNO was superfused separately from the AOB, allowing stimuli to be applied within the VNO. The microscope consists of a 20x water immersion objective with (Olympus, Center Valley, PA, USA) mounted on a piezoelectric actuator with a 400 μm range (Piezosystem Jena, Hopedale, MA, USA), onto which is mounted a custom-designed coupler linked to an optical fiber, a light collimator, and a light sheet-forming cylindrical lens oriented at 90° to the focal plane of the microscope objective. Images were taken using a 1004x1002 pixel EM-CCD camera (Andor, South Windsor, CT, USA) located after a 100 mm tube lens (Infinity Photo-Optical Company, Boulder, CO, USA). Volumetric images were produced by scanning the light sheet across the tissue. The total potential scan range along the "z" axis was 400 μm, but the "z" step size was typically limited to 6 μm with a dwell time of 50 ms/frame and scan time of 2.55 s/volume (in three AOB preps, the scan time was up to 0.4 s longer due to imaging angle). Voxel dimensions were thus 0.71 μm x 0.71 μm x 8 μm (6 μm for experiments in Chapter 4). Although, in all cases our custom software for registration and analysis uses the actual acquisition parameters, we later restricted the inter frame distance to more closely reflect the estimated light sheet thickness after we conducting a optics realignment procedure, and thus the total dimensions of typical image stacks were 713 μm x 712 μm x 400 μm (or 300 μm in the latter case). The total time to acquire and write each image stack was ~5s.

Prior to image acquisition, the superfusing aCSF was warmed to 33–35° C and the preparation and chamber were allowed to equilibrate for 15 minutes. A second oxygenated bubbling of aCSF occurs in a screened bubbling chamber built into into the imaging chamber but just before actual tissue superfusion. Depending on the experimental paradigm, 11 sulfated steroids (1–10 μM) or there mixtures, 100-fold diluted BALB/c urine samples, and control Ringer's stimuli were delivered to the VNO through the polyimide cannula using a pressurized, computer-controlled stimulus delivery system (AutoMate Scientific, Berkeley, CA, USA) or an UltiMate 3000 analytical autosampler (Dionex, Sunnyvale, CA). Each stimulus lasted 3 or 5 image stacks (15 s for experiments performed in Chapter 4 or 25 s for experiments performed in Chapter 3) and was followed by a recovery period of at least 12 image stacks (60 s). All stimuli were presented in 4

or 5 randomized, interleaved blocks. This means that for an exceptionally small 979 μm^3 region of interest (ROI) of composed of a minimum of 324 voxels, we had a minimum of 19440 voxel data points per mean stimulus timecourse.

$$18^2 \frac{voxels}{stack} * 15 \frac{stacks}{presentation} * 4 \frac{presentations}{stimulus} = 19440 \frac{voxels}{stimulus}$$

In a small subset of experiments, we acquired images from single frames at 10 Hz, stimulating the VNO for with P8200 or Q1570 for 10 s with a recovery period of 50 s.

VNO GCaMP3 Ca2+ imaging

Volumetric images of the mouse VNO were reconstructed in a similar fashion from a smooth scanning acquisition with serial readout of optical sections of the VNO neuroepithelium using an objective-coupled planar illumination (OCPI) microscope[43]. Images were acquired in a custom imaging and superfusion chamber with tissue mounted on a nitrocellulose membrane, similar to those used in protein blotting procedures. The microscope, camera, and acquisition systems were the same as listed for the AOB. Volumetric images were produced by scanning the light sheet across the tissue. The scan range along the "z" axis was 400 μm, but the "z" step size was typically limited to 5 μm with a dwell time of 50 ms/frame and scan time of 2.55 s/volume. Voxel dimensions were thus 0.71 μm x 0.71 μm x 5 μm (although, in all cases our custom software for registration and analysis uses the actual acquisition parameters), and thus the total dimensions of typical image stacks were 713 μm x 712 μm x 250 μm. The total time to acquire and write each image stack to disk was ~5s. Prior to image acquisition, the superfusing VNO Ringer's was warmed to 42.5 °C and allowed to cool but always delivered at a temperature controlled 36 °C . Depending on the experimental paradigm, sulfated steroids (1–10 μM) or mixture of those stimuli, 100-fold diluted BALB/c female urine, and control Ringer's stimuli were delivered to the VNO epithelium through a MEA Systems temperature controlled perfusion probe by a computer-controlled stimulus delivery system (AutoMate Scientific, Berkeley, CA, USA) or an UltiMate 3000 analytical autosampler (Dionex, Sunnyvale, CA). Each stimulus lasted 3 image stacks (15 s) and

was followed by a recovery period of at least 12 image stacks (60 s). All stimuli were presented in 4–5 randomized, interleaved blocks. This means that for a exceptionally small 161.3 μm^3 region of interest (ROI) of composed of a minimum of 64 voxels, we had a minimum 3840 voxel data points per mean stimulus timecourse.

$$10^2 \frac{voxels}{stack} * 15 \frac{stacks}{presentation} * 4 \frac{presentations}{stimulus} = 3840 \frac{voxels}{stimulus}$$

2.5 Noise Detection, Exclusion, and Regression

Initial Data Exclusion

Approximately 2/3 of data sets were discarded during quality control due to visible noise sources such as unremovable free microvasculature (order 10-100 μM) or unstable response magnitudes which monotonically decrease by more than 10% over the course of the experimental baseline acquisition.

Noise Detection and Removal

We utilized a series of steps to assess movement and recording artifacts and to annotate them via not a number (NaN) designation for particularly obvious noise sources before registration and data processing.

We assume that the noise sources in fluorescence ought not exceed shot noise, that is the stochastic Poisson distributed noise present in the processes of signal acquisition. We had a sufficiently large number of counts then that by using a unbiased estimate of intensity across an acquired frame, such as the median intensity, we tested each frame for deviation from the expected median intensity relative to another frame. In particular, we statistically compared each frame to it's temporally adjacent neighbors (unless they had been flagged with NaN, in which case the comparison extended one step further in time).

In order to detect smaller deviations in data after registration to the base stack, we calculated

the voxel-wise mean square intensity mismatch between the stack image and the base stack image. In this way we measure the mean square mismatch for each image frame (z) in stack image volume I_i .

$$E(z)_i = \sum_{x,y} (I(x,y,z)_i - I(x,y,z)_{base})^2$$

We then used median filtering (MatLab, medfilt1improved) over five time points and flagged any frames with errors in significant excess of the expected error.

$$E(z)_I = 10 * median(E_{expected}(Err(z)_i)$$

In determining whether a particular chunk of data is an outlier, we directly compared temporally adjacent chunks of data. The rational for this is that we sample at a frequency greater than that of the largest magnitude fluorescence changes in data, we should be able avoid selecting responsive regions but rather select regions of excessive movement.

Post-registration Data Exclusion Criterion

The images were also assessed for other less obvious sporadic noise sources. This require image registration to minimize small movements between stacks and pulled out much less obvious errors.

In order to achieve an estimate of the by voxel signal intensity we averaged the frames from one time point forward and backward. If more than 1 in 252 (0.04%) of voxels in given frame varied (were greater or less than) by more than one half the mean intensity for that voxel, the frame was automatically flagged. Qualitatively, these events indicated sudden slight decreases in image clarity, unregisterable movement after registration, power fluctuations whether laser or camera, or small light scattering events (bubbles). Frames errors were no more likely to be detected during stimulus delivery than during the interstimulus interval (ANOVA, p=0.47) and thus deemed to be related to acquisition and not stimulus. In our glutamate blockade data, we observed a mean of 1.24% of stacks containing bad frames (mean of 7.57 bad frames with a standard deviation

of 4.32 frames and a range of 1 to 51 frames) which resulted in discarding 0.18% of our data after stringent inclusion criterion. Our analysis infrastructure has been designed to annotate and accommodate empty ("not a number") regions of data that are discarded due to having acquisition errors, imaging artifacts, or other detectable noise. VNO data were not modeled with GLMs.

Post-exclusion Noise Regression

To detect more covert and potential various noise sources, we utilized a conservative number of parameters, from 2 to 9 parameters for ~$4e^{10}$ data points per experiment recording, to estimate covert correlated noise components across all voxels in the data set (publicly available code, GLMdenoise, [Kay2013]). This resulted in a small number of components that explained a significant amount of multiframe signal variability, that were not excluded by the mismatch error detection described above or

2.6 Image Analysis

Region Definition by Change in Calcium Fluorescence

For further details see Appendix.

For both VNO and AOB imaging, volumetric time series movies (each ~100 GB in raw data) were analyzed in MATLAB (Mathworks, Natick, MA, USA) using custom software described previously [95, 36]. Each image stack was "registered" to a reference stack acquired between stimulus presentations near the middle of the experiment. For the AOB, an important aspect of the image registration is qualitatively handling both higher frequency movements occurring between individual stacks in addition to slow changes such as tissue swelling; quantitatively, image registration typically reduced the mean squared difference between the voxels in any given stack by ~100 fold although the magnitude varied both over time and pharmacological conditions. In the VNO, high frequency movement was not a concern but registration was still required to maintain cell alignment over the duration of the experiments. The number of stacks used to

estimate stimulus response fluorescence were fixed for an experiment, but could vary due to noise exclusion criterion as described. Data exclusion due to frame errors was not significantly biased toward any particular segment as detailed in that section of the methods (p=0.47).

To measure resting or baseline fluorescence, we averaged the fluorescence intensity at each image voxel in 2-3 consecutive stacks prior to stimulus onset ($f_{resting}$). To measure stimulated activity, we averaged the fluorescence during the 2-3 stacks of stimulus presentation to the vomeronasal organ ($f_{stimulus}$). From these, we computed the relative change in fluorescence intensity for each voxel (coarsened, via array restriction methods to 252x252 in the higher resolution dimensions) for each stimulus trial.

$$dF/F = \frac{\Delta F}{F} = \frac{f_{stimulus} - f_{resting}}{f_{resting}}$$

Outside of the Methods, $\frac{\Delta F}{F}$ is referred to as dF/F.

To measure the reliability of responses across repeated stimulus presentations, we also computed the "response reliability index" (RRI) for each voxel.

$$RRI = \frac{mean\left(\frac{\Delta F}{F}\right)}{stdev\left(\frac{\Delta F}{F}\right)}$$

Where $stdev$ represents standard deviation of the mean across all stimulus repetitions. This produced a 4-dimensional (X x Y x Z x stimuli) voxel by stimulus matrix for each the change in fluorescence and RRI. We thresholded 4–D voxel by activity matrices, then subjected 4–D image to dot product or magnitude correlation image flow, wherein each voxel was associated with itself or an adjacent voxel. Thus each voxel was assigned to itself or the 26 voxels sharing edges with this voxel. This association was determined by calculating the maximum multidimensional peak in $\frac{\Delta F}{F}$ (the magnitude correlation or dot product) by traversing an "uphill" path of its nearest neighbor voxels, unless the voxel in question was the local maxima. This process produced volumetric ROIs. This process is further expanded on in the Appendix; all procedures contained within the appendix were limited to experiments performed for Chapter 3.

While some adjacent ROIs shared identical response patterns and no obvious physical discontinuities or differences (i.e. a "split" ROI), they occasionally had different time course responses. If however, they appeared to be homogenous in all those aspects no aspect of physical shape belied potential anatomical separation, then we manually merged such ROIs using a customized graphical user interface in MATLAB.

2.7 ROI Analysis

Inclusion Criterion

For each volumetric ROI in Chapter 3, a scalar response value was produced by weighting the activity of each voxel by its dot product with the mean response, then summing all activity within the ROI. Thus, the Ca2+ activity for experiment was condensed to a (nStacks x nROIs) matrix. Only ROIs which responded with ΔF/F exceeding the various thresholds and which showed statistically significant responses compared to Ringer's controls for at least one stimulus ($p < 0.05$, Wilcoxon rank sum test) were included in subsequent analyses.

For each volumetric ROI in Chapter 4, regions were included if the joint probability of significance compared to Ringer's control was significant ($p < 0.05^2$) where p was defined as the p-value was defined as the multiple of p-values for that ROI and stimulus across both pharmacological conditions.

Concentration Response Analysis

For the concentration-response analysis in Figure 3.5.2, we calculated the GCaMP2 "signal strength", the sum of the $\frac{\Delta F}{F}$ signal for all voxels that crossed experiment-specific RRI thresholds. We then normalized these values for each experiment by the maximum value across stimuli and concentrations. Because the maximum value was not always elicited by 100 μM P8200, the average across experiments, even for 100 μM P8200, was less than 100%.

Clustering of Glomerular Response Patterns

From each set of experiments an nStimuli x nROIs matrix of $\frac{\Delta F}{F}$ values was computed as described above. We utilized clustering algorithms (based on mean shift clustering[22]) to identify common patterns of activity in the population (Figures 3.3.3f and 3.3.6b). We evaluated sulfated steroids cluster results at multiple ROI thresholds (Supplementary Figure 3.5.5). The resulting patterns strongly agreed with patterns identifying functional classes of VSNs from somatic recordings . For steroid clusters (VSN classes), labels were arranged to match a common numeric assignment (Classes 1-10 plus an unclustered group; Figure 3.3.6b).

For the subsequent analyses (Chapter 4) the best fit to a linear projection of those clusters (3, 4, 5, and 8 defined by the pregnanolones and estradiol sulfates) in the relevant dimensions was used to categorize ROIs into the previously defined groups but with numeric assignments (1, 2, 3, and 4, respectively for the aAOB with the rest assigned separately into pAOB groups, see following section of positional analysis); Figure 4.3.3.

Analysis of ROI positions

Several methods were used to compare the positions of ROIs. To measure absolute glomerulus positions (Figure 3.3.4 and Supplementary Figure 3.5.6), we first identified ROIs on the basis of their responses to one or more stimuli. For each experiment, we generated a set of 3 orthogonal vectors indicating the anterior/posterior, medial/lateral, and depth axes using a biplanar fit to the surface of the tissue and the visible division between the aAOB and pAOB (the *linea alba* [55]). We then measured ROI positions along each of these axes by computing the dot product between the ROI position and the orthogonal vectors. We then normalized the ROI positions along each axis. We simplified each ROI as a sphere (matching the centroid and volume of observed ROIs), and then measured the tendency for ROIs of each class to occupy positions along each axis. We did this by normalizing to the total occupancy across all classes, and then comparing these relative occupancies to those expected from 100,000 shuffled glomerular maps. In the shuffle test, ROI positions remained static but cluster identities were scrambled. Shuffle

tests were used to indicate the 95th percentile, corresponding to a 95% confidence interval for relative occupancy. Glomerular classes showing preferential occupancy along any axis show relative occupancy exceeding this 95thpercentile.

For measurements of relative spacing between glomeruli, (Figures 3.3.4e and 3.3.8b), pairwise distances were computed where $d_{ROI(i,j)}$ is the Euclidean distance between ROI centroids and $V_{g(i,j)}$is the geometric mean of the ROI volumes.

$$d_{ROI(i,j)} = d_{c(i,j)} - \sqrt[3]{\frac{3}{4\pi}V_{g(i,j)}}$$

In this case, we used a shuffle test (N=10,000) to establish the propensity for randomly-chosen elements in the set to produce a given measured distance. The median minimum pairwise distance from each ROI in Cluster/Class 1 was calculated for members of all other Clusters/Classes 2-10 (first column of Figures 3.3.4e and 3.3.8b). This value was then compared to mean values taken from 10,000 sample sets with the same number of ROIs per class, but with class identities shuffled. We calculated the likelihood of encountering each value by computing a physical spacing index (PSI).

$$PSI = \frac{median_{observed} - mean(median_{shuffled})}{stdev(median_{shuffled})}$$

The PSI thus resembles the statistical z-score. PSI values less than 0 indicate values closer together than expected in shuffled sets, and vice-versa.

Chemical Space and Receptive Field Analysis

For each sulfated steroid, the chemical structure was entered into online DRAGON software [91, 35], which produced a set of 1,666 of molecular descriptors. Of these descriptors, 1,319 varied across the 11 stimuli. We normalized the values as follows.

$$n_{i,j} = \frac{x_{i,j} - min(x_j)}{max(x_j) - min(x_j)}$$

Where $x_{i,j}$represents the raw value of the i^{th} molecule for the j^{th} descriptor, and $n_{i,j}$ is the normalized value. Thus, the range of normalized values for each descriptor ranged from zero (the minimum observed value for a particular descriptor) to 1 (the maximum observed value for a particular descriptor). We then computed the chemical dissimilarity for each VSN class receptive field pair by calculating the mean Euclidean distances between all components of each class pair. For example, the dissimilarity between Class 1 (responsive to Q1570 and Q3910) and Class 4 (responsive to P3817, P3865, and P8200) was the average Euclidean distance between the 1319-dimensional representations of all steroid comparisons.

A pairwise dissimilarity matrix was made, and a 2–D visualization of this matrix calculated using nonclassical multidimensional scaling (MATLAB function "mdscale"; Figure 3.3.7a). This analysis summarizes the differences across all 1,319 chemical descriptors without weighting any particular descriptor as being more or less important for its binding properties. Because the features that relate structure to receptor binding are not clear, this remains one of the best objective ways to compare odorant structures to one another.

We calculated a relative chemical spacing index (Figure 3.3.8c) by comparing pairwise chemical dissimilarity values to 10,000 iterations of a shuffle test. In each instance of the shuffle test, the identity of the steroids giving rise to each receptive field was shuffled (e.g., for Class 4, each of the 3 steroids giving rise to the receptive field was randomly resampled, without replacement within the panel 11 steroids). This process produced values assessing the relative spacing of these receptive fields, with closeness indicated by values < 0 and farness by values > 0. Note that this comparison is specific to the molecules and activity patterns found with this stimulus set.

Isomap and Spring Embedding Analysis

We evaluated the tendency for glomerular juxtaposition and dispersal to be correlated (or anti-correlated) with receptive field similarity using a spring embedding model (Figure 3.3.8d). In this model, normalized estimates of receptive field similarity R_S were used as the spring constant $k_{rf} = R_S^3$. The relative physical spacing between glomeruli was measured using 2- dimensional

isomap analysis [90] ("Isomap.m" in MATLAB dimensionality reduction toolbox). To produce the 2D isomap, we identified the 6 nearest-neighbors for each ROI, and measured the probability for members of each other class to be among these neighbors. This produced a matrix of relative juxtapositions J between classes that was symmetrized and normalized (J_{norm}), and then evaluated by isomap analysis. The isomap epsilon term was set to the median value in J_{norm}. The spring embedding model was follows.

$$E = \sum_{i=1}^{n} \sum_{j=1}^{m} k_{rf(i,j)} \left(D_{i,j}\right)^2$$

Where E is the model energy, $k_{rf(i,j)}$is the receptive field difference between Classes i and j, and $D_{i,j}$is the pairwise Euclidean distance between the 2D isomap positions of Classes i and j. The observed values for E were compared to 100,000 shuffle test computations of $E(E_{sim})$ in which the $D_{i,j}$ terms remained constant while $k_{rf(i,j)}$ were scrambled. Values of E significantly lower than E_{sim} (i.e. less than the 5th percentile of the shuffle test) would indicate that similarly-tuned glomeruli are preferentially juxtaposed (i.e. chemotopy based on glomerular juxtaposition/dispersal), and E values higher than E_{sim}would indicate antichemotopy. The observed value of E in our dataset (Figure 3.3.7) was just slightly higher than E_{sim} (6.8 $\pm$ 0.8).

Suppression Index and Additivity

In order to measure the change in a component part of the mixture, we calculated normalized deviation from the expected response to the preferred stimulus, a "suppression index" (SI). This metric was only calculated for combinations of stimuli and mixtures that involved the preferred stimulus.

$$SI = \frac{\left(\frac{\Delta F}{F}\right)_{mixture} - \left(\frac{\Delta F}{F}\right)_{preferred}}{\left(\frac{\Delta F}{F}\right)_{preferred}}$$

To visualize this index across experiments and glomerulus/ROI types, we also constructed plots of the preferred stimulus response against mixture responses. This placed all SI values in

the same quadrant of the graph, such that each point represented 1 + SI and visualized any suppression as appearing below the diagonal of the quadrant (the line y=x).

$$\frac{\left(\frac{\Delta F}{F}\right)_{mixture}}{\left(\frac{\Delta F}{F}\right)_{preferred}} = SI + \frac{\left(\frac{\Delta F}{F}\right)_{preferred}}{\left(\frac{\Delta F}{F}\right)_{preferred}} = SI + 1$$

For the all pregnanolone responsive neurons which were responsive to multiple stimuli, we calculated the more general "additivity index" (AI) as the total deviation of the mixture response from the sum of component parts normalized over the sum of component parts. It is also notable that as additivity approaches zero, suppression is accounted for by a negative response to the non-preferred odor alone: the SI is a special case assumption of the AI where there is only one "preferred" stimulus.

$$AI = \frac{\left(\frac{\Delta F}{F}\right)_{mixture} - \sum \left(\frac{\Delta F}{F}\right)_{preferred}}{\sum \left(\frac{\Delta F}{F}\right)_{preferred}}$$

Delta (dF/F)

To visualize the magnitude changes across pharmacological conditions, we plot the $\frac{\Delta F}{F}$ response under glutamate blockade against the $\frac{\Delta F}{F}$ $\mathrm{response}$ in control conditions and also compare the slope values ($\Delta\frac{\Delta F}{F}$, referred to as delta (dF/F) outside of Methods). This is a visualization of magnitude effect of blocking circuit feedback.

Linear Modeling: ANOVAs and other GLMs

All linear model comparisons were performed using custom code in MatLab. The fits to the repeated measures ANOVA linear models and corrections for asphericity (mixed Greenhouse-Geisser and Huynh-Feldt adjustments to degrees of freedom) were performed in MATLAB using freely distributed code from Thomas E Gladwin[1]. It is worth noting corrections were only necessary for one instance which is specified in the text in which a test for asphericity was positive.

For the RM-ANOVAs we utilized a two factor design: ionotropic glutamate blockade (2 levels:

[1]http://www.mathworks.com/matlabcentral/fileexchange/30737

baseline and blockade) and stimulus (3 levels: pure compound, mixture one, and mixture 2). Given the small number of comparisons (n), we utilized strict Bonferroni or $\frac{1}{n}$ correction for multiple comparisons in *post hoc* t-tests.

In addition, within analysis comparison of effect sizes for adding variables, such as an interaction term to a linear model such as the RM-ANOVA were assessed by η^2. The η^2 can be calculated by multiple partial correlation (which in the case of a simple interaction is the equivalent of r^2, but requires a higher order partial correlation in the case of interactions between terms) by any appropriate method for generating a correlation or covariance matrix or by a linear regression of the third "interaction" term onto a dummy variable[56].

$$\eta^{2=} r^2_{Y(X_1,X_2,X_3)} = \frac{R^2_{Y(X_1,X_2,X_3)} - R^2_{Y(X,X_3)}}{1 - R^2_{Y(X,X_3)}}$$

As the model explicitly tested by the ANOVA is that if and only if there is a quantity relating the responses in one condition to those in the other ($c\tilde{r} = r$), then does that quantity (inhibition) explain the changes in each stimulus across conditions (in other words, does the stimulus by condition data deviate from the two parameters described).

Variance Scaling for Chi-square Based Population Parameter Fits

Subsequent further elaborations of the linear models were designed to test specific types of potential interactions. These were coded by the authors utilizing MatLab's singular value decomposition (svd) and least squares linear fit(lsqfit) algorithms, estimates of variance, and design matrices as described by the following. Standard deviation and variance were calculated in traditional manner for each stimulus response within each region. However, exclusively for the purposes of fitting and comparing entire data sets across subsequent models, it was is necessary to avoid overestimating the certainty in the variance and subsequently the χ^2goodness-of-fit certainty in fitting model parameters. For this purpose we estimated a single constant per experiment (one value per animal), a_x, such that in each data set, across all models we observed the minimum median reduced-$\chi^2 \geqq 1$. In practice, this was achieved by using multiple within-experiment estimates of the variance in stim-

ulus responses and glomerulus responses, such that for experiment x, the variance in glomerulus i to stimulus j in condition k was $\sigma^2_{i,j,k} = a_x * \left(\sigma^2_{i,j,k} + \frac{1}{o+n}\sum_k^o \sum_i^n \sigma^2_{i,j,k} + \frac{1}{o+m}\sum_k^o \sum_j^m \sigma^2_{i,j,k}\right)$.

Variance scaling was not used for the ANOVA or repeated measures ANOVAs (where traditional degrees of freedom corrections were used as described), but rather limited to subsequent comparisons of explanatory models in which the scaling could be constrained by a median parameter fit value for each animal. In particular, given the sphericity of the data when considering the relatively homogenous population types and only the preferred stimuli and mixtures of the preferred stimulus, such treatment was unnecessary except when comparing goodness of fit due relatively small ROI response variance in data sets.

ROI Inhibition by Condition

We analyzed change in inhibition across conditions in experiments with a baseline condition and two subsequent pharmacology conditions using acquired stimulus responses and scaled variances. While ANOVAs gave the same result with a much higher p-value, we wanted to be certain the uncertainty in the variance was appropriately considered as we describe in the previous section. Each ROI was fit for all stimuli in the stimulus set and the "self-connectivity" c value best minimizing the least-squares difference in stimulus responses after some blockade ($\widetilde{r}$) to those in baseline condition (r), as determined by singular value decomposition (svd).

$$\begin{aligned} \tilde{r} &= r + r * c \\ \tilde{r} &= r * (1 + c) \end{aligned}$$

Chapter 3

Functional organization of glomerular maps in the mouse accessory olfactory bulb

Previously published in Nature Neuroscience, 17(7), 953–61, 2014 with all author copyrights retained, although minor changes to text have been made within this version.

Authors: Gary F. Hammen[1], Diwakar Turaga[1], Timothy E. Holy[1,*], and Julian P. Meeks[2,*]

Affiliations: [1]Washington University School of Medicine, St. Louis, MO; [2]The University of Texas Southwestern Medical Center, Dallas, TX. *These authors contributed equally to this work.

Contributions follow: JPM and DT developed the imaging infrastructure; GFH and JPM conducted the experiments; and GFH, JPM, and TEH analyzed results and wrote the manuscript.

3.1 Abstract

The mammalian accessory olfactory system (AOS) extracts information about species, sex, and individual identity from social odors, but its functional organization remains unclear. We imaged presynaptic Ca2+ signals in vomeronasal inputs to the accessory olfactory bulb (AOB) during peripheral stimulation using light sheet microscopy. Urine- and steroid-responsive glomeruli densely innervated the anterior AOB. Glomerular activity maps for sexually mature female mouse urine overlapped maps for juvenile and/or gonadectomized urine of both sexes, whereas maps for sexually mature male urine were highly distinct. Further spatial analysis revealed a complicated organization involving selective juxtaposition and dispersal of functionally-grouped glomerular classes. Glomeruli that were similarly tuned to urines were often closely associated, whereas more disparately tuned glomeruli were selectively dispersed. Maps to a panel of sulfated steroid odorants identified tightly juxtaposed groups that were disparately tuned and dispersed groups that were similarly tuned. These results reveal a modular, non-chemotopic spatial organization in the AOB.

3.2 Introduction

Neural circuits decode the sensory world through a highly refined series of synaptic connections. Because most neuronal circuitry is local, progress in dissecting functional interactions has long emphasized the nervous system's spatial organization [59, 46, 66, 100, 18, 103]. Indeed, discovering how sensory modalities are "mapped" to regions of the brain was an essential step in deciphering their function. Discoveries in the visual and somatosensory cortices revealed links between sensory parameters and the location of neural responses, indicating that these sensory systems possessed "topographic maps" [59, 46]. Whether topographic or nontopographic, sensory maps have served as a foundation for our understanding of the brain.

However, many regions of the brain do not have a natural correspondence to external space; there is considerable interest in understanding the principles of spatial organization that govern such circuits. In the chemical senses, one prominent form of spatial organization is observed in the

olfactory bulb, in which olfactory sensory neurons expressing the same receptor gene project their axons into common regions of neuropil called "glomeruli" [100, 79]. This organization pools the output of many individual sensory neurons with identical specificity for odorants. This glomerular organization serves as a form of sensory map, since particular functional responses are reproducibly localized to particular regions8. In the main olfactory bulb (MOB) of rodents, numerous studies have defined the position and tuning profiles of many of the glomeruli [103, 82, 8, 97, 12, 50, 65, 86, 58, 89]. While this map is reproducible across animals, no overarching principle has been discovered that broadly describes its spatial organization [69]. The lack of a cohesive model for MOB topography might be a consequence of the huge diversity of odorous compounds and difficulties inherent in determining how "proximity in chemical space" is related to odorant receptor structure and axon targeting.

To overcome these barriers, one promising approach is to study maps and topography in an olfactory system selective for a narrower range of stimuli. An attractive candidate is the accessory olfactory system (AOS), also called the vomeronasal system, which specializes in the detection of social odors [83]. Vomeronasal sensory neurons (VSNs), neuroepithelial cells in the vomeronasal organ (VNO) project axons to the first AOS circuit, the accessory olfactory bulb (AOB). The AOB receives all of its synaptic inputs within a densely packed glomerular layer. In mice, this layer covers less than a square millimeter of the brain surface and is roughly 150 μm deep, in principle allowing optical observation of nearly all synaptic inputs into the AOB in a single experiment. An important difference between the AOB and the MOB is that VSNs expressing the same receptor gene (members of a "VSN type") target multiple AOB glomeruli, and do so with significant variability across experimental subjects [9, 80]. Until now, the only studies of the organization of the glomerular layer have been anatomical, in which one [9, 80] or a few [105] VSN types were tagged with a fluorescent label. Such studies provide a precise but narrow snapshot of the organization of AOB inputs. Moreover, because the molecules that activated VSN types were unknown, the relationships between glomerular receptive fields and physical positions have remained unexplored.

However, any attempt to determine the functional organization of the AOB must address a number of technical obstacles. AOB glomeruli are small (10–80 μm in diameter), variable in shape, and stacked on top of one another in depth, so obtaining an exhaustive functional map requires methods to quickly image activity in three dimensions throughout large volumes. We combined *ex vivo* methods that expose the AOB surface [62] with calcium imaging via objective coupled planar illumination (OCPI) microscopy [43]. By stimulating VSNs with AOS odorants, including urine from different developmental stages and sulfated steroids [70], we obtained the first large-scale functional images of the AOB glomerular layer. Our results identify organizational features across spatial scales, and reveal a modular organization in this circuit that physically juxtaposes certain inputs and selectively disperses others.

3.3 Results

We studied AOBs from adult male transgenic mice expressing the Ca2+-sensitive fluorescent protein GCaMP2 in the cytoplasm of VSNs [39]. We imaged GCaMP2 fluorescence in the glomerular layer of the AOB while stimulating peripheral VSNs with mouse urine and sulfated steroids in live *ex vivo* preparations of the AOS [62] (Figure 3.3.1a). Image stack dimensions were approximately 700 μm along both the anterior-posterior and medial-lateral axes and nearly 200 μm deep into the tissue (Figure 3.3.1b). These image stacks encompassed the entire anterior AOB (aAOB) and approximately 1/3 of the posterior AOB (pAOB, Figure 3.3.1b, Supplementary Movie 1) and were acquired every 5 seconds while stimuli were delivered to the VNO. Responses were recorded continuously for periods up to an hour and forty minutes.

Sex-specific glomerular maps are activated by mouse urine.

We hypothesized that male- or female-responsive glomeruli might occupy specific spatial domains within the aAOB. Previous electrophysiological recordings identified aAOB mitral cells responding to dilute male and female urine, without clear evidence of sex-dependent spatial organization [41].

However, mitral cells possess extensive dendritic arbors with connections to multiple glomeruli spanning large distances [105, 25, 110], which might complicate understanding of local circuits. We observed fluorescence intensity changes in the glomerular layer when we stimulated the VNO with 100-fold dilute adult, sexually-naive BALB/c female and male mouse urine, but not with Ringer's control saline (Figure 3.3.1c). As in previous studies of male- and female-selective neural responses, we pooled urine from many individual mice in order to stimulate sex-specific responses that represent the "average" of each sex. We calculated a response reliability index (RRI, which reports signal-to-noise ratio) for each image voxel by normalizing the fluorescence changes to the across-trial noise (Figure 3.3.1d). We used RRI values to identify regions of interest (ROIs) representing putative glomeruli. These glomerular ROIs showed stimulus-dependent increases in fluorescence, consistent with previous Ca2+ imaging from VSNs [39, 95] (Figure 3.3.1e). In the AOB, glomerular boundaries are often poorly-defined by anatomical criteria [9], but when visible these boundaries aligned well with activated ROIs (Figure 3.3.1f). Moreover, GCaMP2 activation highlighted regions that could not be distinguished based on morphological cues alone (Figure 3.3.1f).

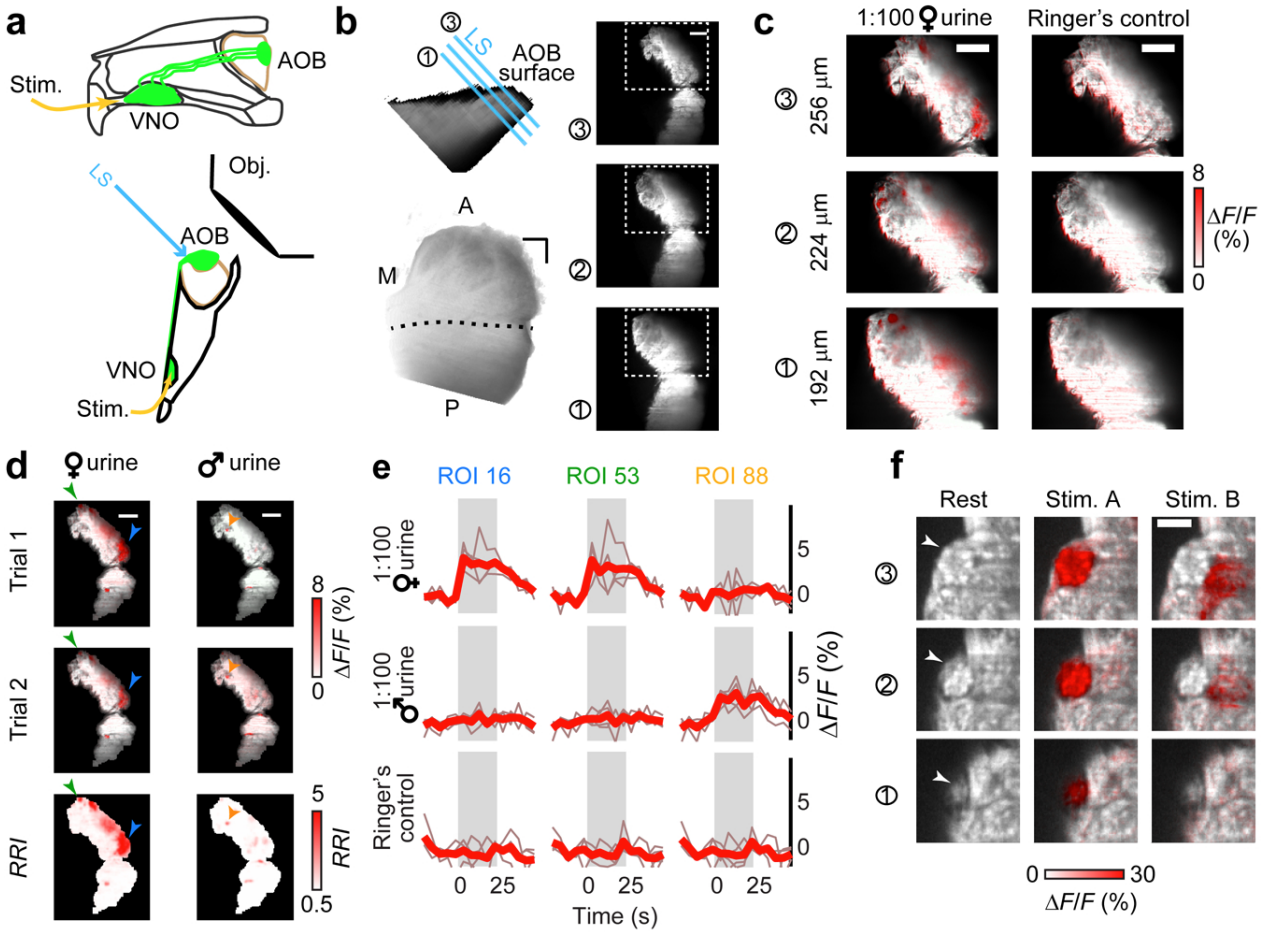

Figure 3.3.1: Functional presynaptic Ca^{2+} imaging in the AOB.
(a) Midline (top) and ventral (bottom) schematic of the OCPI imaging setup for *ex vivo* preparations. VSNs and their axons are highlighted in green. LS: light sheet used to excite fluorescence. Obj: microscope objective. (b) Top-left: side-view of AOB glomerular layer. Cyan lines illustrate 3 positions of the light sheet. Right: images at three light sheet positions. Bottom-left: 3D rendering of the AOB, as seen from the surface. M, A, P: medial, anterior, posterior. Dashed line indicates the *linea alba*, the visible division between the aAOB and pAOB. (c) GCaMP2 fluorescence changes during VNO stimulation with dilute BALB/c female urine at the light sheet positions indicated in b. (d) Glomerular ROIs were defined based on ΔF/F intensity and response reliability index (RRI), a measurement of the across-trial signal/noise. ΔF/F responses to 1:100 BALB/c female (left) and male (right) mouse urine are shown for two different trials (top2 rows). The RRI across 5 trials is shown in the bottom row. Arrowheads indicate the ROIs evaluated in e. (e) Fluorescence in 3D glomerular ROIs was evaluated during peri-stimulus image stacks and compared to the response to Ringer's control saline. The stimulus timing is indicated by gray shading. Thin traces: individual trials, bold traces: across-trial mean. (f) Glomerular boundaries (arrowheads) were evident in the GCaMP2 baseline fluorescence in certain image frames (left). Stimulus-responsive voxels often followed visible anatomical boundaries (middle, 10 µM epipregnanolone sulfate). Nearby voxels activated by other stimuli (right, 10 µM 5-androsten-3β, 17-diol disulfate) did not cross visible glomerular boundaries. Images represent mean ΔF/F across 4 trials. Three adjacent optical sections are shown.
Scale bars: b-d, 100 µm; f, 20 µm.

To compare male and female urine-responsive glomerular maps, we aligned AOBs to visual boundaries in each image (Figure 3.3.2; see Methods 2). Consistent with previous reports [43], we observed strong aAOB responses to 1:100 BALB/c female urine (Figure 3.3.2a). The sum volume of all glomeruli activated by 1:100 BALB/c female urine was 4-fold larger than was activated by 1:100 BALB/c male urine (4.4 $\pm$ 1.6 fold, n = 8, p = 0.043, Figure 3.3.2a, b). A much larger fraction of male urine-responsive than female urine-responsive voxels were located in the visible regions of the pAOB (32 $\pm$ 8% male versus 2 $\pm$ 1% female; p = 0.007; n = 8; Figure 3.3.2b). Female urine-responsive ROIs tended to be larger than male urine-responsive ROIs (Figure 3.3.2c, p = 0.032 Kolmogorov-Smirnov test). Because ROI volumes increase with the intensity of the $\Delta F/F$ response, this effect may be influenced by stronger maximal activation by BALB/c female urine than male urine, but might also suggest that female urine-responsive glomeruli possess a larger synaptic territory in the AOB.

We observed a small but significant number of ROIs that responded to both male and female urine (Figure 3.3.2a, d). To ensure that this effect was not due to inclusion of very weak responses to male urine, we evaluated glomerular ROI responses at multiple thresholds. The overlap persisted until very high thresholds, confirming that these glomerular ROIs were activated by cues found in both male and female urine (constituting 4 $\pm$ 3% of female and 9 $\pm$ 4 % of male urine responsive voxels at $\Delta F/F > 2\%$, n = 8, Figure 3.3.2d). This population represented a larger fraction of the male urine-responsive ROIs, owing largely to the larger overall pool of female-responsive ROIs.

Glomerular maps encode both sex and maturity from urine

If the only function of the AOS were to distinguish sex, one might naturally wonder why so many glomeruli respond to female urinary cues. The four-fold difference in overall volume of the AOB glomerular layer activated by male and female urine mirrors observed differences in the number of VSNs demonstrating sex selectivity for urine24 . Given that a small number of sex-selective VSNs and AOB neurons is theoretically sufficient for sex classification [1], we hypothesized that some of the abundant female urine-selective glomeruli may encode biologically-relevant features

other than sex, for example sexual maturity [39]. We therefore compared glomerular activity maps generated by VNO stimulation with juvenile (P21), gonadectomized, and sexually mature urine from the same BALB/c mouse strain (see Methods 3).

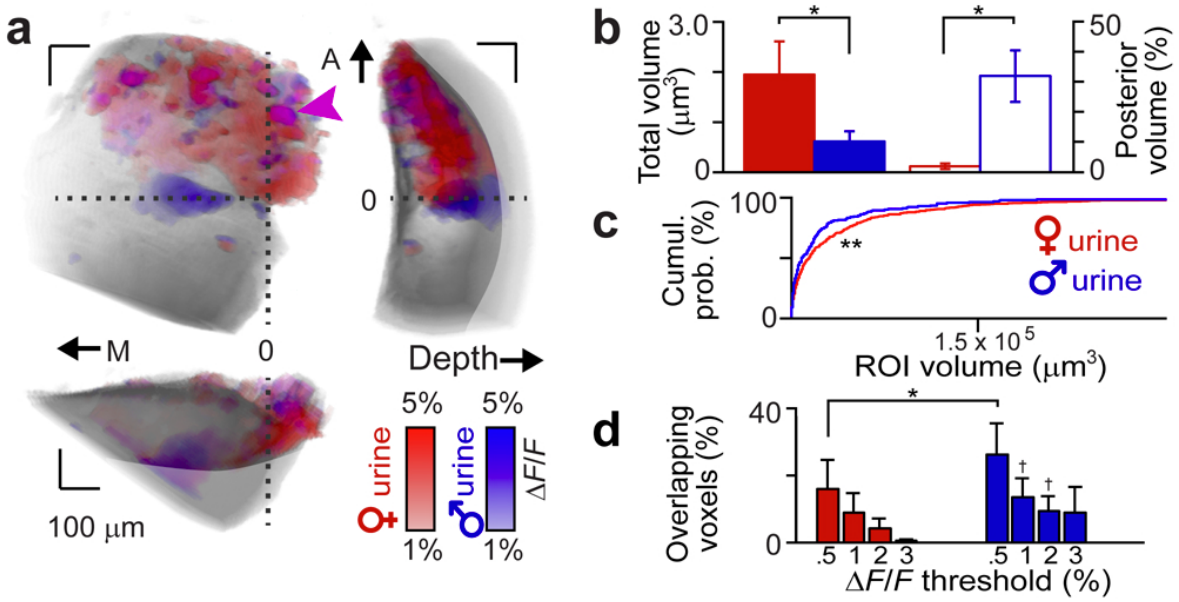

Figure 3.3.2: Overlap and distribution of adult BALB/c male and female urine activity maps. (a) Glomerular activity maps to VNO stimulation with BALB/c adult male or female urine. Bi-planar fits were made between the *linea alba* and the AOB surface to establish orthogonal (medial/lateral, anterior/posterior, and depth) axes. A reference point was chosen along the *linea alba* at its intersection with the AOB lateral edge (horizontal dashed line). Blue voxels show male urine responses, red voxels show female urine responses, and magenta colored voxels (arrowhead) show glomeruli responding to both. M, A: medial, anterior. 0: reference position. Voxels lying below the horizontal dotted line are considered to be in the pAOB. (b) Total volume (filled bars, left ordinate) and fraction of voxels in the pAOB (open bars, right ordinate) of female (red) and male (blue) urine-responsive voxels. (c) Cumulative probability histogram of the volume of female (red line) and male (blue line) urine-responsive ROIs. (d) Overlap between male and female glomerular response maps across ΔF/F thresholds. * and †reflect $p < 0.05$ and $p < 0.1$, respectively (paired Student's t-test between male and female). ** reflects $p < 0.05$ (K-S test, $n = 8$ animals). Error bars reflect s.e.m.

Each of these 6 urinary cues activated at least one glomerulus (Figure 3.3.3). Glomerular maps generated by this stimulus set revealed the rich combinatorial nature of responses in the AOB (Figure 3.3.3a-c). Many of the glomeruli demonstrated selectivity for certain urines, indicated by an increase the numbers of selective ROIs and a decrease in the number of non-selective ROIs at higher ΔF/F thresholds (Figure 3.3.3d). The large majority of ROIs activated by sexually mature

female urine also responded to juvenile and/or gonadectomized urine of one or both sexes (86 $\pm$3% at $\Delta F/F > 2\%$, $n = 5$; Figure 3.3.3a, c, e). Thus, only a small fraction of the female urine-responsive aAOB glomeruli are exclusively tuned, or "selective", for urine from adult intact females at this concentration (Figure 3.3.3e). This was not the case for male urine-responsive glomeruli, which showed almost no overlap between intact, juvenile, and castrated males (Figure 3.3.3b). Including all stimuli, we found that the large majority of intact male urine-responsive ROIs were also selective for this stimulus (70 $\pm$ 14%, $p < 0.05$ one-way ANOVA, $n = 5$, Figure 3.3.3e). Intact adult female urine responses were nearly entirely abolished by sulfatase treatment (Supplementary Figure 3.5.1, Methods Chapter 2.2 and 2.3), confirming that sulfated compounds dominate the AOS activity induced by female urine [70] .

Evaluation of all urine responses revealed specific, repeated tuning patterns among aAOB glomeruli (Figure 3.3.3f). Clusters displayed responsivity for anywhere from one to five of the six stimuli, with approximately half of the ROIs dominated by one or two stimuli. This classification of glomeruli into types serves as a foundation for analysis of the spatial organization of responses to natural stimuli (Figure 3.3.3g, Supplementary Figure 3.5.1).

Figure 3.3.3

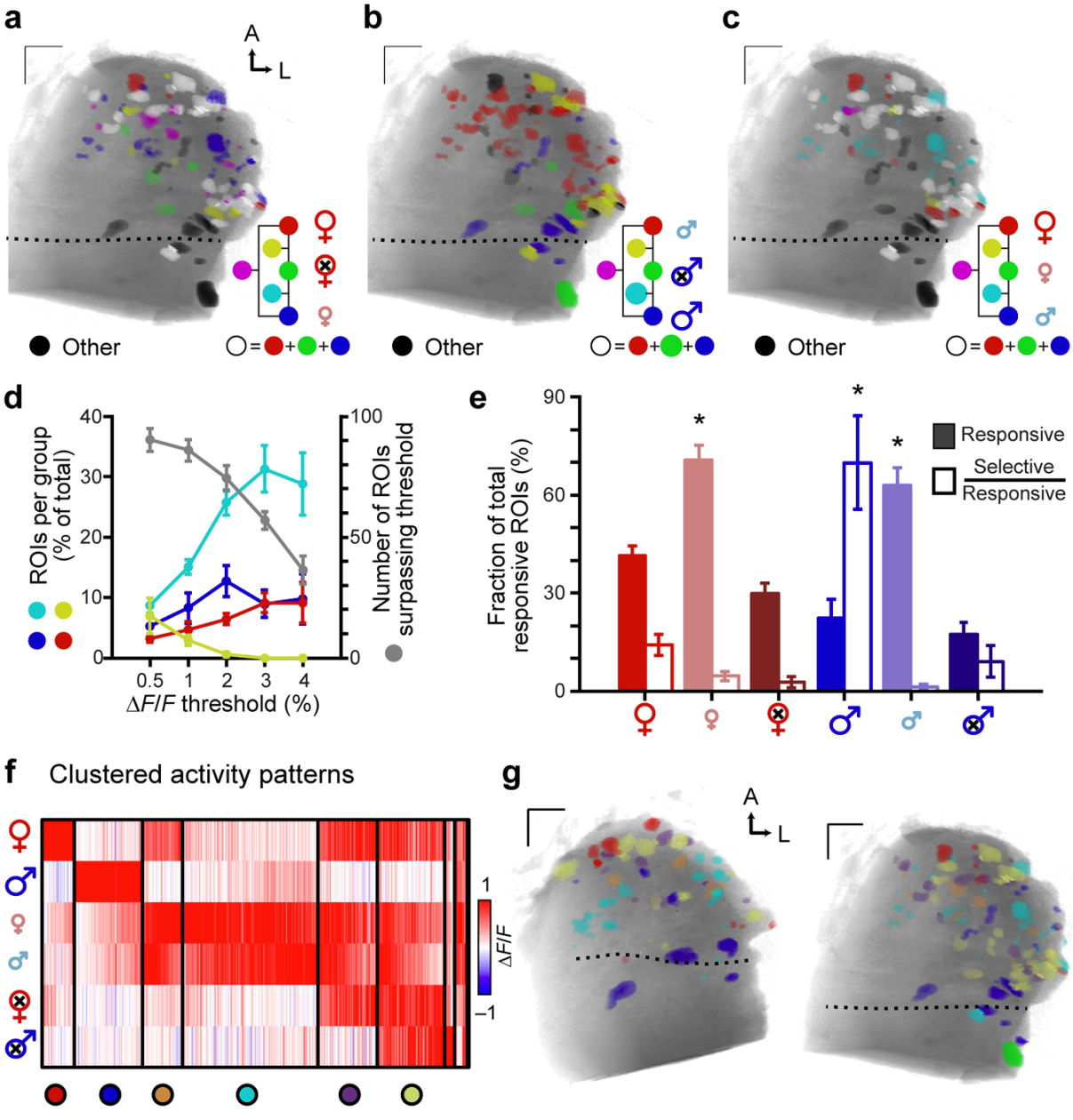
a
b
c
A
L
Other
Other
Other
d
ROIs per group (% of total)
Number of ROIs surpassing threshold
ΔF/F threshold (%)
e
Fraction of total responsive ROIs (%)
Responsive
Selective
Responsive
f
Clustered activity patterns
ΔF/F
g

Figure 3.3.3: Glomerular maps activated by mouse urine across sex and maturity.
(a-c) Example glomerular response maps to dilute BALB/c urine from different sexes and sexual maturities. Colored voxels indicate responsiveness to 3 selected urines in each panel ($\Delta F/F > 2\%$). Color mixtures indicate glomeruli that responded to more than one of the highlighted urines (yellow: red + green, magenta: red + blue, cyan: blue + green, white: all 3). Glomeruli that responded to urine cues other than those highlighted in each panel are colored black. (d) Increasing the $\Delta F/F$ threshold reduced the total number of glomeruli (gray symbols, right ordinate), and the prevalence of nonselective glomeruli (yellow symbols, left ordinate). Selectivity for sexually mature female (red symbols), sexually mature male (blue), and juvenile (cyan) urine increased at higher thresholds. (e) The percentage of glomerular ROIs responsive (filled bars) and selective (open bars) for BALB/c mouse urine of different sexes and sexual maturities ($\Delta F/F > 2\%$). (f) Cluster analysis of glomerular tuning to 6 urines. Each thin vertical stripe shows an individual ROI and rows indicate the stimuli. Vertical black bars divide the clusters. The color of each thin pixel indicates the normalized $\Delta F/F$ for each ROI and stimulus. Colorized circles (bottom) assign unique colors to identify members of each cluster in g. (g) Functional glomerular maps organized by glomerular tuning. ROI color indicates membership in the associated cluster in f. Members of the two smallest clusters are omitted. Dotted lines indicate the position of the *linea alba*. Scale bars: 100 μm. Error bars represent s.e.m. ($n = 5$). Asterisks: $p < 0.05$ (one-way ANOVA).

Sets of functionally-defined glomeruli form spatial modules.

Because the evaluation and analysis of natural stimuli by the AOB might be based on local circuitry, we wondered whether glomeruli exhibited patterns in the relationship between their receptive fields (Figure 3.3.3f) and their spatial organization (Figure 3.3.3g). To evaluate such questions statistically, we compared the observed positional patterns against those that arose from randomly shuffling the cluster label assigned to each ROI.

Several glomerular clusters were preferentially spatially distributed along the 3 orthogonal axes (Figure 3.3.4a-b, Supplementary Figure 3.5.1). Intact adult female urine-selective glomeruli (Cluster 1) were preferentially located near the anterior tip of the AOB ($p < 0.05$, $n = 5$, Figure 3.3.4b). In contrast, intact adult male urine-selective glomeruli (Cluster 2) were preferentially located more posteriorly, very near the *linea alba* dividing the aAOB and pAOB ($p < 0.05$, $n = 5$, Fig. 4b). Cluster 3 glomeruli were preferentially located approximately mid-way between Clusters 1 and 2 along the anterior/posterior axis ($p < 0.05$, $n = 5$, Figure 3.3.4b). Cluster 1 glomeruli were frequently among the most medial of all activated glomeruli, and had an unusually-strong tendency to be superficial rather than deep ($p < 0.05$, $n = 5$, Figure 3.3.4b). Cluster 3 glomeruli

were biased towards deeper positions ($p < 0.05$, n = 5, Figure 3.3.4b).

In addition to the regularities in absolute positioning exhibited by three of these clusters, we asked whether there might be reproducible patterns in the relative positioning between two or more clusters [105]. Again using comparisons against shuffled maps (Figure 3.3.4c-f), we found that the largest effects consisted of dispersals: for example, Cluster 1 ROIs (selective for intact adult female urine) and Cluster 4 ROIs (selective for juvenile urine) were much farther apart than expected by chance (Figure 3.3.4c-d; $p < 1e^{-7}$, n = 5). A similar result held for Clusters 1 and 2 ($p < 1e^{-7}$), Clusters 4 and 5 ($p < 1e^{-3}$), and Clusters 4 and 6 ($p < 1e^{-8}$; all n = 5, Figure 3.3.4d-f). We also found two clear instances of preferentially-juxtaposed functional groups (Figure 3.3.4d-f). Cluster 3 (responsive to intact adult female and juvenile urine) and Cluster 4 (responsive to juvenile urine only) tended to be near one another (Figure 3.3.4d-f, $p < 0.01$, n = 5). Likewise Cluster 5 (responsive to all female urines and juvenile male urine) and Cluster 6 (responsive to all urines except intact adult male urine) tended to be closer than expected by chance ($p < 0.01$, (Figure 3.3.4d-f). Clusters 1 and 2, selective for intact adult female urine and intact adult male urine, only showed preferential dispersal with other groups. Clusters 4, 5, and 6 showed preferential juxtaposition in some pairwise comparisons and preferential dispersal in others.

In both cases of selective juxtaposition, the glomeruli were similarly tuned, with the two members of each pair differing by only one response. Selectively dispersed groups, on the other hand, were more dissimilarly tuned (i.e. differing by at least 2 responses). At face value, this suggested that relative spacing among glomeruli may selectively group similarly-tuned inputs and disperse dissimilarly-tuned inputs. Such an organization would suggest that the AOB possesses "identity-based" chemotopy based on relative glomerular position. However, because the blend of odorants in each urine source is unknown, it remains unclear from these data whether preferential juxtaposition and dispersal among glomeruli reflects sensitivity to similar molecules.

Figure 3.3.4

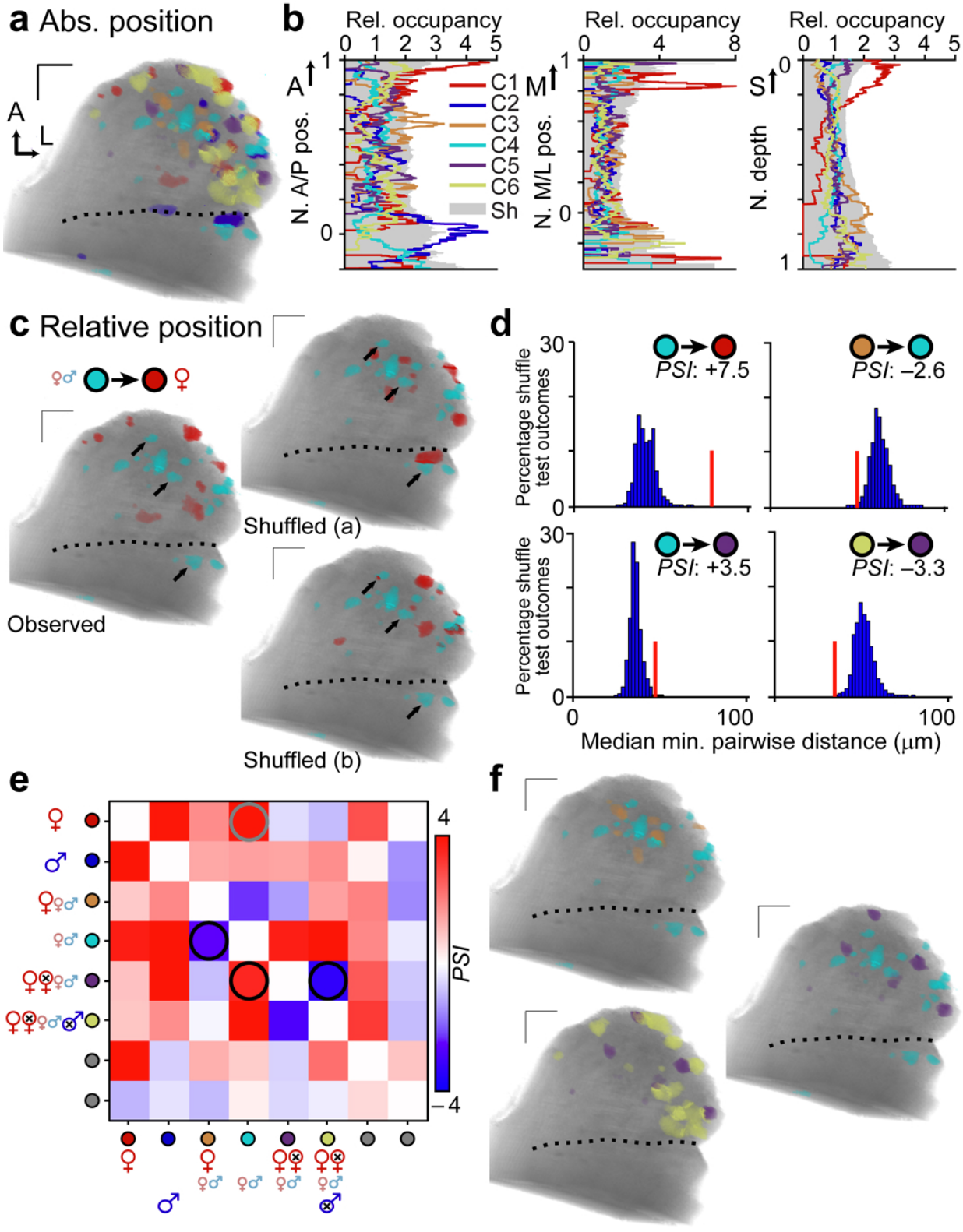
a Abs. position
A
L
b
Rel. occupancy
N. A/P pos.
N. M/L pos.
N. depth
C1
C2
C3
C4
C5
C6
Sh
c Relative position
Shuffled (a)
Observed
Shuffled (b)
d
Percentage shuffle test outcomes
PSI: +7.5
PSI: –2.6
PSI: +3.5
PSI: –3.3
Median min. pairwise distance (μm)
e
PSI
f

Figure 3.3.4: Absolute positions and relative distances between populations of urine-responsive glomeruli.
(a) Representative glomerular activity map, with colors assigned as per Figure 3.3.3f. (b) Histogram of glomerular positions by cluster along the A/P (left), M/L (middle), and depth (right) axes. The tendency for glomeruli of each cluster to be located at various locations along these axes (relative occupancy) was compared to the 95th percentile from a shuffled map (Sh, gray shading). (c) Relative position between glomeruli of Clusters 1-6 was likewise compared to expectations from shuffled maps. Black arrows highlight several juvenile-selective glomeruli (cyan) that are more distant from the nearest sexually mature female urine-responsive glomerulus (red) in the observed case than in the exemplar shuffled cases. (d) Histogram of pairwise glomerular distances from shuffle tests (blue filled bars; 10,000 shuffled comparisons per experiment; n = 5) compared to observed distances (red vertical bar). The colored circles indicate the populations being tested. The physical spacing index (PSI) resulting from this test is shown for each comparison. Positive PSI values indicate preferential dispersal, while negative values indicate preferential juxtaposition. (e) PSI matrix for all pairwise comparisons, averaged across 5 separate experiments. Red hues indicate preferential dispersal, while blue hues indicate preferential juxtaposition. The gray circle highlights the comparison shown in c and the top-left histogram in d. Black circles highlight the three other comparisons in d and shown in f. (f) Glomerular maps highlighting the comparisons indicated by black circles in e. Dotted lines indicate the position of the *linea alba*. A: anterior. M: medial, L: lateral, S: surface. All scale bars: 100 μm.

Steroid-responsive glomeruli span the aAOB and pAOB.

To make explicit comparisons between glomerular spatial organization and odorant chemical structures, we generated maps to a panel of 11 synthetic sulfated steroids, a prominent class of natural ligands [70]. This panel of sulfated steroids, spanning the androgen, estrogen, pregnanolone, and glucocorticoid families, was delivered at 10 μM, a concentration previously found to activate at least 10 functionally-separable VSN populations [62, 95]. Across 10 adult experimental subjects, we identified 1078 glomeruli that responded to at least one of the 11 synthetic sulfated steroids with $\Delta F/F$ greater than 1%. We observed reliable, concentration-dependent glomerular activity across multiple stimulus trials (Figure 3.3.5a-b, Supplementary Figure 3.5.2, and Supplementary Movie 2). Within glomerular regions of interest (ROIs), fluorescence peaked within the first image stack (within 5 s), and then accommodated over subsequent image stacks (Figure 3.3.5b). Single-plane imaging at 10 Hz indicated that fluorescence increases began within 1-2 s of stimulus onset, and peaked within 3-5 s (Supplementary Fig. 2, Supplementary Movie 3). The vast majority (1012 of 1078, 94%, $\Delta F/F > 1\%$, n = 10) of steroid-responsive ROIs were located in the aAOB,

but were widely distributed within this subregion (Figure 3.3.5c-f, Supplementary Figure 3.3.3, Supplementary Movie 4). Since V1R-expressing VSNs selectively innervate the aAOB [9, 80], these results confirm that many VSNs expressing V1Rs are sensitive to sulfated steroids [49, 95].

We observed a notable number of glomeruli responsive to sulfated pregnanolones in the posterior AOB (56 of 576 pregnan-responsive glomeruli, representing 85% of all posterior responses). These glomeruli likely derive from a pregnanolone-responsive population of basal VSNs [95]. We further investigated this pAOB activity by comparing activity maps at different sulfated steroid concentrations (Supplementary Figure 3.5.2). We found reliable aAOB responses to most of the sulfated steroids in the panel starting at 1 μM (Supplementary Figure 3.5.32), consistent with previous results[70, 3]. Glomeruli responsive to allopregnanolone sulfate (P3817) were found in the pAOB at 10 μM (Supplementary Fig. 2). At 100 μM, activity in the pAOB increased markedly to another sulfated pregnanolone, P8200, but less so to other sulfated steroids (Supplementary Figure 3.5.2). Since the pAOB receives input from V2R-expressing VSNs, these results suggest that sulfated pregnanolones elicit activity in both major vomeronasal receptor families.

Because sulfated steroid abundance is high in BALB/c female urine [70], we investigated spatial relationships between synthetic steroid ROIs and female urine-responsive ROIs. We observed many glomerular ROIs that were activated by both 10 μM Q1570 and 1:100 intact adult BALB/c female urine, consistent with previous results [45, 70] (Supplementary Figure 3.5.4). We also observed many glomeruli that responded to both 10 μM epitestosterone sulfate (A6940) and 1:100 BALB/c female urine (Supplementary Figure 3.5.4), suggesting that female urine contains odorants that activate the same inputs as certain sulfated androgens. Glucocorticoid overlap was also seen for juvenile male and female and ovariectomized female urine (Supplementary Figure 3.5.4), suggesting these glucocorticoids are present at comparable concentrations in these urine sources. Also apparent in this comparison was the low incidence of overlap between these sulfated steroids and intact adult male urine (e.g. Q1570 overlap was 7 $\pm$1% for female urine and 0 $\pm$ 0.1% for male urine, $p < 0.05$ Kruskal-Wallis test, $n = 7$, Supplementary Figure 3.5.4).

Figure 3.3.5

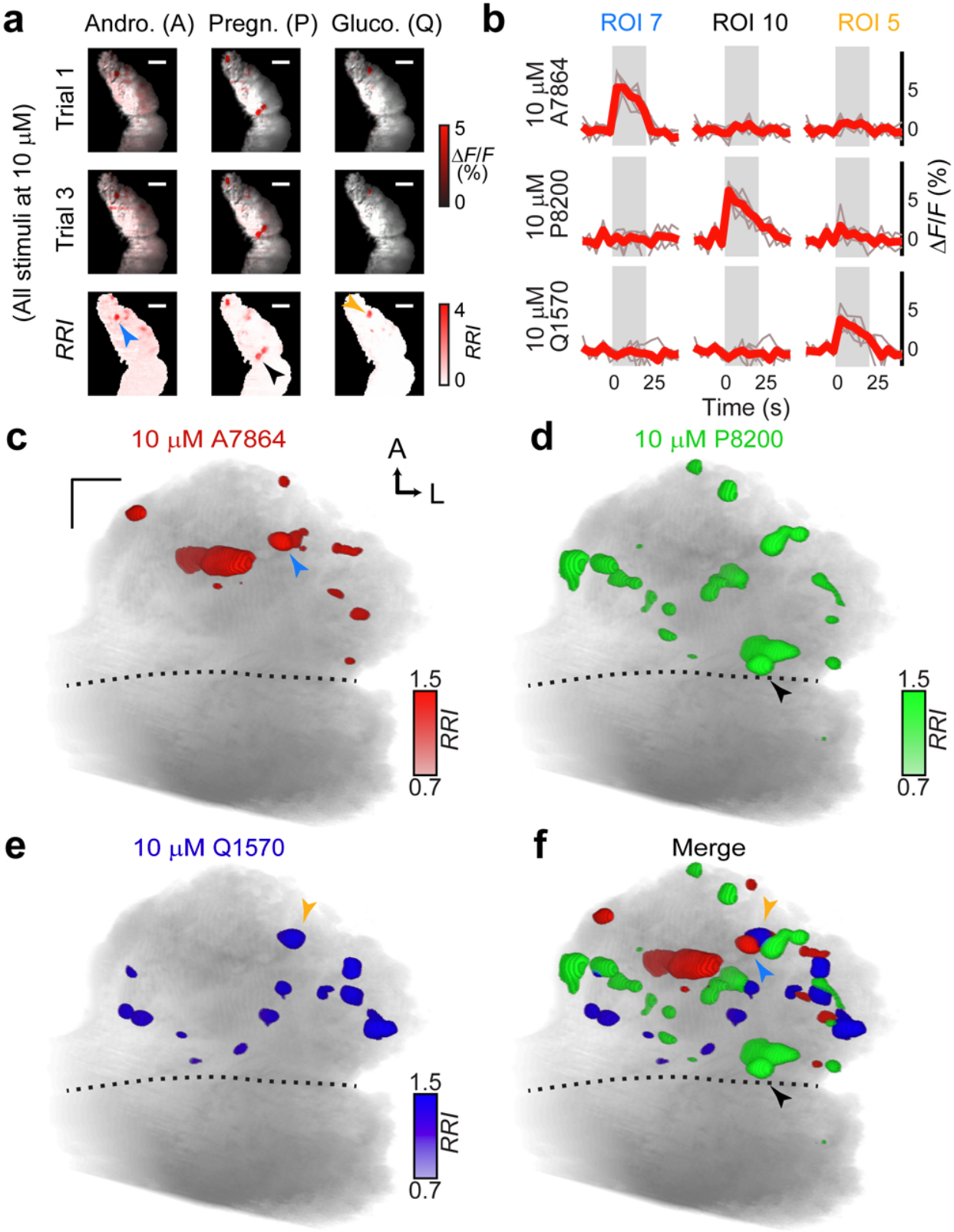
a
Andro. (A)
Pregn. (P)
Gluco. (Q)
(All stimuli at 10 μM)
Trial 1
Trial 3
RRI
5
ΔF/F (%)
0
4
RRI
0
b
ROI 7
ROI 10
ROI 5
10 μM A7864
10 μM P8200
10 μM Q1570
5
0
ΔF/F (%)
0 25
Time (s)
c
10 μM A7864
A
L
1.5
RRI
0.7
d
10 μM P8200
1.5
RRI
0.7
e
10 μM Q1570
1.5
RRI
0.7
f
Merge

Figure 3.3.5: Sulfated steroid VNO stimulation generates robust activity in the aAOB. (a) aAOB glomeruli were activated by VNO stimulation with 10 μM sulfated steroids from different classes (red colored voxels). Two trials per stimulus are presented (top rows) along with the RRI (bottom row) for a sulfated androgen (A7864), pregnanolone (P8200), and glucocorticoid (Q1570). Arrowheads in the bottom row indicate glomeruli highlighted in b - f. (b) ROIs encompassing sulfated steroid-responsive glomeruli were analyzed in the peri-stimulus region (gray rectangle). Thin traces show responses to individual trials, and bold traces represent the average response. (c) Activity maps generated by VNO stimulation with 10 μM A7864 were confined to the aAOB. The blue arrowhead marks ROI 7 from a - b. (d-e) Glomeruli activated by the sulfated pregnanolone P8200 and glucocorticoid (Q1570) were also located predominantly in the aAOB. Black and orange arrowheads mark ROIs 10 and 5 from a - b. (f) Merged glomerular maps from c - e. Scale bars: 100 μm.

Glomerular juxtaposition does not infer similar tuning.

To determine whether individual glomeruli are organized by their tuning for molecular features, we first analyzed the glomerular activity patterns to synthetic sulfated using clustering algorithms [62, 95]. We found that glomerular responses to these steroids fell into at least 10 classes of reproducible patterns (Figure 3.3.6a-c). These classes match previous physiological recordings in VSNs [62, 95], and nearly every glomerulus (1071/1078, 99%) could be assigned to one of these classes. Cluster features remained consistent across response thresholds (Supplementary Figure 3.5.5). This suggests that glomerular responses to sulfated steroids reflect these functionally-defined peripheral populations.

To compare receptive fields to molecular features of the ligands (Figure 3.3.7a), we calculated 1,666 molecular descriptors [35] for each sulfated steroid in the panel, then computed the average pairwise Euclidean distance between the normalized odorant descriptors sensed by each VSN class. This produced quantitative measurements of receptive field differences between all VSN classes (Figure 3.3.7b). The distinctions among most VSN response classes had a clear corresponding structural basis – compounds with similar molecular features were more likely to co-activate the same glomerulus – but some classes showed selectivity for steroids differing in subtle aspects poorly captured by these descriptors (e.g. the 3 sulfated pregnanolones).

The absolute glomerular positions for most VSN classes showed no evidence of selective positioning along the 3 orthogonal axes. The exceptions were a strong posterior bias among Class

5 glomeruli, selective for allopregnanolone sulfate (P3817), and a bias among Class 7 glomeruli (selective for 17α-estradiol disulfate) to lie laterally along the *linea alba* (Supplementary Fig. 6). Visual inspection of activity maps for similarly tuned VSN classes revealed no evidence of a positive link between physical closeness and receptive field similarity (Figure 3.3.7c). For example, the three pregnanolone-responsive classes had highly similar receptive fields, but were not similar in their projection patterns (Figure 3.3.7b-c). At face value, these data indicate that at fine spatial scales, VSNs sensing highly similar odorants do not necessarily project to physically adjacent locations.

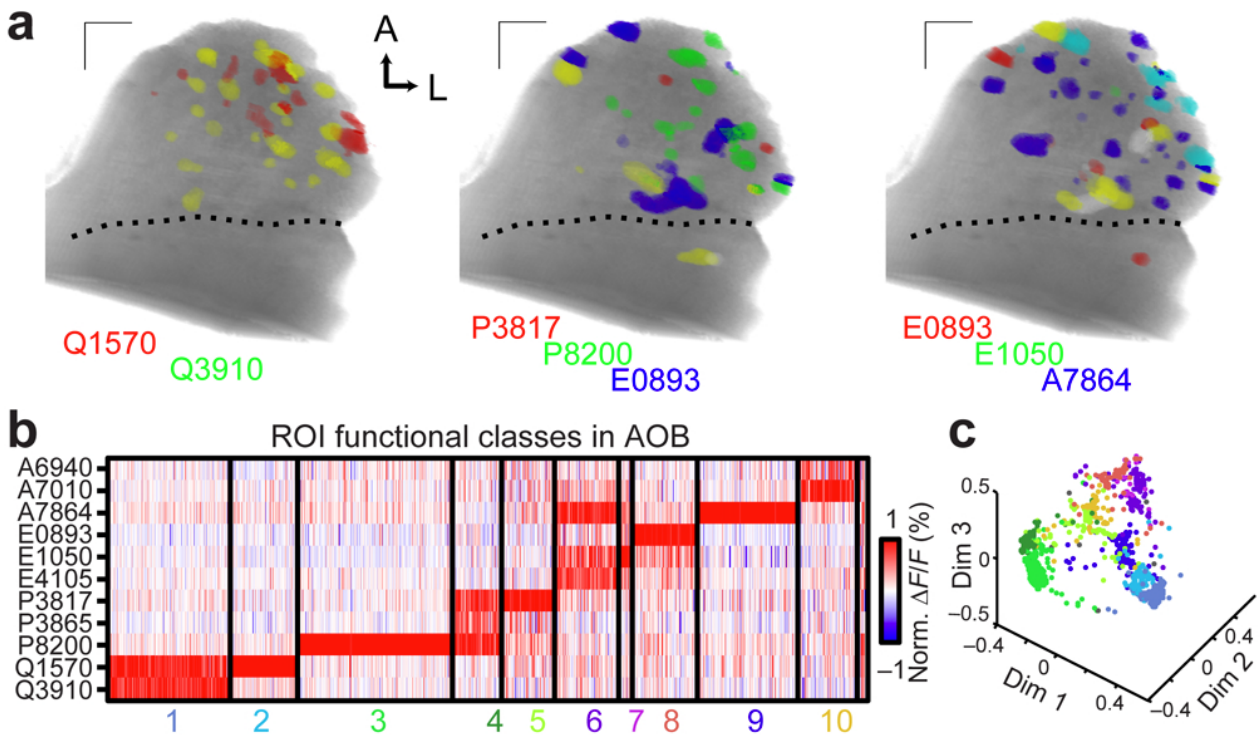

Figure 3.3.6: Glomerular activity patterns identify functional VSN classes.
(a) Glomeruli responding to the indicated steroids (10 μM) with $\Delta F/F > 1\%$ were colorized according to stimulus. Glomeruli responding to more than one steroid are indicated by color mixtures (yellow: red/green, magenta: red/blue, cyan: green/blue, white: red/green/blue). Scale bars: 100 μm. (b) 1078 glomerular responses across 10 experiments to the 11-steroid panel match previously-identified VSN functional classes. Each thin vertical stripe shows the activity pattern of a single glomerular ROI, and each row shows responses to a single sulfated steroid (10 μM). A small unclustered group (far right) consisted of less than 1% of all ROIs. (c) Multidimensional scaling (first 3 dimensions) of the ROI responses to the 11 sulfated steroids in the stimulus panel. Colors of the points correspond to the clusters in b.

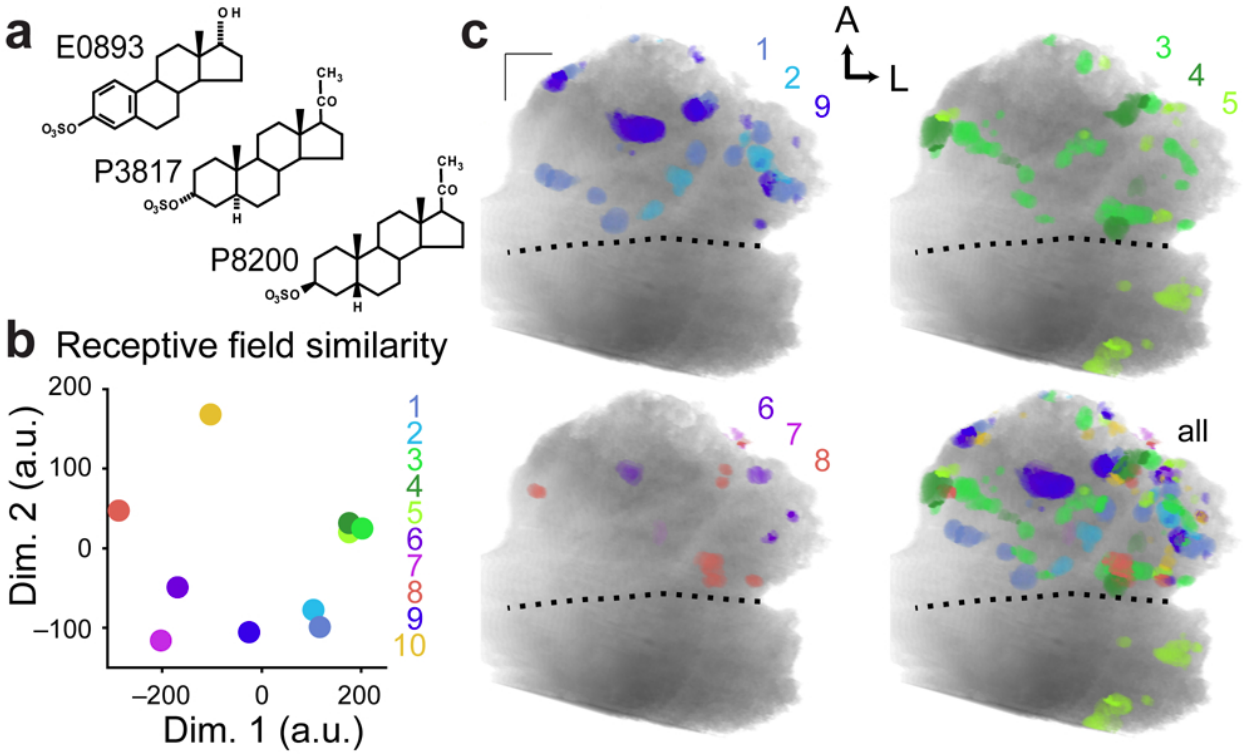

Figure 3.3.7: Glomeruli of similarly-tuned VSN classes are distributed across the AOB. (a) Chemical structures for 17α-estradiol sulfate (E0893), allopregnanolone sulfate (P3817), and epipregnanolone sulfate (P8200), 3 of the 11 sulfated steroids in the panel. Responses to these steroids were critical in identifying Class 3 (P8200-dominated responses), Class 4 (responsive to P3817 and P8200), Class 5 (P3817-dominated responses), and Class 8 (E0893-dominated responses). E0893 and P3817 have multiple structural differences while P3817 and P8200 are stereoisomers. (b) Relative differences in the receptive fields of each glomerular class were calculated across 1,666 molecular descriptors and displayed here using 2-dimensional nonclassical multidimensional scaling. Symbols for Classes 4 and 5 were shifted slightly from underneath the symbol for Class 3 to allow better visualization. (c) Glomerular activity maps for classes with similar receptive fields. Color similarity indicates similar receptive fields, and color opponency indicates disparate receptive fields.

We next sought to determine whether any of these functionally-defined classes showed evidence of higher-order spatial relationships. We compared pairwise distances between the 45 combinations of VSN class pairs, and identified two tightly juxtaposed pairs. The most tightly juxtaposed pair was Class 4 - 8 ($p < 1e^{-5}$, Figure 3.3.8a; Supplementary Movie 4). The second pair was Class 6 - 10 ($p < 0.01$, $n = 10$). As was the case for our investigation of spatial similarity among urine-responsive glomeruli (Figure 3.3.4), we observed glomeruli for many VSN class pairs (14 total) that were preferentially dispersed compared to shuffle test expectations ($p < 0.05$, $n = 10$, Figure

3.3.8b). In all, 16 of the 45 VSN class pairs (36%) showed a reciprocal statistically significant spatial relationship (Figure 3.3.8b). We also observed several non-reciprocal significant spatial relationships (for example, Class 1 - 3, Figure 3.3.8b), indicating tight juxtaposition between subsets of glomeruli in certain class pairs.

The juxtaposed glomeruli in the Class 4 - 8 pair arose from VSN classes with the most distant receptive fields in our analysis (Figure 3.3.8c-d). The Class 6 - 10 pair did not possess strongly similar or dissimilar receptive fields compared to other pairs (Figure 3.3.8c-d). Among the most spatially dispersed pairs was Class 3 - 5, sensitive to pregnanolone stereoisomers, the most molecularly-similar ligands in our stimulus set (Figure 3.3.7a, c). To test whether there was a consistent relationship between glomerular receptive fields and relative spacing, we generated a spring embedding model in which receptive field similarity was used as the spring constant and spatial similarity was used for the distance between points (Figure 3.3.8d). The model energy necessary to produce the observed isomap (i.e. the product of spatial distance and the spring constant) was near the mean values expected from shuffled maps (observed energy 7.1, Gaussian fit of shuffle test: $\mu = 6.8$, $\sigma = 0.8$, $p = 0.63$). This indicates that, in aggregate, the preferential juxtaposition and dispersal of AOB glomeruli is not organized by the similarity or dissimilarity of their odorant tuning.

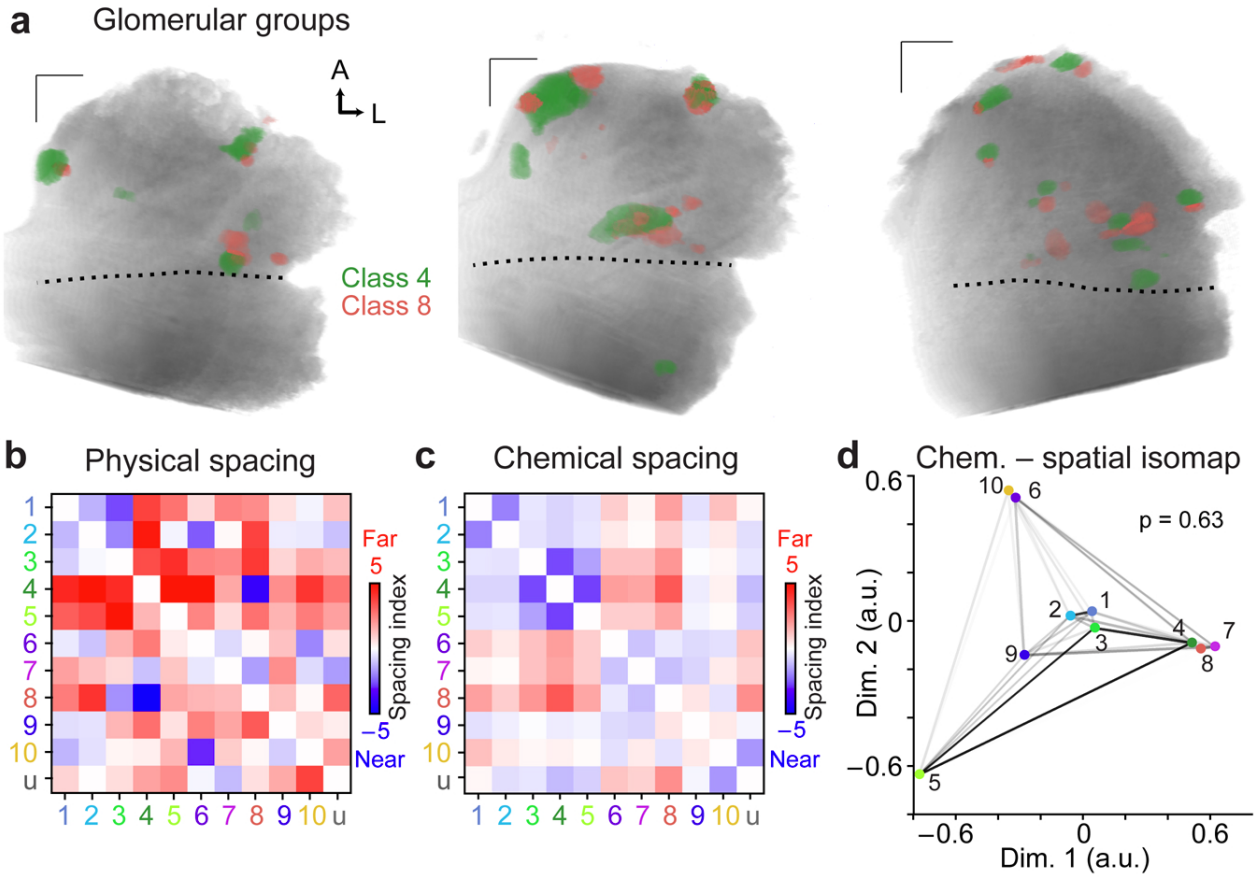

Figure 3.3.8: Glomerular juxtaposition does not imply sensitivity to similar odorants. (a) Glomeruli from Class 4, broadly responsive to sulfated pregnanolones, and Class 8, selective for sulfated estradiols, were found in tight proximity in each of ten adult AOBs. (b) Physical relative spacing index for all VSN class pairs (n = 10). Blue hues indicate pairs with tight spacing, and red hues those with distant spacing. Elements above the diagonal represent the "forward" test (i.e. from ordinate class to abscissa class) and elements below the diagonal represent the "reverse" test. Group "u" represents the unclustered population from Figure 6b. (c) Chemical relative spacing index for all VSN class receptive fields. (d) Isomap analysis of physical spacing with receptive field similarity. The closeness of each colored point to others indicates the tendency for that pair to be spatially juxtaposed. The darkness of the shaded connecting lines indicates the similarity of receptive fields, with black representing the most similar and white the most dissimilar. The unclustered group is omitted. The p-value reflects the probability that the observed relationships indicate preferential juxtaposition of similarly tuned inputs (spring embedding model, 100,000 simulations). A: anterior, L: lateral. Scale bars 100 μm.

3.4 Discussion

A distributed glomerular code for sex and maturity

Many individual VSNs and AOB mitral cells are selective for the sex, strain, and species of urine sources [39, 61, 41, 1, 57, 10, 44]. Several studies have demonstrated that the aAOB and pAOB become strongly active during exposure to female or male urinary cues, respectively [28, 63]. However, male urine also has been shown to activate the aAOB, and female urine in the pAOB [43, 48], suggesting that each of these major AOB subregions possess the capacity to compare sex-selective signals. The majority of AOB glomerular responses to VNO stimulation with 100-fold diluted mouse urine of both sexes were located in the aAOB, suggesting that, at these concentrations, this V1R-receptive AOB region is a prominent site of sex discrimination.

We compared activity patterns induced by intact adult urine to those generated by urine of sexually immature or gonadectomized animals. This combinatorial approach revealed that only 14% of the ROIs that respond strongly to intact BALB/c female urine responded exclusively to this urine type, with the most prominent sources of overlap being juvenile urine of either sex. Thus, the odorants present in sexually mature BALB/c female urine activate VRs that are also sensitive to odorants in sexually immature urine. These broadly responsive inputs are poor candidates for performing discrimination tasks that underlie specific behavioral responses to sexually mature adult females, and may instead be involved in multi-glomerular comparisons between non-male individuals. Glomeruli selective for sexually mature female urine were preferentially located along the anterior aAOB border and at superficial depths.

Glomeruli selective for sexually-mature male urine were preferentially located near the posterior edge of the aAOB near the *linea alba*. Many fewer ROIs responded to intact adult male urine, but most (70%) of these ROIs were exclusively activated by it. As such, the activity generated by the AOS in response to mature male urine appears to be more directly indicative of a sexually intact BALB/c male. This also indicates that sexually mature males, but not juvenile or gonadectomized males, cease producing urinary odorants common to sexually mature female mice. This implies

that changes in metabolic pathways in intact males result in halted production, metabolic shunting, or accelerated degradation of many AOS odorants.

Our combinatorial approach to studying AOB glomerular maps also revealed that juvenile female and male urine were the most potent sources of aAOB activators in our study, activating nearly two-fold more glomerular ROIs than even intact BALB/c female urine. Nearly one-third of these ROIs were exclusively activated by both juvenile male and female urine. Discovery of this population suggests a large number of inputs to the aAOB possess the capacity to discriminate sexually immature animals at weaning age (P21) from sexually mature adults. These inputs are prime candidates for guiding behaviors towards these young animals.

Juxtaposed glomeruli have correlated urine tuning

To date, the clearest indication that the AOB glomerular layer possesses a systematic organization at fine scales came from anatomical studies labeling two or more members of the same "clade" [105] . In these studies, VSNs types in the same clade were found to closely appose their glomeruli [105]. Because clade definitions were based on amino acid homology for the entire receptor, this result suggested a modular glomerular organization that juxtaposes inputs with similar receptive properties. We measured the pairwise distances between glomeruli with different receptive fields for sexually mature and immature urines, and found strong evidence for preferential juxtaposition among two of these glomerular populations. We also found evidence for strong preferential dispersal among other glomerular populations. These findings suggest that relative spacing between glomerular populations may be a prominent "axis" upon which biologically-relevant spatial relationships might be built in the AOB.

The preferentially juxtaposed glomerular groups all responded to juvenile urine of both sexes but differed in their sensitivities to various adult urines. Each of these juxtaposed pairs differed only by sensitivity to just one of these stimuli, whereas each of the preferentially dispersed glomeruli differed by more than one. At face value, this might seem to suggest that preferential glomerular juxtaposition is associated with similar organism status, which would constitute a form

of chemotopy. However, the urinary odorants activating juxtaposed glomeruli may or may not be molecularly similar. To address this question, we performed similar experiments using a defined panel of sulfated steroid odorants known to activate distinguishable VSN populations [61, 95].

Sulfated steroids activate aAOB and pAOB glomeruli.

At the most macroscopic scale, the AOB has a tripartite organization determined by innervation of VSNs expressing receptors from different families [48]. However, how these macroscopic regions correspond to receptivity to defined ligands has scarcely been explored. The 11 synthetic sulfated steroids were chosen to match previously-identified functional groups of similarly-tuned VSNs [61, 95]. The breadth of our stimuli allowed us to compare glomerular activation patterns to chemically similar and distinct odorants. AOB glomerular responses to sulfated steroids showed concentration dependence, with sensitivity to some sulfated steroids at 1 μM. AOB responses to steroids at 1 to 10 μM showed increased peak fluorescence within glomeruli but few changes in the macroscopic activity pattern. This was in stark contrast to the responses at 100 μM, which dramatically changed both the intensity and number of activated glomeruli. At 100 μM, activated glomeruli retained some stimulus specificity, consistent with previous reports [70, 95], and indicating that even at 100 μM sulfated steroids do not gate a nonspecific conductance in VSNs.

The physical location of steroid-responsive glomeruli was dispersed across the aAOB. This is consistent with previous observations that sulfated steroids activate apical [95] and V1R-expressing VSNs [49]. The small (6%) but consistent population of steroid-responsive glomeruli in the pAOB were dominated by glomeruli responding to certain sulfated pregnanolones. This posterior activity was strongly concentration-dependent, but was present in some cases even at 1 μM, suggesting either a displaced V1R-expressing population projects to the pAOB, or that some VSNs expressing V2Rs are sensitive to sulfated pregnanolones.

The glomerular activity patterns across the panel of 11 synthetic sulfated steroids, matched those previously observed in VSNs using multielectrode array recordings [61], and population cal-

cium imaging [95]. This suggests that our experimental setup was capable of accurately producing topographical maps in the AOB downstream of functionally-defined sets of VSNs. Some glomerular ROIs assigned to functional classes possessed lower-intensity activity patterns that resembled those of other classes (see Figure 3.3.6b). These particular ROIs may encompass parts of two anatomical glomeruli.

Glomerular proximity is not based on odorant similarity

In chemical senses, regional specificities are apparent, but scarce evidence of systematic positional relationships between these regions has been found [69]; however, this question has never been considered for the AOB, which is activated by a narrower range of stimuli. We explored the hypothesis that systematically juxtaposed glomeruli have similar receptive fields. Similarly-tuned glomeruli were not always found in tightly-packed groups. This was especially evident for Classes 3-5, responsive to pregnanolone stereoisomers, which showed preferential dispersal rather than juxtaposition. Additionally, the most preferentially juxtaposed pair, Classes 4-8, responded to the most disparate ligands in the study (sulfated pregnanolone and estrogen-selective inputs, respectively). In combination with evidence that receptors within the same clade, at least in some circumstances, target neighboring glomeruli [105], one possible interpretation of this result is that receptor amino acid sequence is more directly related to axonal targeting than to ligand binding. It is worth noting that our functional clustering scheme may lump multiple, similarly-tuned VSN types together. As such, it may be the case that some ROIs correspond to a clump of indistinguishably-tuned glomeruli. Our results do not suggest that tight glomerular apposition cannot exist between similarly-tuned VSN types, but rather that strong, reproducible juxtaposition does not require similar odorant tuning.

These observations comprise the first clear examples of functionally-defined AOB glomerular "modules", and demonstrate that the individual glomeruli in these modules can be tuned to odorants with very different molecular features. The apparent discrepancy between juxtaposition and receptive field similarity when evaluating urine-stimulated maps and steroid-stimulated maps

may indicate that the organizational principle in the AOB is based on phenotypic, and not molecular, similarity between odorants. This would perhaps indicate that only biologically-significant odorant combinations are selectively juxtaposed in the AOB. The computational benefits of juxtaposing these particular glomeruli remain to be elucidated. Are these adjacent signals integrated by downstream mitral cells or specifically inhibited by local interneurons? Does physically juxtaposing these inputs enable the AOB to identify specific hormonal or behavioral states? Answering these questions will certainly improve our understanding of the logic of this important social and reproductive sensory pathway.

3.5 Supplemental Figures

Figure 3.5.1

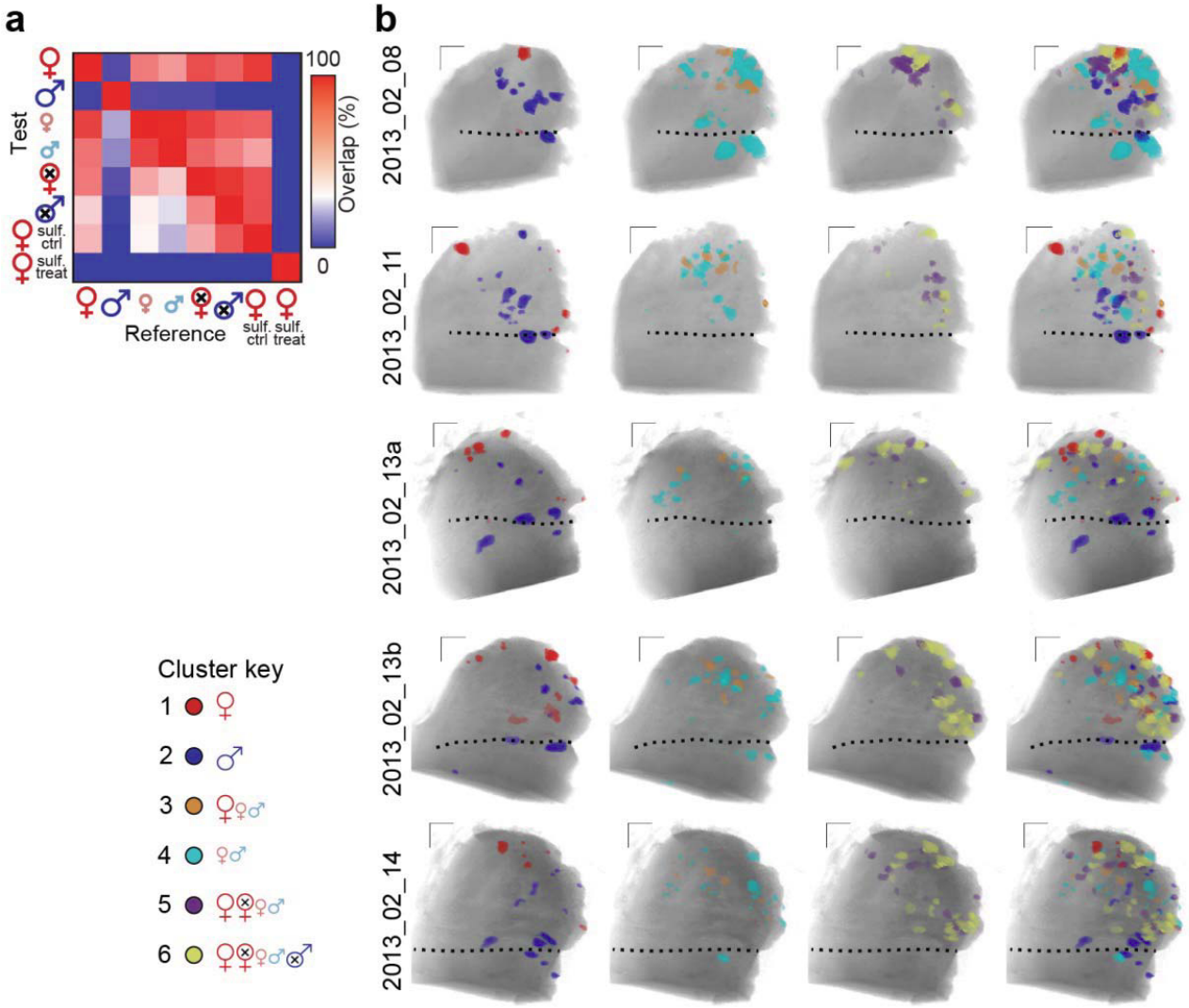

Figure 3.5.2

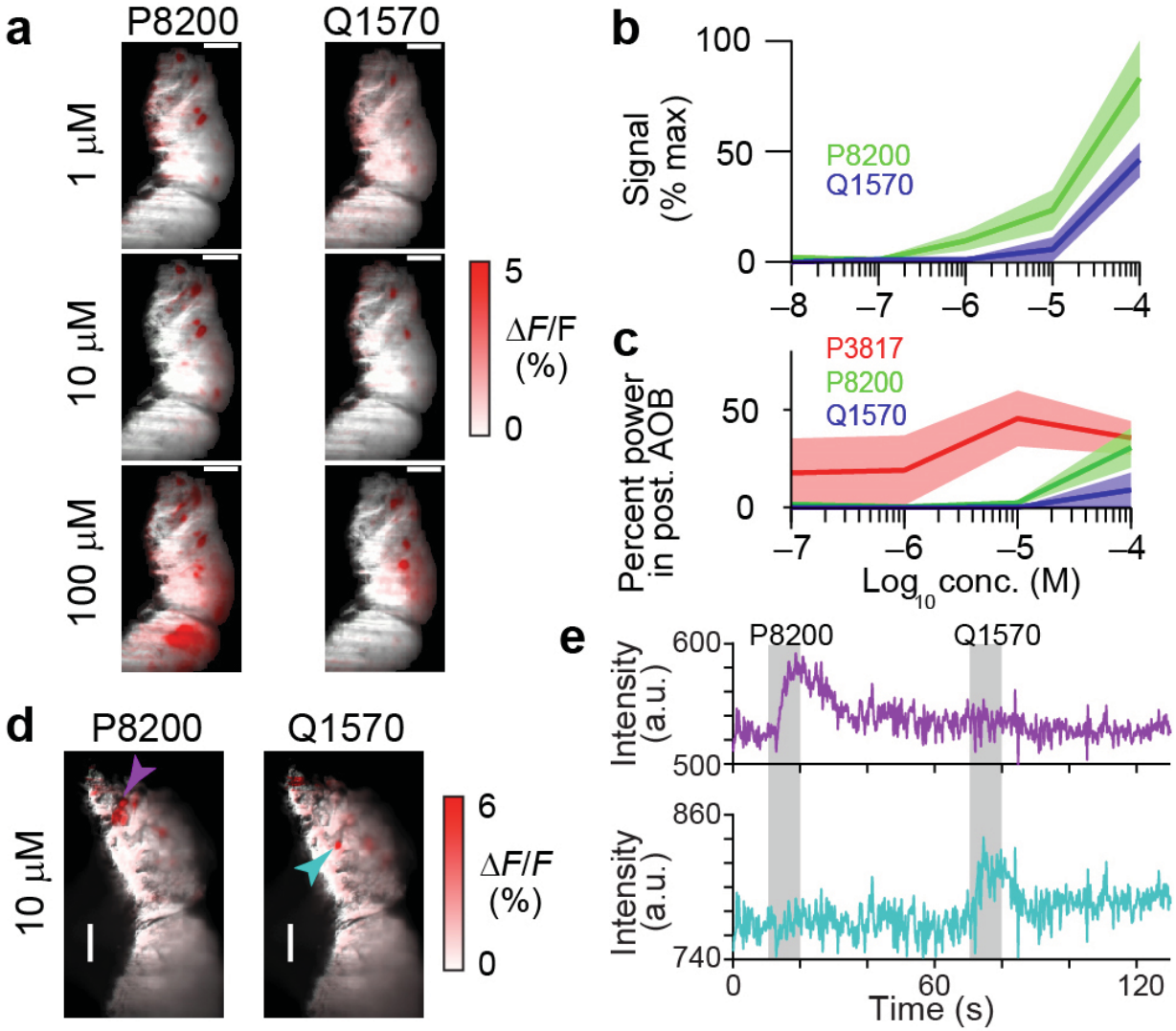
a
P8200
Q1570
1 μM
10 μM
100 μM
5
ΔF/F
(%)
0
b
100
50
0
Signal
(% max)
P8200
Q1570
–8
–7
–6
–5
–4
c
P3817
P8200
Q1570
50
0
Percent power
in post. AOB
–7
–6
–5
–4
Log10 conc. (M)
d
P8200
Q1570
10 μM
6
ΔF/F
(%)
0
e
P8200
Q1570
600
500
Intensity
(a.u.)
860
740
Intensity
(a.u.)
0
60
120
Time (s)

Figure 3.5.1: Response overlap and spatial distribution of urine-responsive glomeruli. (a) Pairwise comparison matrix for the overlapping ROI volume between all tested urine sources ($\Delta F/F$ 2%). Columns represent the reference groups and rows represent the test groups. Note: sulfatase-treated adult female urine (final row/column) activated extremely few glomeruli at this threshold. (b) Urine-selective glomerular maps for 5 experimental animals. Each glomerulus is colored using the strategy indicated in Figure 3f. The first column shows maps for clusters 1 and 2, the second 3 and 4, and the third 5 and 6. The smallest clusters, Clusters 7 and 8 are omitted from this figure. The right-most column shows clusters 1-6. Figure 3a displays experiment "2013_02_14", Figure 3g displays experiments "2013_02_13a" and "2013_02_14", and Figure 4 displays experiment "2013_02_13b". Dotted lines indicate the position of the *linea alba*. Scale bars: 100 μm.

Figure 3.5.2: Sulfated steroid glomerular activity across concentrations and at fast time scales. (a) Stimulation of the VNO with 1, 10, or 100 μM P8200 or Q1570 resulted in increased fluorescent intensity and number of active glomeruli. At 100 μM, the activity increased dramatically, making discrimination of individual glomeruli more difficult. Scale bars 100 μm. (b) Percentage of signal strength (sum of suprathreshold ΔF/F intensity, normalized per experiment) for each steroid across 5 log orders of concentration. Shaded areas represent mean ± standard error of the mean across multiple experiments (P8200, N = 4; Q1570, N = 2). (c) At higher steroid concentrations, the number of steroid-responsive glomeruli in the pAOB increased for all steroids. Posterior AOB glomeruli responsive to sulfated pregnanolone P3817 were evident at lower concentrations. (d) Average change in fluorescence during stimulation during continuous 10 Hz imaging of a single frame. Colored arrowheads indicate the location of two glomeruli analyzed in e. Scale bars 100 μm. (e) Intensity changes in glomeruli indicated by the colored arrowheads in d. Stimuli were delivered for 10 s (gray regions).

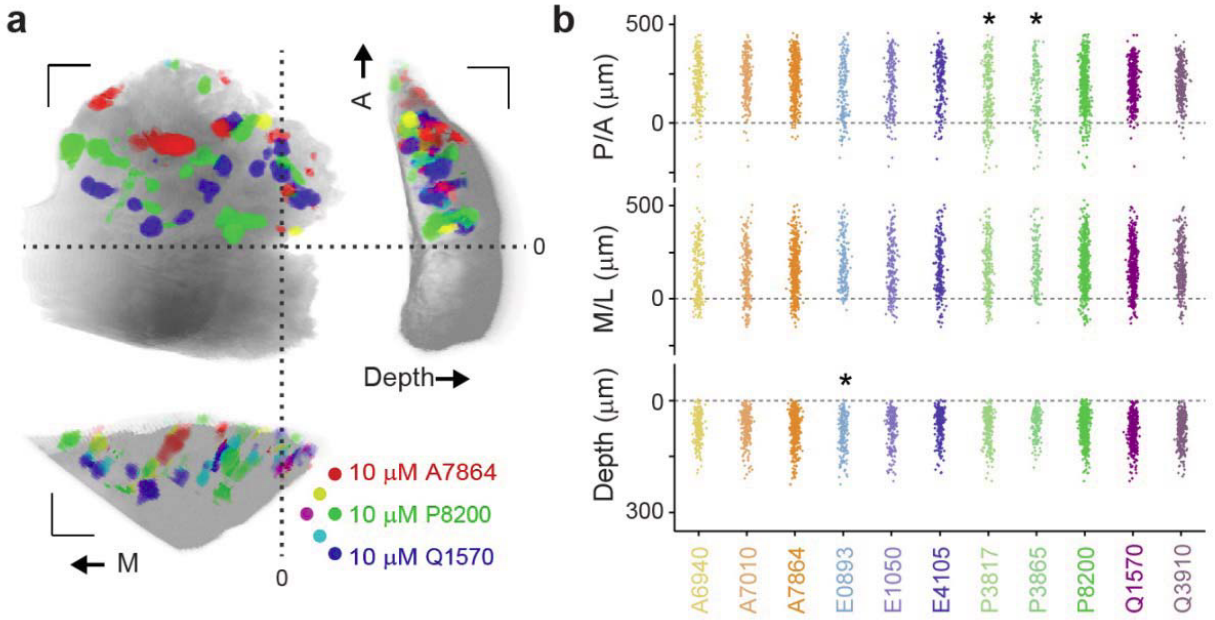

Figure 3.5.3: Absolute positions of sulfated steroid-responsive ROIs and pAOB responses to sulfated pregnanolones.
(a) Orthogonal plot of views of the AOB as visualized from the surface (top-left), posterior (bottom) and lateral (right) viewpoints. The color of the glomeruli reflects their responsivities (threshold ΔF/F > 1%). Yellow, magenta, and cyan regions indicate glomeruli responding to more than one steroid at this threshold. (b) Aggregated position information for all 1078 steroid-responsive ROIs along each of the 3 orthogonal coordinates at ΔF/F > 1% (n = 10). The dotted line along the medial/lateral (M/L) and posterior/anterior (P/A) axes refers to their position relative to the landmarks indicated by dotted lines in a. Depth was measured relative to the actual tissue surface. Asterisks denote populations which were statistically different than the majority of the other populations ($p < 0.05$, one-way ANOVA).

Figure 3.5.4

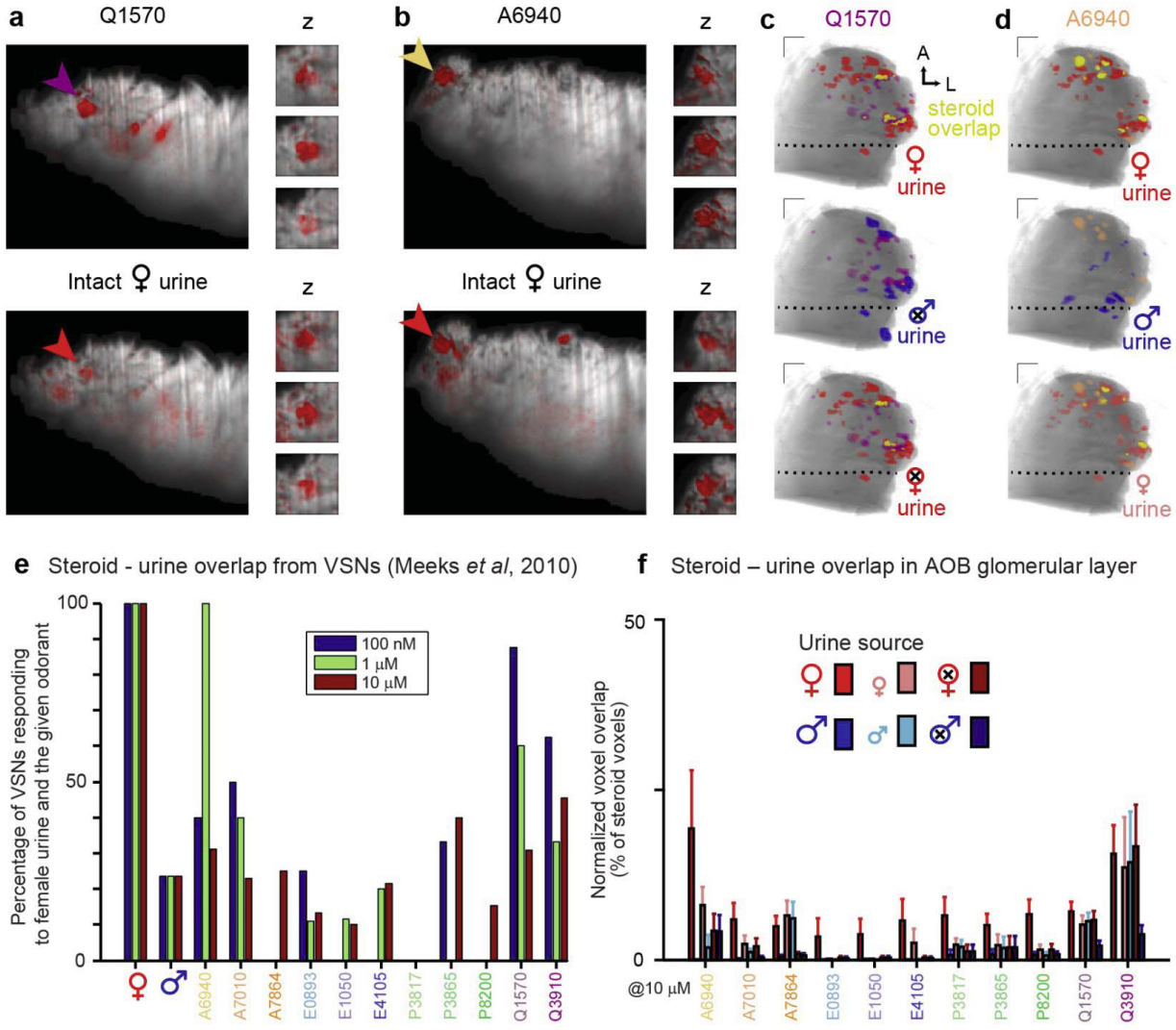
a
Q1570
z
b
A6940
z
Intact ♀ urine
Intact ♀ urine
c
Q1570
d
A6940
A
L
steroid
overlap
urine
urine
urine
urine
urine
urine
e Steroid - urine overlap from VSNs (Meeks et al, 2010)
Percentage of VSNs responding to female urine and the given odorant
100
50
0
100 nM
1 µM
10 µM
♀
♂
A6940
A7010
A7864
E0893
E1050
E4105
P3817
P3865
P8200
Q1570
Q3910
f Steroid – urine overlap in AOB glomerular layer
Normalized voxel overlap (% of steroid voxels)
50
0
Urine source
@10 µM
A6940
A7010
A7864
E0893
E1050
E4105
P3817
P3865
P8200
Q1570
Q3910

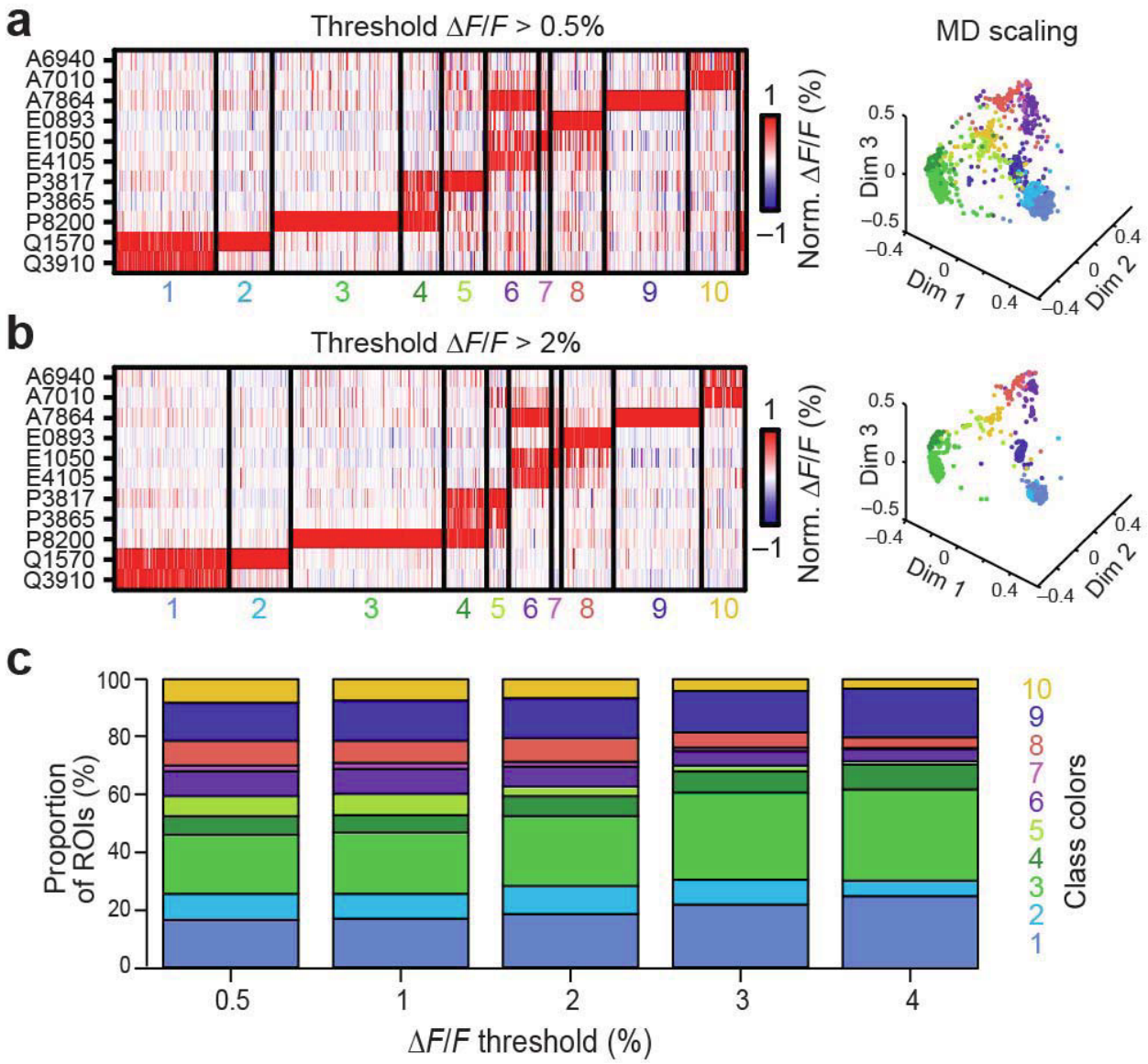

Figure 3.5.5: ROI functional clusters across threshold.
(a-b) Plots of the normalized ΔF/F for all ROIs across all experiments (N = 10). Each colorized column represents 1 ROI. The order of the ROIs within each cluster grouping (delineated by vertical black bars) was randomized. Insets to the right of each plot show the first 3 multidimensional scaling dimensions from independent clustering runs. The color of each point matches the VSN class color values in c. (c) Proportion of total ROIs in each cluster across all thresholds tested. Colorized list at right indicates the color assigned to each VSN class.

Figure 3.5.4: VSN co-activation by sulfated steroids and intact BALB/c female urine. (a-b) Several aAOB glomeruli were co-activated by 1:100 intact adult BALB/c female urine (bottom, red arrowheads) and 10 μM Q1570 (purple arrowhead, a) or 10 μM epitestosterone sulfate (A6940, yellow arrowhead, b). Right insets in a and b show single responses of the indicated glomeruli across 3 consecutive frames of the stack at higher zoom (image size 35 μm square). (c-d) Rendered maps of glomerular ROIs responding to 10 μM Q1570 (c, purple) or A6940 (d, orange). Steroid- responsive maps are overlaid on glomerular ROIs responsive to 1:100 dilutions of the indicated urines ($\Delta F/F > 2\%$) with overlapping voxels labeled yellow. All scale bars 100 μm. A: anterior, L: lateral. (e) The number of VSNs responding to sulfated steroids and 1:100 BALB/c female urine as measured on multielectrode arrays ($p < 0.05$ Wilcoxon rank-sum test, firing rate change > 1 Hz compared to controls; Meeks *et al*, 2010). These estimates are normalized to the total number of neurons responsive to the steroid at each concentration or 1:100 urine (left-most plots). Note the concentration- dependent decrease in the percentage of co-responsive neurons for Q1570. Because nearly all 100 nM Q1570- responsive VSNs also respond to BALB/c female-urine, this would be consistent with an endogenous concentration of Q1570 in BALB/c female urine of 1 to 10 μM (100 x [10 to 100 nM]), consistent with estimates from Nodari *et al*, 2008. (f) The percentage of steroid-responsive voxels that overlapped urine-responsive voxels ($N = 7$ for intact adult urines, $N = 4$ for all others). (f) Normalized voxel overlap between steroid-responsive glomeruli and mouse urine across sex and sexual maturity. Error bars reflect s.e.m.

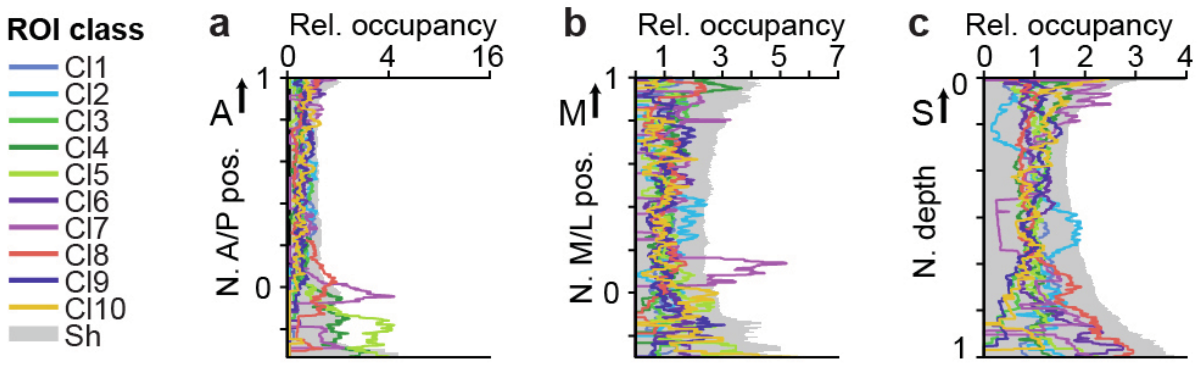

Figure 3.5.6: Absolute positions of steroid-responsive glomerular classes.
(a-c) Plots of ROI relative occupancy by steroid-responsive glomerular class (n = 10, cluster definitions shown in Fig. 6b). The observed relative occupancy of glomeruli of each class (solid colored lines) was compared to the 95th percentile (gray shaded region) from shuffled maps (100,000 shuffle tests per experiment, n = 10 experiments). Lines exceeding the shaded regions indicate preferential occupancy of particular positions by glomeruli of that class.

Chapter 4

Hierarchical modulation of neural olfactory maps: within region, between region, and between odor interactions.

4.1 Abstract

Sensory processing requires integration of multiple streams of information. In the mammalian olfactory systems, integration is thought to begin in the olfactory bulb, but the contributions at different stages of bulbar processing are a matter of active investigation. Here we show that in the mouse accessory olfactory bulb (AOB), substantial integration begins presynaptically in the axon terminals of the sensory neurons. Using mice expressing GCaMP2 in vomeronasal sensory neurons, we imaged whole-AOB glomerular responses to delivery of both natural stimuli and synthetic compounds. Comparing responses to single stimuli and binary mixtures, under both control conditions and blockade of feedback, revealed the existence of strong lateral inhibition between different processing streams.Locally, interactions among glomeruli were often asymmetric and occasionally

nearly unidirectional. Some processing streams were separately subject to odorant-chemorecepter interactions occurring in the nose. On the scale of the whole bulb, pairwise interactions were diverse, with similar glomerular "modules" exhibiting distinct patterns of inhibitory interactions in different regions of the AOB. Consequently, the divergent projections of vomeronasal sensory neurons contributes to a diversity of presynaptic integration.

4.2 Introduction

Presynaptic inhibition of olfactory sensory neurons is a well documented phenomenon. In the *drosophila* antennal lobe, an interconnected network of excitatory and inhibitory interneurons gives rise to an effective global inhibition that serves to normalize activity across the circuit[73]. This inhibitory paradigm, termed divisive normalization [17, 40], is observed in the context of a broad variety of interneurons which could theoretically allow for other modulatory paradigms as well [19].

In the mammalian olfactory bulb, there is ample substrate for mediating lateral interactions at multiple levels [55]. A well described form of postsynaptic inhibition via reciprocal dendrodendritic synapses of mitral cell projection neurons with granule cell interneurons plays a distinct role in decorrelating mitral cell responses [75, 47, 2], perhaps incorporating feedback from other regions of the brain [55]. Within the glomerular layer the short axon cells (SAs) and periglomerular cells (PGs) are predominantly driven by excitatory external tufted cells (ETs), which themselves are driven directly by olfactory neurons (ONs) [38, 85, 52]. These SAs reportedly interconnect up to a dozen glomeruli at a time [52], and, in concert with the ETs can drive lateral inhibition onto some postsynaptic targets within the glomerular layer [106].

Within the main olfactory system, the presence of inhibitory $GABA_B$feedback on the ON presynaptic terminals has been well established [107, 5, 103]. One series of optical recordings from mice, utilizing both *in vitro* glomerular layer slices and *in vivo* anesthetized animals, in which the ONs expressed the fluorescent reporter synpatophluorin reported ionotropic glutamate

mediated $GABA_B$ dependent presynaptic inhibition [104]. Similar experiments performed at nearly the same time explicitly addressed intraglomerular verses interglomerular inhibition but concluded that interglomerular inhibition plays "little or no role" [60]. However, subsequent *in vivo* experiments using olfactory epithelium loaded high affinity calcium dyes found striking evidence for interglomerular inhibition [102], as well as pointing out conflicting data in the previous publication [60]. Subsequent *in vivo* detected separate tonic and activity-dependent presynaptic inhibition, but could not detect presynaptic lateral inhibition [76].

In the mammalian accessory olfactory system (AOS), no such controversy yet exists, and the question of whether there is a role for presynaptic modulation seems particularly important in a system with strong spatial organization between chemosensory representations.

The mammalian AOS extracts and organizes information about species, sex, and individual identity from social odors. Metabolites, such as those from steroid hormones, are know to be prominent cues detected by the system. Sensory responses to both natural and synthetic ligands are spatial organized into an apparently modular map, but the implications of this organization for the neural representation of complex ethological stimuli and mixtures remains to be explored.

The vomeronasal sensory neurons (VSNs) of the AOS detect chemical cues through two families of about 300 receptors. The responses of neurons expressing the same receptor type—and thus having identical responses to chemical stimuli—converge within a small but variable number of neuropil regions, called glomeruli, within the accessory olfactory bulb (AOB). Within glomeruli, presynaptic vomeronasal sensory neuron (VSN) axons release glutamate, driving activity in postsynaptic neurons. On the postsynaptic side, glomeruli are innervated by the principal output neurons of the AOB, the mitral/tufted cells, as well as multiple types of juxtaglomerular neurons [55]. Like their analogs in the main olfactory bulb (MOB), some of these juxtaglomerular neurons are suspected to feed back onto the presynaptic VSN terminals. Consequently, as observed in the MOB there is an anatomical substrate for modulation of presynaptic inputs, but to our knowledge no study has yet examined this question functionally [107, 75, 55].

The AOB possesses a number of favorable properties enabling a detailed investigation of the

nature of presynaptic glomerular interaction. First, its compact size and location on one face of the bulb means that virtually the entire AOB glomerular layer can be imaged in a single field of view [36]. This feature implies that interactions are exhaustively observable, without concern that responses might be modulated by glomeruli that reside on a different face of the bulb. Moreover, individual VSN receptor types target multiple (3–20) glomeruli within the AOB [9], providing a built-in control within a single bulb to test the reproducibility of any candidate "rules" for presynaptic interactions.

Although using mixtures in addition to single component stimuli may evoke deviations from simple response additivity, the ability to pharmacologically block circuit feedback makes this advantageous. In addition to the local neural circuit, mixture components interactions with vomeronasal receptors (VRs) are poised to shape the form of chemosensory information entering into the bulb. In a given odor representation, the component parts could interact at the receptor level or generate feedback onto the presynaptic terminals at map level. Imaging at the presynaptic glomeruli provides access to both of those effects.

Our observations demonstrate that, in contrast to some expectations from the MOB [60], glomeruli in the AOB interact with both self- and lateral inhibition. Locally, one glomerulus may be relatively unaffected by activity in its neighbors, yet provide powerful inhibition onto one or more of its neighbors. Consequently, these interactions are not reciprocal. By classifying glomeruli into types based on their functional responses[36], we then asked whether the interactions among glomeruli follow rules specific to particular glomerular types. We found that certain types are subject primarily to self-inhibition, whereas others are characteristically inhibited by specific other types. However, within the ability of functional classification to resolve types, we also found that interactions are frequently idiosyncratic: in particular, among multiple "modules" in a single AOB containing the same handful of types, interglomerular interactions exhibited significant variation from one module to the next. Consequently, the existence of multiple modules provides an opportunity for diversity in local sensory processing.

4.3 Results

As described in the Chapter 2.2 (Methods), we utilized a semi-intact experimental preparation that preserves connections between peripheral VSNs in the vomeronasal organ (VNO) and the AOB. Importantly, this preparation (see 4.3.1) allows discrete delivery of the sulfated steroids as well as separate superfusion of the AOB circuit (with or without pharmacological agents). In a short series of experiments we pursued between stimulus effects in VNO using a preparation of the neuroepithelium (also detailed in Chapter 2.2).

Figure 4.3.1

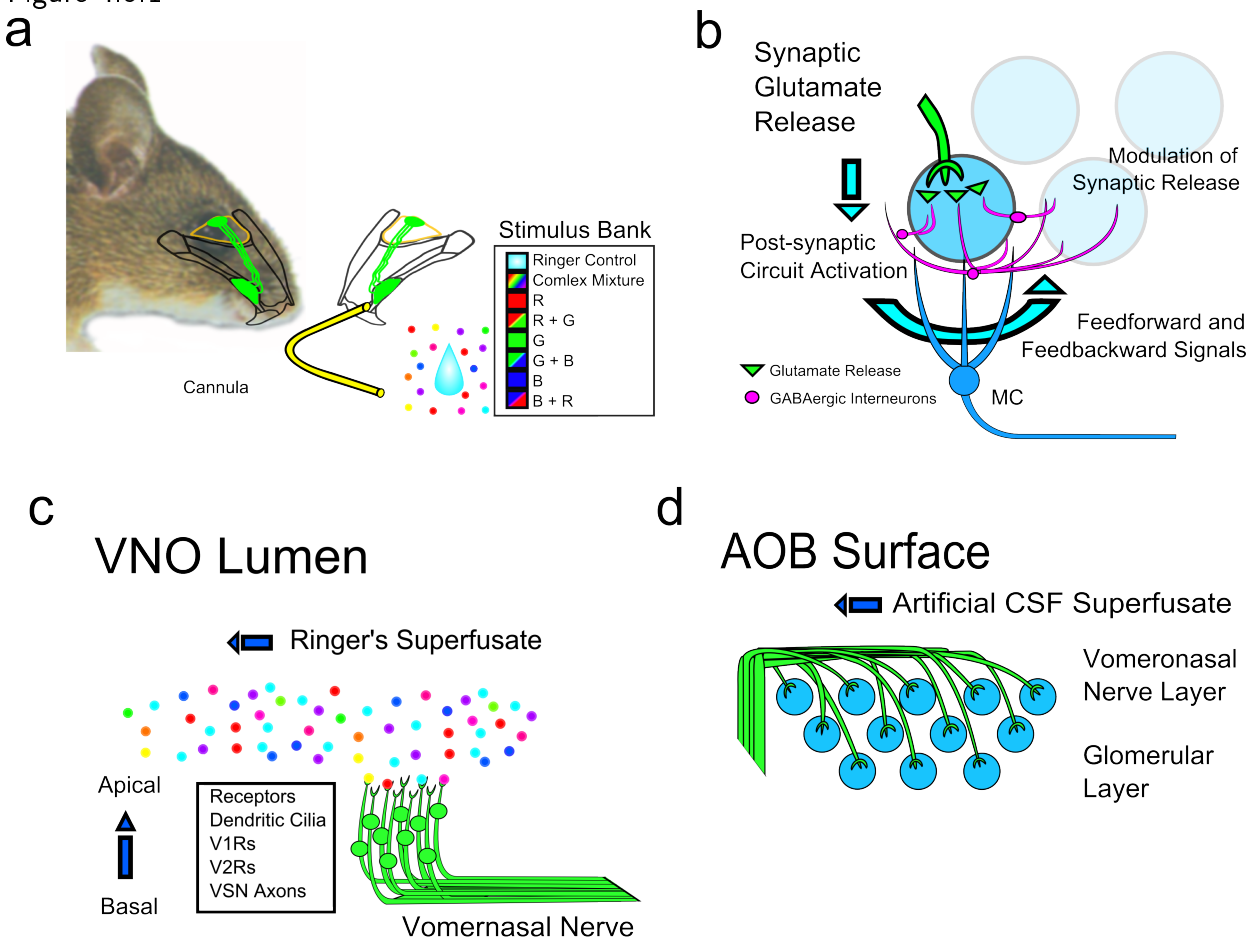
a
Cannula
Stimulus Bank
Ringer Control
Comlex Mixture
R
R + G
G
G + B
B
B + R
b
Synaptic
Glutamate
Release
Modulation of
Synaptic Release
Post-synaptic
Circuit Activation
Feedforward and
Feedbackward Signals
Glutamate Release
GABAergic Interneurons
MC
c
VNO Lumen
Ringer's Superfusate
Apical
Basal
Receptors
Dendritic Cilia
V1Rs
V2Rs
VSN Axons
Vomernasal Nerve
d
AOB Surface
Artificial CSF Superfusate
Vomeronasal
Nerve Layer
Glomerular
Layer

Figure 4.3.1: A hierarchical series of processes may be observed at VSN axon terminal glomeruli. Calcium fluorescence recordings from accessory olfactory bulb (AOB) vomeronasal sensory neuron (VSN) axon terminals allows observation of the signals from multiple processes: ligand-chemoreceptor interactions, the glomerular organization from converging vomeronasal sensory neurons expressing the same receptor type, and potential circuit mediated feedback.
(a) Graphic model of the mouse and the, hemi-head AOB experiment preparation which includes the peripheral accessory olfactory sensory neurons VSNs), nerves of the midline nasal cartilage epithelium, and the olfactory bulb. A small 0.005 inch polyimide cannula delivers a saline Ringer's solution and stimuli, here color coded by "type": aqua saline control, color, or color gradient . Transgenic GCaMP(2) expression is indicated as green.
(b) At the presynaptic terminal of the primary sensory neuron afferent, observed calcium fluorescence changes (a surrogate for presynaptic calcium-mediated vesicle release, green) could represent at least 3 processes: interactions between stimuli and chemoreceptors at the previous stage; process or glomerulus specific local feedback; and lateral feedback (whether directed or undirected).
(c) Graphic model of a green GCaMP expressing vomeronasal neuroepithelium and a "complex" stimulus mixture represented as colored dots, some interacting with receptors on the chemoreceptors on VSN cilia. VSN receptor-type expression varies apical to basal, and via the vomeronasal nerve V1R VSNs project to the anterior AOB (aAOB) and V2R VSNs project to the posterios AOB (pAOB).
d). Graphic model of the AOB glomerular layer cross-section with converging inputs from the nerve layer, represented as a single green axon and terminal, of the same receptor type to a region of neuropil, represented in blue.

Receptor tuning profiles, glomeruli, and relative location are defining features in the neural representation of the components of complex chemosensory information.

We utilized both single compounds and mixtures of three steroids (Figure 4.3.3a) to identify previously reported types of glomeruli (Chapter 3, also [36]) known to occur both inside of and outside of known module type and evoked responses in different combinations of those glomeruli. Although many glomerular regions could be activated by these three stimuli (Fig 4.3.3), we focus on five basic distinguishable classes relevant to our hypotheses.

As demonstrated by rendering different views of ROIs across the AOB, we can see that the anterior/posterior division separates responsive glomeruli (Figure 4.3.2). This allows us to focus primarily on four types of anterior AOB glomeruli. The P2 selective glomeruli in the aAOB occur both in and out of modules (labeled throughout in green, see Figure 4.3.3e for example responses and timecourses). Notably in the aAOB all-pregnanolone, both P1 and P2 responsive,

glomeruli are always spatially associated with a subtype of E1 selective ROI (Figure 4.3.3c-g for spatial maps and timecourses). In contrast to the all pregnanolone type, P1 selective and P2 selective ROIs were reported to be spaced particularly far apart, and neither as a group associated specifically with the all pregnanolone or E1-responsive (see Figure 4.3.3d-e) . These types of glomeruli are consistent with our prior mapping work in the aAOB, as defined in Chapter 3, [36]), and raster plots showing the proportion of glomeruli responding to each of these steroids and their combinations is presented in Figure 4.3.3b and a by-response plotting of ROIs from an example data set in Figure 4.3.3c-g.

In the pAOB there are several types of sulfated steroid responsive glomeruli which we categorized in a similar fashion. These pAOB ROIs are reported in the same color coding as the aAOB, but are separated to the right in heat maps of population responses by group (see Figure 4.3.3b) Those glomeruli that were present in the posterior AOB (pAOB) were likely a V2R expressing populations, while the others in anterior AOB (aAOB) and were assumed to be from the more numerous V1R expressing VSNs ([9]). The pAOB contained separate groups of glomeruli, of which some respond exclusively to P1 and others preferentially to P1 over P2, and we have previously described these consistent but lower affinity responses to P2 (from 10-100 μM). These pAOB glomeruli differ markedly from those in the aAOB: most P2 selective aAOB glomeruli were high affinity responders (as reported in a concentration series in Chapter 3, [36]). Due to the high affinity responses we previously reported, we utilized lower concentrations (1 μM) in the present study to elicit aAOB P2 responses. This pAOB populations were easily segmented anatomically in our data sets by using both anatomical and surface features to define an 3-dimensional coordinate system with an anterior/posterior plane (Figure 4.3.2e).

Figure 4.3.2

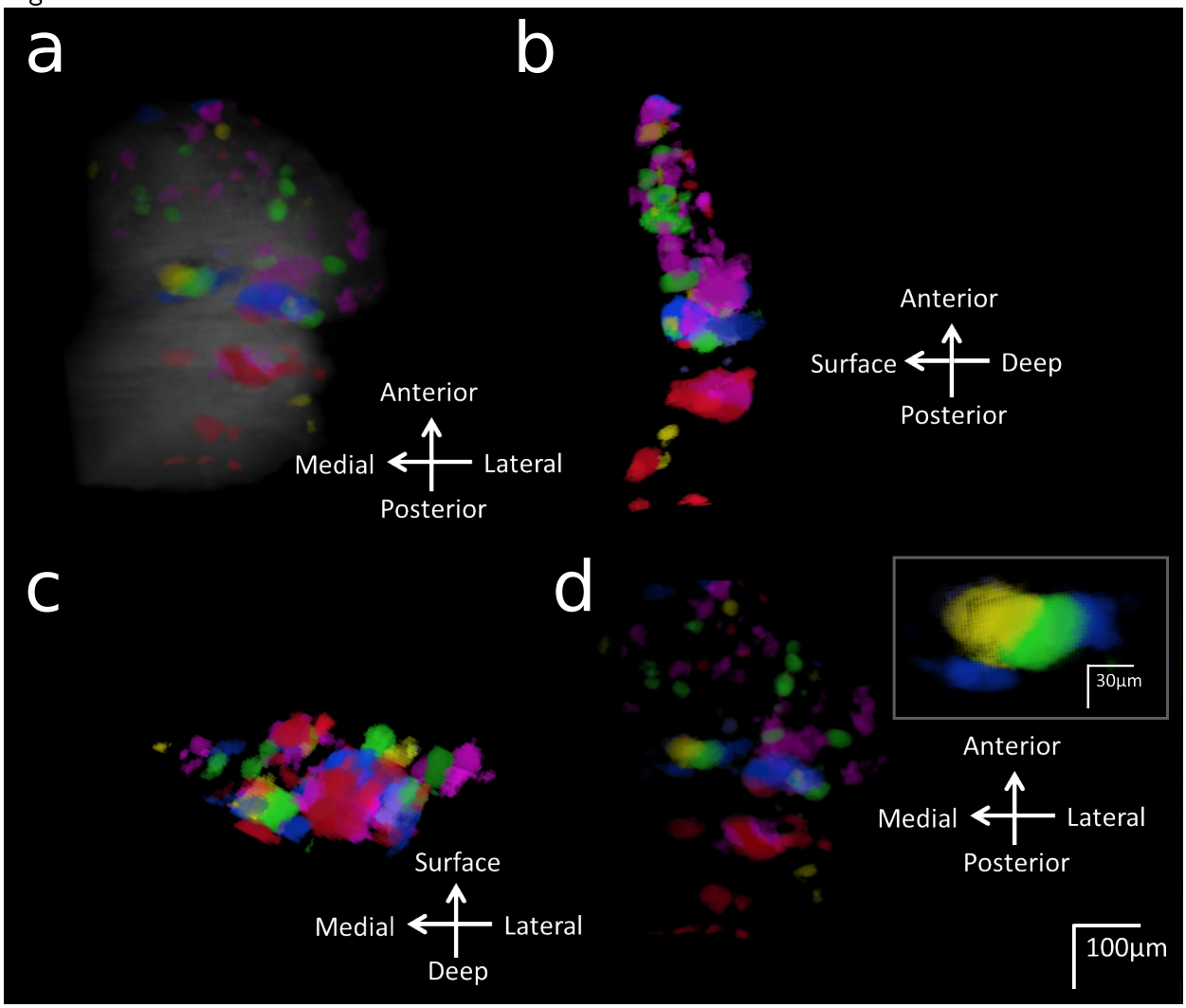
a
Anterior
Medial
Lateral
Posterior
b
Anterior
Surface
Deep
Posterior
c
Surface
Medial
Lateral
Deep
d
30µm
Anterior
Medial
Lateral
Posterior
100µm

Figure 4.3.2: Orthogonal projections of ROIs in an anatomical coordinate system show both anterior posterior divisions as well as spatial associations.
(a) The spatial relationships between E1 selective and all-pregnanolone responsive regions is visible by rendering ROIs with color coding the response patterns and noting anterior/posterior localization: E1 selective blue; P1 selective red; P2 selective green; all pregnanolone responsive yellow; and others in purple. Scale bar is 100 μm and projection directions are relative to the defined 3D coordinate system.
(b) Using surface based coordinates to generate a lateral to medial projection view without grayscale makes the spacing between anterior and posterior AOB (aAOB and pAOB) regions prominent. The lateral most estradiol/pregnanolone module is particularly visible along the a/p divide.
(c) The posterior to anterior projection (PA) view without grayscale surround highlights some depth differences between aAOB P1 selective glomeruli and aAOB P2 selective glomeruli that are obscured in the lateral to medial projection. PA projection also makes the deeper, selected module appreciable; it appears framed in lower left corner by red and magenta posterior AOB (pAOB) regions in the foreground and several green aAOB P2 selective regions.
(d) The surface projection (a) without grayscale further clarifies the location of some smaller ROIs such as the aAOB P1 selective group. As an inset: one deeper module is rendered at higher resolution for better identification within different projections and later optical slices.

As hypothesized, there were interactions visualized in the glomerular maps when mixtures of specific types of odorants, or steroids, were presented. For example, a smaller group of ROIs selective for the P1 only responded strongly to P1 when E1 was not present (see Figure 4.3.3b(group 3),d). In other words, the P1 selective component of the glomerular responses was markedly suppressed in the context of E1 presentation. These P1 selective glomeruli, as a population, were not specifically near any other evoked activity, but this was not a global phenomenon as there was still a component of P1 evoked activity in pAOB as well as other components of the mixture response in the aAOB (see the raster for E1+P1, Figure 4.3.3b).

Figure 4.3.3

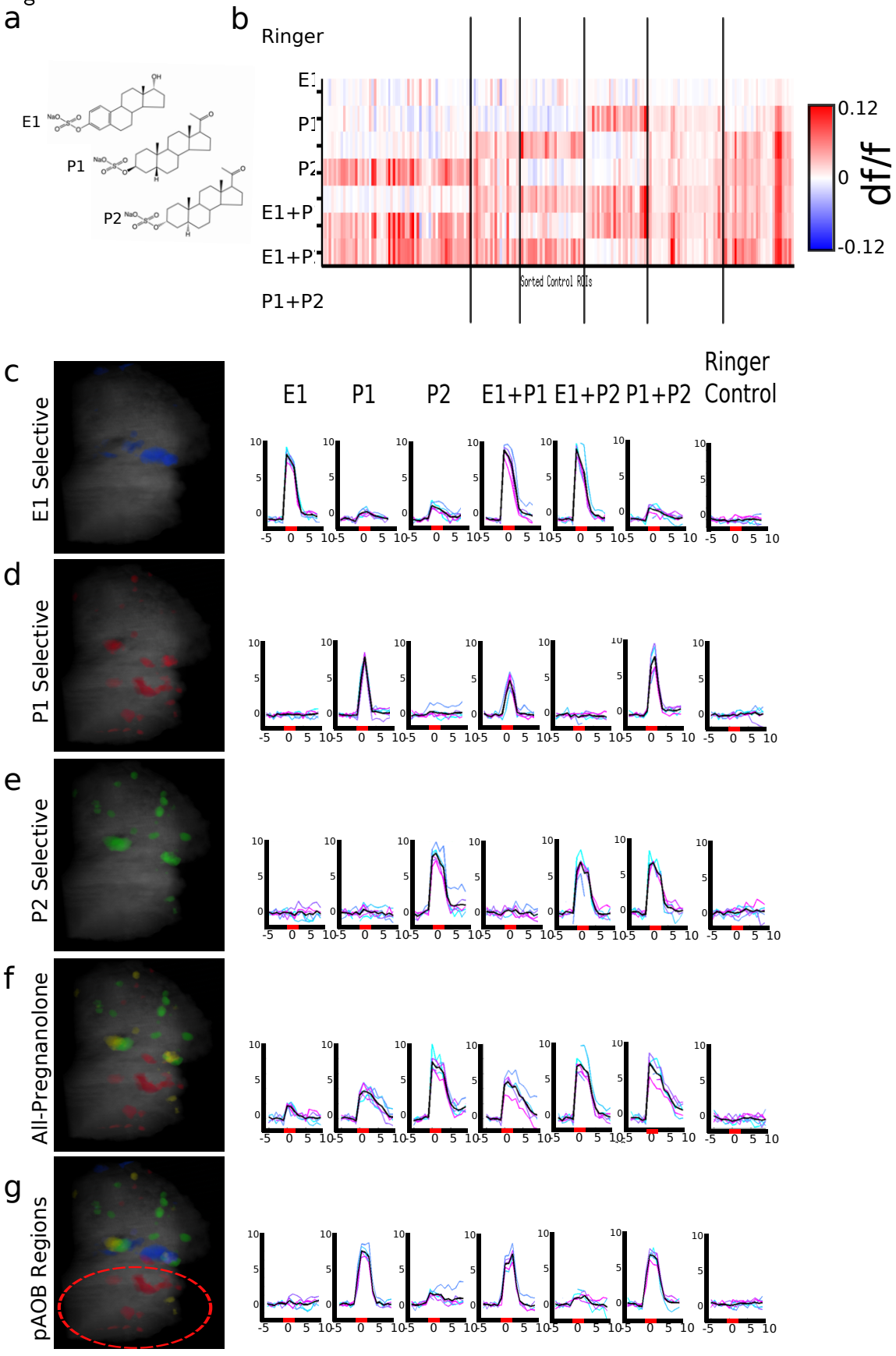
a
E1
P1
P2
b
Ringer
E1
P1
P2
E1+P
E1+P
P1+P2
Sorted Control ROIs
0.12
0
-0.12
df/f
c
E1 Selective
d
P1 Selective
e
P2 Selective
f
All-Pregnanolone
g
pAOB Regions
E1
P1
P2
E1+P1
E1+P2
P1+P2
Ringer Control

Figure 4.3.3: Regions are defined by evoked responses to odorants and anatomic location.
a) Three sulfated steroids were delivered, alone or in binary combinations, diluted in a Ringer's solution: E1 estradiol-17β 3-sulfate, P1 allopregnanolone 3-sulfate, and P2 epipregnanolone 3-sulfate, see Table 2.2.
g) Heat map or dF/F separated by pure stimulus response types and anatomical location, with aAOB(left) and pAOB(right).
c-g) Volumetric grayscale rendering in which the ROIs are labeled by their pattern of response specificity: blue E1 selective, red P1 selective, green P2 selective, and yellow All-Pregnanolone response. Regions in the aAOB and pAOB were presumed to be of different types, scale bar 100 μm, anterior/posterior. Timecourses (dF/F normalized) for stimuli and Ringer's control solution(s) trial repeats were aligned (color coded by order, cyan to magenta) to calculate the mean timecourses (black). Red circle indicates the pAOB

To further explore the attenuation of P1 response to the P1 component of odor mixtures by E1, we calculated the magnitude of this effect as a suppression index (SI). In one of the time/control animals, every P1 selective region has a reduced dF/F response to P1+E1 mixtures verses P1 alone. The response is not significantly changed in the P1+P2 mixtures, and this is reflected in the SI plots(4.3.4a-b). Across all animals, we visualized the decreased representation of the P1 component in the context of E1 by plotting the mean responses and the standard errors of responses to P1 on the abscissa and P1+E1 on the ordinate (no statistical measures were made on single glomerulus ROIs, coordinates related to SI by +1, see Methods 2.6).

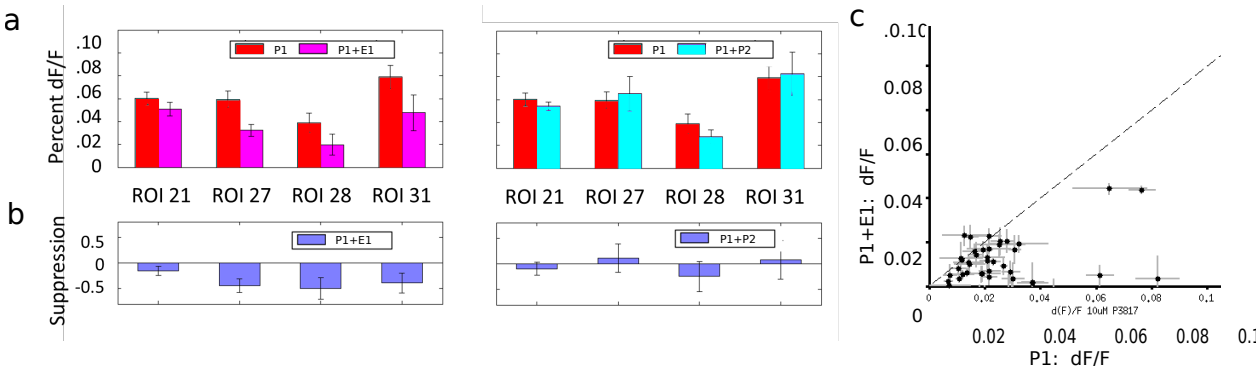

Figure 4.3.4: P1 responses in P1 selective regions were suppressed by co-presentation of P1 with E1.
P1 selective ROIs from one of the time/vehicle control experiments and all time/vehicle controls (n=3) are compared. a) Paired P1 selective ROI mean responses to each P1 and a mixture with E1 or P2, error bars are standard errors .
b) The SI index for each P1 mixture pair, matched by ROI and mixture.
c) Mean response and standard error for all P1 selective time/vehicle control animals as scatter plot indicating suppression as a point below the diagonal equivalence line of $y = x$. The coordinates of P1, abscissa, and E1+P2, ordinate, are equivalent to the SI+1, see Methods 2.6.

After encoding, signals represented in map regions were subjected to circuit mediated inhibition.

Given the strong suppression of P1 selective glomeruli, we wanted to block circuit mediated feedback in order to have access to both the raw, untempered inputs to the glomeruli before glutamate driven circuit mediated feedbacks.

We performed two sets of experiments each with two conditions: control experiments (n=3) with both a baseline and time/vehicle condition acquisition periods and ionotropic glutamate receptor blockade (iGluR) with both baseline and iGluR acquisition periods. When we observed all groups of ROIs, and the maximum responses after glutamate blockade (see Figure 4.3.5b-e) is quite different from that observed in control experiments after time/vehicle control (see Figure 4.3.5,d-e). With increasing time, in the control experiments preferred stimulus responses were largely maintained as indicated by scatter about the x/y diagonal (although with some possible decrement as deviation below the diagonal). However, in iGluR experiments the deviation above the diagonal was large, indicating a general increase in fluorescence with application of ionotropic

glutamate blockade.

For one of these iGluR experiments, the locations of ROIs and maximum mean responses in the baseline and blockade conditions are rendered (Figure 4.3.5b-c).This pattern of disinhibition was specific to the pharmacology and did not occur in the time/vehicle control experiments (Figure 4.3.3), as shown in the by-condition ROI responses to the preferred steroid stimuli (4.3.5j-k). Blockade of post-synaptic ionotropic glutamate receptor mediated circuit feedback unmasked significant inhibition at many glomeruli.

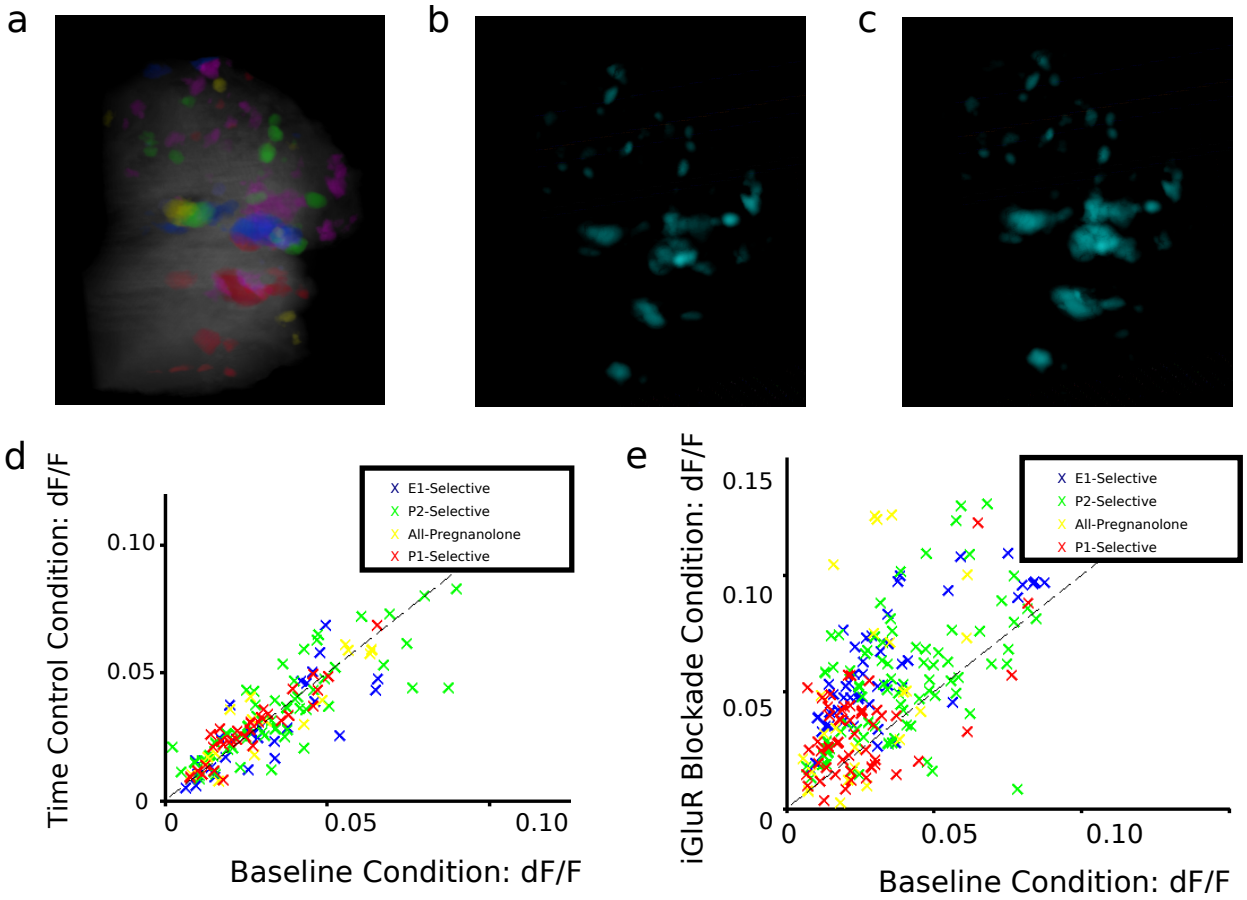

Figure 4.3.5: Glomerulus VSN axon terminal calcium responses are tempered by ionotropic glutamate feedback.
Ionotropic glutamate dependent modulation is measurable as the change in response after blockade of ionotropic glutamate receptorsThis visualization includes the anterior AOB and the approximately 2/3 of the adjacent posterior AOB.
(a) All regions, including, in purple, those that were not in our groups, with color assignments are shown for comparison to maximum responses.
(b-c) Rendered cyan intensity achieved by linearly increasing opacity with response.
(b) The maximum mean dF/F within all defined ROIs during the baseline condition of a glutamate blockade experiment.
(c) The maximum dF/F within all defined ROIs after ionotropic glutamate receptor antagonist washin.
(d) Scatter plot of ROI responses to preferred stimuli in baseline condition and after time/vehicle control (n=3 animals).
(e) Scatter plot of ROI responses to preferred stimuli after ionotropic glutamate blockade shows that there is a marked disinhibition of ROIs to their preferred stimulus (n=4 animals).

In the P1 selective regions, the effects of stimulus mixture and ionotropic glutamate receptor (iGluR) blockade were distinct, separate effects.

Given the previously demonstrated mixture suppression and effects of inhibition, we hypothesized that inhibition may be mediating the effects of mixture suppression. The presynaptic glomerular representation of P1 components of stimuli at P1 selective glomeruli was markedly suppressed by the presence of E1 in the mixtures (Figure 4.3.3). Examining the mean responses to all stimuli in a P1 selected ROI, we see that the mean response to most stimuli increases in magnitude after glutamate blockade (Figure 4.3.6b), but the P1 component was still suppressed by mixtures in this ROI and this ROI had no others in close proximity (lower right ROI in inset, Figure 4.3.6a). The mean population responses to individual stimuli and the mixtures (Figure 4.3.6d-e) shows an a qualitatively similar pattern, except with mixture suppression in both E1+P1 and P1+P2 mixtures is detectable at population level.

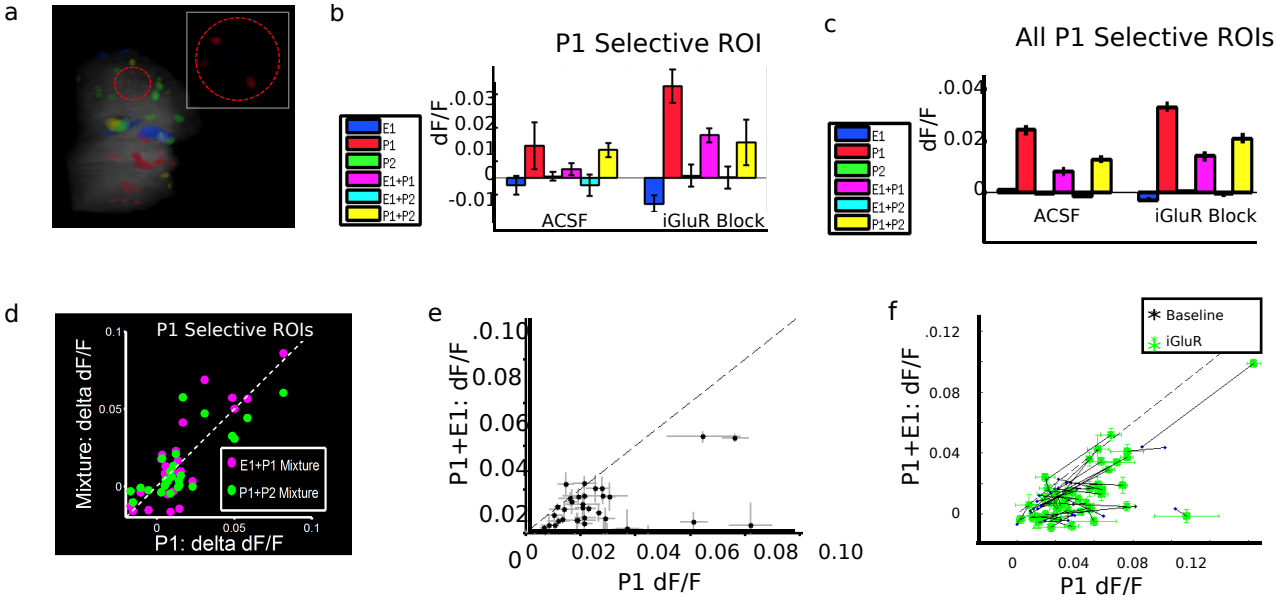

Figure 4.3.6: In the P1 selective glomeruli of the anterior AOB are unaffected by surround activity. Recruiting activity in either E1 or P2 selective glomeruli does not result in increased ionotropic glutamate dependent feedback on P1 selective glomeruli but does result in mixture suppression.
(a) In the rendered surface view of the data, the location of a selected set of the relatively isolated P1 selective anterior AOB (aAOB) glomeruli is highlight with a red dashed line and inset figure has the gray scale bulb removed.
(b) For one of the P1 selective regions, the lower right from inset (a), the receptive feild response profile to the pure stimuli are consistent in both aCSF and aCSF plus ionotropic glutamate receptor blockade. The largest change after iGluR is the response to the preferred stimulus alone and mixture suppression of the P1 component persists.
(c) The mean responses of all P1 selective ROIs from iGluR experiments exhibit residual suppression after ionotropic glutamate blockade (RM-ANOVA: between factors $p = 1.5e^{-13}$, η=0.68; effect of iGluR $p = 6.9e^{-4}$, η=.22; effect of stimulus $p = 4.5e^{-14}$, η=.47; iGluR x stimulus $p = 0.62$, η=.0098).
(d) The magnitude of the effect of inhibition on P1 selective ROIs mixture responses represented as the change in response, delta(dF/F), of the preferred stimulus P1 and two P1 mixtures (w/E1 magenta and w/P2 cyan).
(e) P1 selective ROIs (iGluR, control condition to P1, abscissa, E1 + P1, ordinate) responses indicating suppression as a point below the diagonal equivalence line of $y = x$. The coordinates are equivalent to the SI+1, see Methods 2.6.
(f) The relative change, after iGluR, in responses to P1 verses E1+P1 is represented as a line vector between the baseline cond (from (e),blue points) to glutate blocakde responses (green points), with error bars only after blockade. (errors bars were plotted in the previous panel for the starting points).

We then compared the suppression index (SI), a measure of the difference between the dF/F in the single stimulus presentation and in the mixture presentation, for the P1 selective ROIs before

and after ionotropic glutamate blockade (4.3.6e). For all P1 selective ROIs in these animals (n=4), we further visualize the change or trajectory in component responses after glutamate blockade by plotting a line vector between the baseline responses (blue points)and after glut ate blockade responses (green points), with error bars only at the blockade point for simplicity (errors bars for the starting points seen in Figure 4.3.6e). This plot demonstrates that while there is an increase in the response for each ROI with glutamate blockade, the response does not increase to the point that it crosses the diagonal line of equality, which would indicate that the mixture response becomes equal to the single stimulus response. To test for a statistically significant, systematic deviation from linear effect of glutamate blockade on stimulus we performed a repeated measure ANOVA but found the effects to be separable (RM-ANOVA: between factors $p = 1.5e^{-13}$, η=0.68; effect of iGluR $p = 6.9e^{-4}$, η=.22; effect of stimulus $p = 4.5e^{-14}$, η=.47; iGluR x stimulus $p = 0.62$, η=.0098).

Imaging of VNO neuroepithelium demonstrates suppression of odorant responses by mixture components.

To ascertain whether the observed independence of the mixture suppression and inhibition (control verses ionotropic glutamate blockade) was best explained by mixture ligand interactions with the receptor or some unaccounted circuit feedback phenomenon, we performed similar experiments using the same stimulus paradigm (but no pharmacology conditions) in the VNO neuroepithelium (see rendered image, 4.3.7a). We clustered stimulus responses sufficiently to separate out the same major groups observed in the aAOB (Figure 4.3.7b), however we could not fully separate the aAOB from pAOB types. We did identify a group of cells that were clearly P1 selective with many members showing E1 suppression(Figure 4.3.7b, two different animals), unfortunately we cannot definitively separate out the V2R expressing P1-responding that project to the pAOB from those projecting to the aAOB in the prior analysis.

Figure 4.3.7

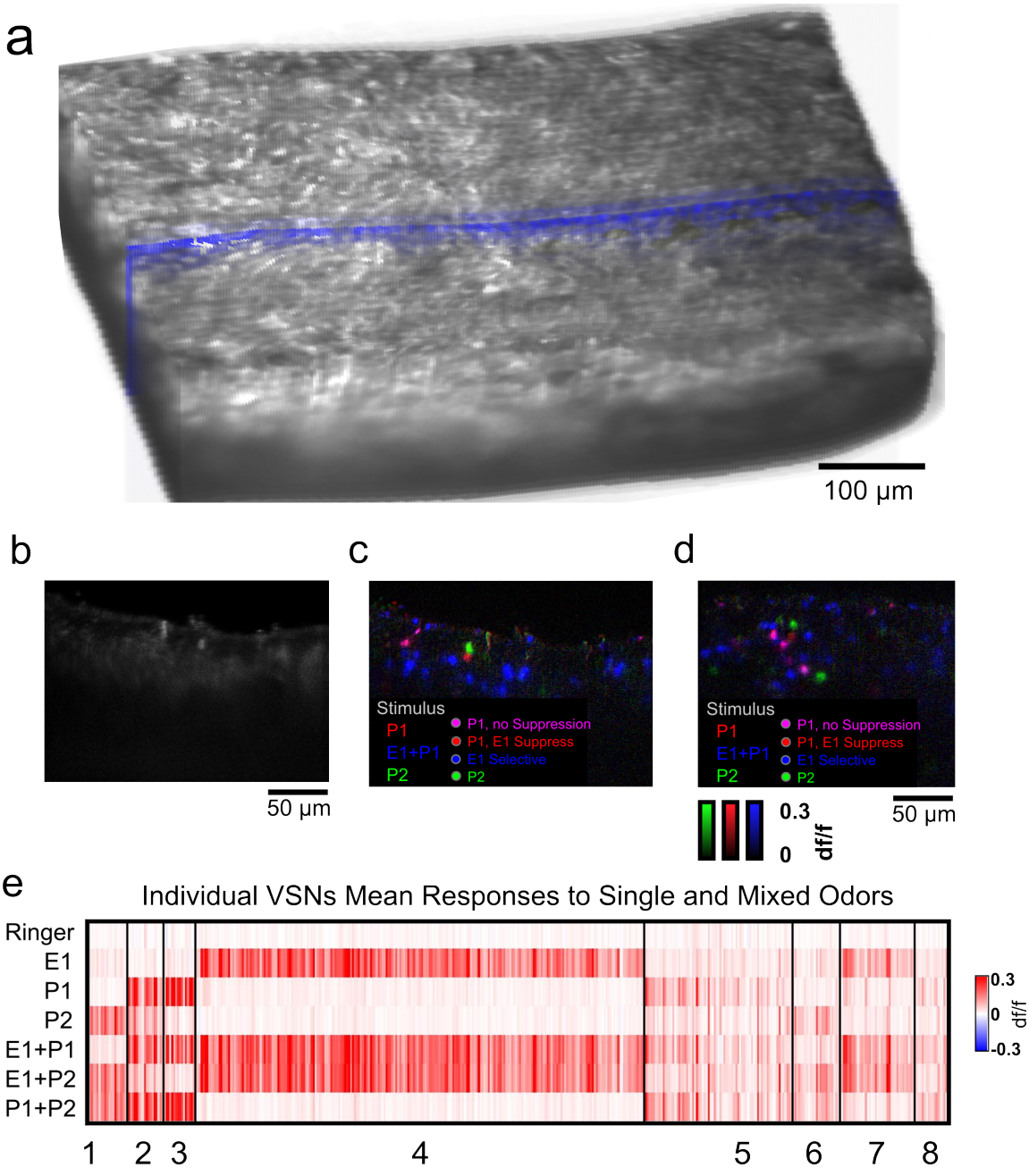
a
100 µm
b
50 µm
c
Stimulus
P1
E1+P1
P2
P1, no Suppression
P1, E1 Suppress
E1 Selective
P2
d
Stimulus
P1
E1+P1
P2
P1, no Suppression
P1, E1 Suppress
E1 Selective
P2
50 µm
0.3
0
df/f
e
Individual VSNs Mean Responses to Single and Mixed Odors
Ringer
E1
P1
P2
E1+P1
E1+P2
P1+P2
1 2 3 4 5 6 7 8
0.3
0
-0.3
df/f

Figure 4.3.7: A subset of P1 selective vomeronasal sensory neurons (VSNs) exhibit E1 mixture component suppression.
(a) 3D rendering of the isolated vomeronasal organ (VNO) neuroepithelium experiment preparation demonstrates GCaMP fluorescence throughout the VSNs acquired by volumetric scanning objective coupled planar illumination (OCPI): OCPI illumination illustrated as a single optical section colored blue.
(b) Grayscale optical section, representative of a 50 ms, matches the activity in (c).
(c-d) Two example optical sections from two VNO recordings. P1 selective cells do not responding to P2, and are magenta if responsive to the mixture and red if they not responsive to the mixture. Shown are the mean responses to 4 trials: P1 responses are colorized in red; E1+P1 mixture responses are colorized in blue; and P2 responses are colorized in green. Scale bar is 20 μm. Contrast limits are 0-12% dF/F.
(e) The total population of VSNs for which significant responses were recorded. Groups 5-8 represent weak responders that fell below confidence for linear classification and were clustered, see Methods 2.7. Contrast limits are 0-12% dF/F.

However, plotting the SI for all (apparently) P1 selective cells demonstrates a number of VSNs show the characteristic suppression pattern (Figure 4.3.8a:C). By contrast P2 selective cells and E1 selective cells show small stimulus component interactions and fall mostly along the x=y diagonal (Figure 4.3.8c:L,d:L), with the P2 selective have a small negative SI with P1, and the E1 selective cells appear to have modest supra-additive interactions. However the all pregnanolone cells suggest some suppression of P2 but not P1 responses in the context of co-presentation with E1.

Given the challenge in strictly assigning VR family identity, this may warrant further study but would also benefit from further characterization of pAOB ligands.

Figure 4.3.8

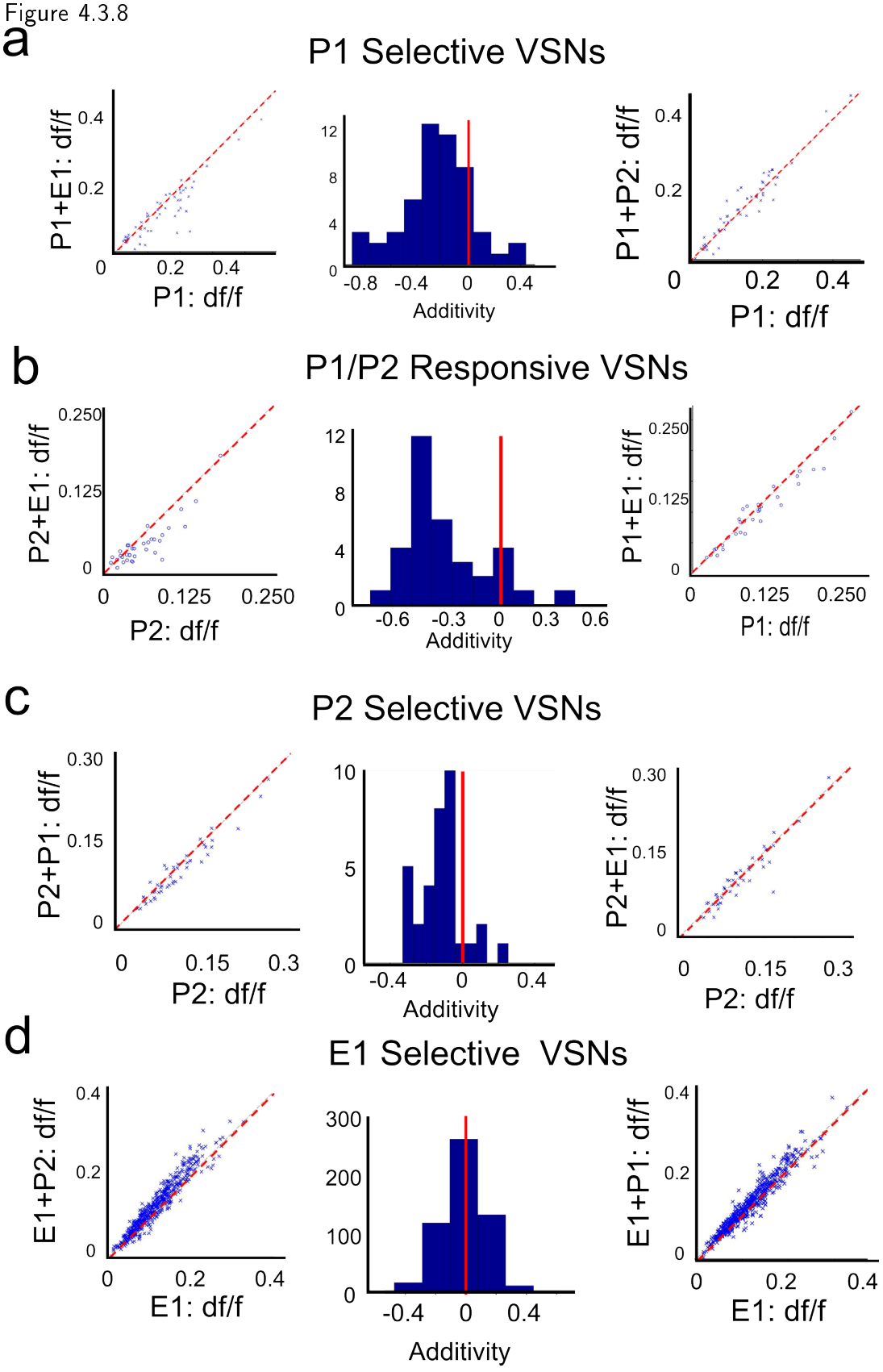
a
P1 Selective VSNs
P1+E1: df/f
P1: df/f
Additivity
P1+P2: df/f
P1: df/f
b
P1/P2 Responsive VSNs
P2+E1: df/f
P2: df/f
Additivity
P1+E1: df/f
P1: df/f
c
P2 Selective VSNs
P2+P1: df/f
P2: df/f
Additivity
P2+E1: df/f
P2: df/f
d
E1 Selective VSNs
E1+P2: df/f
E1: df/f
Additivity
E1+P1: df/f
E1: df/f

Figure 4.3.8: Peripheral VSN responses reflect potential antagonist/agonist mixture component interactions.
Standard suppression plots of preferred the preferred stimulus response, abscissa, and mixture response, ordinate are paired. For each group, the most linear mixture plot is to the right (R), and the mixture for which there was the greatest deviation from the diagonal equivalence line is left (L) of the central (C) additivity index (AI for all-pregnanolone or the special case, SI for others, see Methods Chapter 2.7) histogram: as additivity approaches zero, suppression is counted for by a negative response to the non-preferred odor alone.
(a) P1 selective cells, L: P1+E1 SI plot indicates that there is subset of P1 selective cells that have significant suppression by E1. C: Negative additivity suggests that E1 suppression effect is largely accounted for by the SI. R: P1+P2 SI has little deviation below the diagonal.
(b) All preganolone responsive cells, L:show a similar supression effect as the P1 population, E1 suppression of copresented P2 in a subset of cells, but (R) no effect on P1+E1. C: Bimodal additivity is congruent with at least two, anterior and posterior AOB, populations.
(c) P2 selective cells, R: P1+P2 mixture is suggestive of a small suppressive effect of P1 on P2 selective responses to P1+P2. L: E1 seems not to affect P2 selective E1+P2 responses, which along the diagonal equivalence line. C: Additivity near zero suggest that linear affects account for the modestly negative SI values.
(d) E1 selective: L/R both populations appear very but have a postive SI at higher values suggesting greater response to mixture than to E1 alone, but (C) additivity suggest a weak additive or agonist effect.

E1 selective module components were inhibited by surround activity.

Though the P1 selective glomeruli and VSN mixture suppression data does not support a role of interglomerular inhibition at glomerular level, our initial mixture analyses also demonstrated a mixture suppression effect for E1 selective glomeruli. This is particularly interesting, given that E1 selective glomeruli are almost always adjacent other glomeruli (Chapter 3, [36]). Thus after the previous test of P1 selective glomeruli detected circuit mediated feedback that was independent of the effects of mixture evoked activity, we focused on the E1 selective population that are associated with all pregnanolone responsive glomeruli. In order to better visualize the relative locations of these modules, the location of ROIs was rendered without grayscale background in Figure 4.3.2a-d. For ease of identification, the deepest module is also rendered as an example in larger size in Figure 4.3.2b and for comparing activity in Figure 4.3.9b.

In an optical section through this module, we compare the mean responses resulting from this single module in response to individual stimuli and mixtures (4.3.9). For the glomeruli in

the optical section of this module, the surface is located up out of the screen and to the left of the single rendered module (due to the imaging angle, as illustrated in orthogonal views, Figure 4.3.2).

In each glomerulus within this module, there are two visually apparent categories of changes after glutamate blockade: the response to the preferred compound increases after ionotropic glutamate blockade and the mixture response profile changes after glutamate blockade. The two E1 selective glomeruli had the largest relative increase in response to the preferred stimulus, easily seen by comparing the upper baseline and lower iGluR labeled panels in Figure 4.3.9f. The next largest increase is in the P2 selective glomerulus response to P2, which is less visible by eye but still large (see Figure 4.3.9c). In contrast the All-pregnanolone glomerulus undergoes the largest shift in pattern of responses to single stimuli., changing from a pattern of strongly P1-preferring to an equivalent All-pregnanolone pattern. That change in response pattern may belie the fact that the P2 response under baseline may have been partially attributable to the immediately adjacent All-pregnanolone responsive glomerulus.

Within this local context then, only the All-pregnanolone responsive glomerulus is described by a unique region of the potential response space. The consequences of that overlap are multiple: the increase in the P2 selective glomerulus response to P2 could be partially driven by lateral inhibition from the P2 responses in the All-pregnanolone glomerulus. In addition, the very large increase in E1 response after glutamate blockade in the two E1 selective glomeruli could be the result mutual and parallel inhibitory feedback.

In the mixture response profiles, we see a visible difference between single compound components of the responses and the mixture responses in all glomeruli within the module (4.3.9f, top row). For example, when the the apparent P1 selective ROI is activated in conjunction with the neighboring P2 selective ROI, there is a large attenuation in the P2 selective ROI response (quantified in Figure 4.3.9c) and this effect is dependent on ionotropic glutamate receptor signaling in the baseline condition. Similarly the differential between P1 and P2 responses in the All-pregnanolone glomerulus only occurs before glutamate blockade: after glutamate blockade it

becomes clear that the apparent P1 selective glomerulus is better characterized as an all pregnanolone responsive glomerulus. This same All-pregnanolone responsive glomerulus is effectively silenced by co-presentation of E1+P1 as a mixture. In contrast to the P1 selective glomeruli, this inhibition is clearly dependent on ionotropic glutamate blockade.

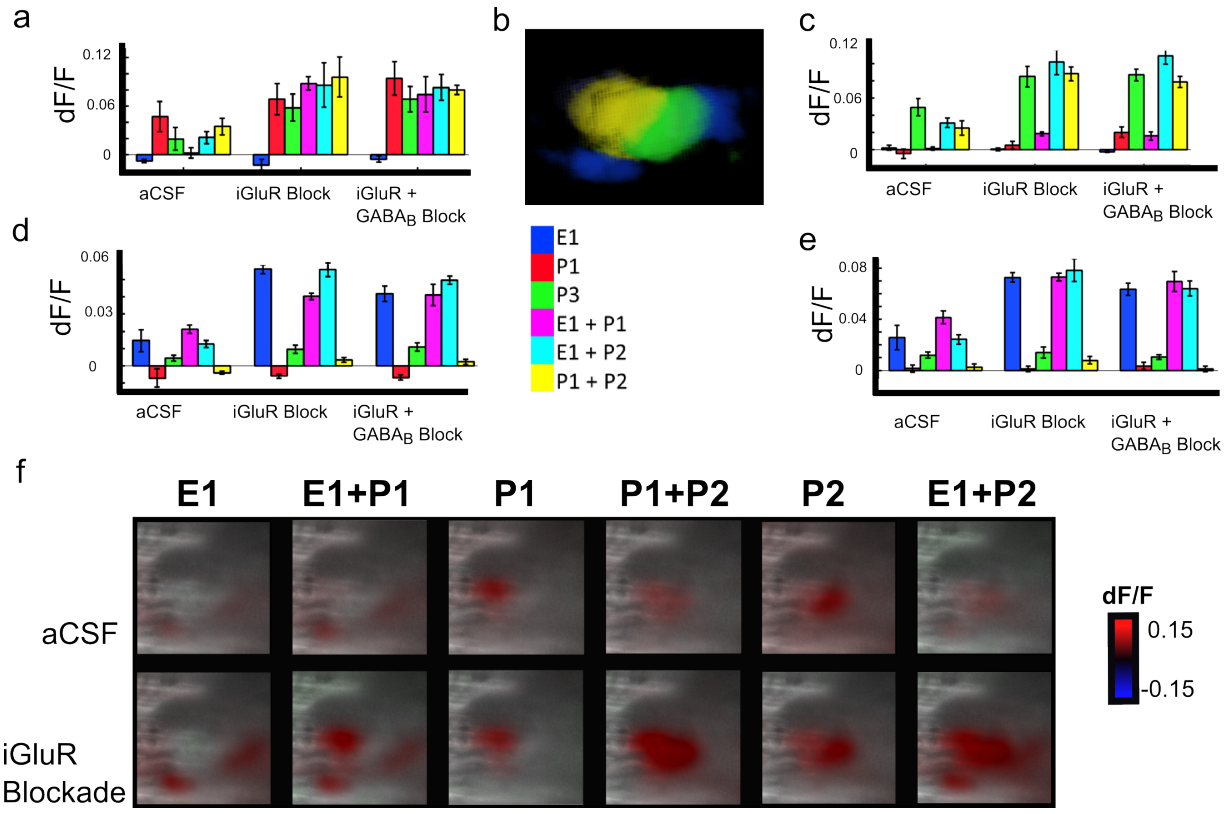

Figure 4.3.9: A selected module suggests that response tuning is modulated by surrounding activity via ionotropic glutamate receptor (iGluR) mediated feedback inhibition.
a,c-e) The mean responses over stimulus presentation and standard errs are presented for each component of the module.Colors (r/g/b) indicate pure compounds and their mixtures are represented as intermediate color mixtures, as indicated in the figure legend. Further blockade of $GABA_B$did not uncover covert inhibition.
f) We use an optical section through the selected regions to display the mean response for each stimulus and stimulus mixture, both as inputs under ionotropic glutamate blockade and after ionotropic glutamate dependent feedback. Note that the sequence is for display only: each trial was randomized.

While the single module shown in Figure 4.3.9 provides clear examples of both intraglomerular and local inhibitory effects, we also wished to characterized this on a population level. Specifically we tested whether was a difference in glutamate dependent inhibition in the three types

of stimulus selective glomeruli: E1 selective, all-pregnanolone responsive, P2 selective ,and P1 selective glomeruli.The E1 glomeruli are almost always associated with other glomeruli and thus provide a gross measure of the effect of local inhibition. In other words, since E1 glomeruli almost always have local partners, any glutamate mediated effects of mixtures are likely to reflect local inhibition. In contrast, P1-selective glomeruli which are almost always found on their own and thus not subject to local inhibition (other than the extrema, intraglomerular inhibition).

Figure 4.3.10

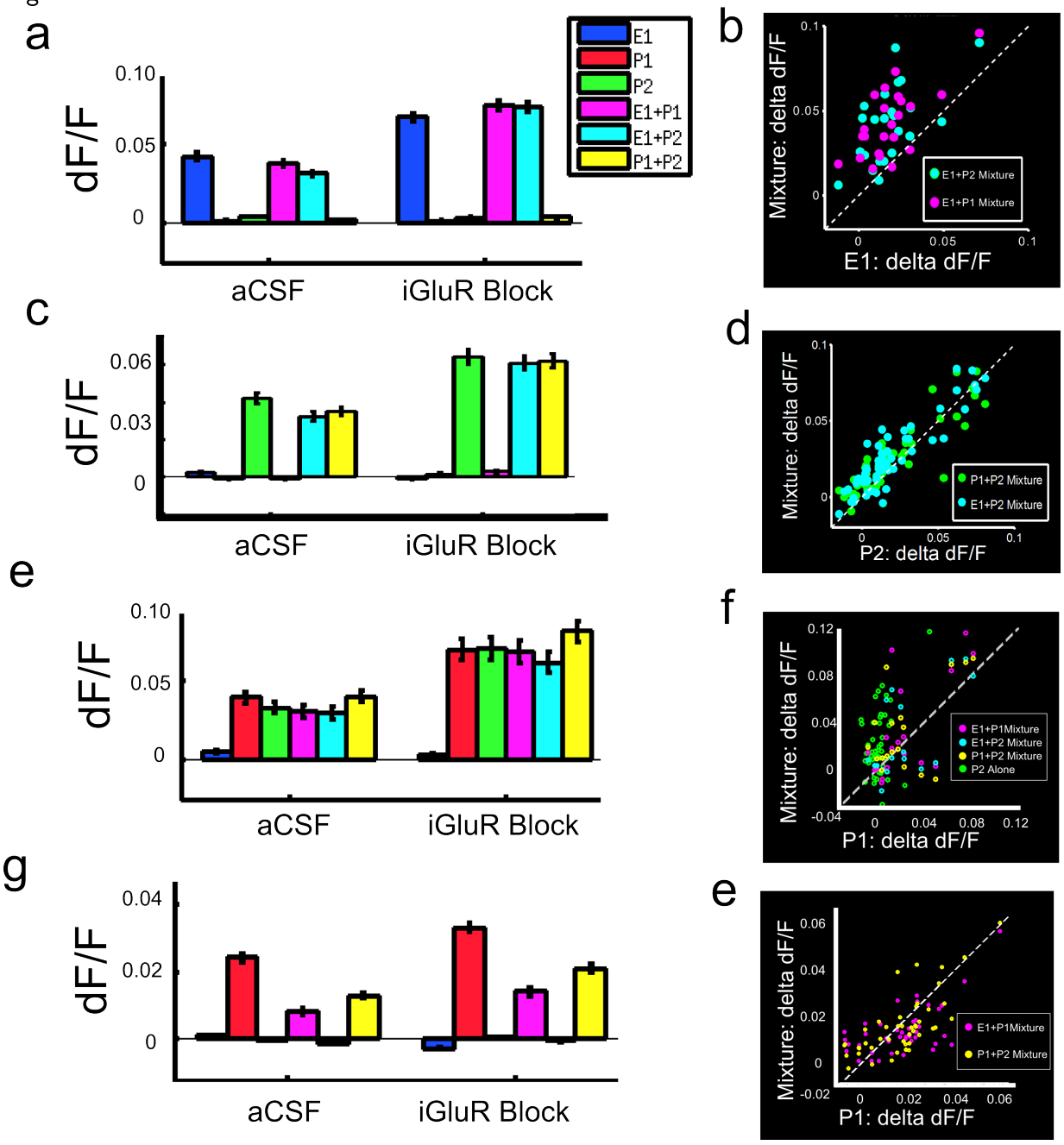
a
dF/F
0.10
0.05
0
aCSF
iGluR Block
E1
P1
P2
E1+P1
E1+P2
P1+P2
b
Mixture: delta dF/F
E1: delta dF/F
E1+P2 Mixture
E1+P1 Mixture
c
dF/F
0.06
0.03
0
aCSF
iGluR Block
d
Mixture: delta dF/F
P2: delta dF/F
P1+P2 Mixture
E1+P2 Mixture
e
dF/F
0.10
0.05
0
aCSF
iGluR Block
f
Mixture: delta dF/F
P1: delta dF/F
E1+P1Mixture
E1+P2 Mixture
P1+P2 Mixture
P2 Alone
g
dF/F
0.04
0.02
0
aCSF
iGluR Block
e
Mixture: delta dF/F
P1: delta dF/F
E1+P1Mixture
P1+P2 Mixture

Figure 4.3.10:
The two populations of E1 selective and all pregnanolone responsive glomeruli were subject to greater inhibition during mixture presentation than during preferred stimulus presentation, while the heterogeneously in and out of module P2-selctive group was relatively weakly but reliably inhibited.
(a-b) The E1 selective population mean response component to pure stimuli is of larger magnitude in the aCSF + ionotropic glutamate blockade relative to aCSF + vehicle.
(a) The E1 selective population mean response component to the preferred stimulus relative to stimulus mixtures is tested in a repeated measures ANOVA, see Table 4.3.1.
(b) The relative effect of inhibition magnitude is visualized as in the E1 responsive pop, a delta(dF/F) scatter plot.
(c-d) The P2 selective population mean response component to pure stimuli is of larger magnitude in the aCSF + ionotropic glutamate blockade relative to aCSF + vehicle, and the mixture responses to the P2 component are under greater inhbition than when it is presented alone (d), see Table 4.3.3.
(e-f) The all-Pregnanolone responsive population mean response component to the preferred stimuli relative to stimulus mixtures is most different in the additive case of P1+P2, however due the larger number of stimuli most within group means were not significantly different, see Table 4.3.4.
(g-h) The P1 selective population mean responses were scaled by ionotropic glutamate, but this effect was linearly seperable from independent effects of stimulus mixtures, see Table 4.3.2.

In addition to the standard iGluR blockade, we performed $GABA_B$ blockade as a third condition in one animal. Further blockade did not indicate the presence of covert feedback (svd based GLM, linear regression, slope=0.822 and intercept = 0.0007, norm of residuals = 0.365 and R2=0.77, see Methods Chapter 2.7). The observed decrement in fluorescence was similar to that seen between baseline and time/vehicle conditions in control animals (described earlier in Figure 4.3.5d).

We analyzed the E1 selective glomerulus ROI responses across all modules from the glutamate blockade experiments. As with the P1 selective glomeruli, the single ligand pattern of responses in the E1 selective glomeruli was similar between control and glutamate blockade conditions with an increase in response to the preferred stimulus (Figure 4.3.10a-b). Over all E1 selective glomeruli as a group, the population was inhibited by activity in surround, something which is difficult to appreciate based on the example module in Figure 4.3.9. More importantly, we examined the effect or magnitude change in response after ionotropic glutamate blockade for these E1 selective

glomeruli. For most E1 selective ROIs the magnitude increase for mixtures is greater than that for E1 alone. In other words, the effect of inhibition is greater on mixture responses than on single compounds, which is reflected in the scatter plot seen in Figure 4.3.10b, in which the values consistently fall above the line of equality (diagonal, x=y) indicating there is a a greater increase for mixtures relative to single compounds when glutamate blockade is present. The population responses were significantly different and there was a significant effect of glutamate blockade as measured by RM-ANOVA. When using the averaged Greenhouse-Geisser and Huyndt-Feldt correction penalties for asphericity, testing two factors (stimulus type and condition), we found an effect of stimulus type ($F(2, 106) = 3.3$, $p=4.1*10^{-2}$, effect size $\eta_p^2= 0.059$), an effect of condition ($F(1, 53) = 80.5$, $p=3.2*10^{-12}$, $\eta_p^2= 0.60$), and a stimulus by condition interaction ($F(2, 106)=18.1$, $p=1.7*10^{-7}$, $\eta_p^2=0.255$), with the first two factors combined accounting for a Sum of Squares Error (SSE) of 0.0722 with a Residual Error (RE) of 0.158 and Sum Square Total (SST) of 0.23. At this point interpretation requires an exact definition of our measure of effect size.

While the partial eta square value is not useful for direct comparisons across analyses, it very useful for assessing the explaining power of "adding a variable" in a RM-ANOVA (see Methods 2.7). Loosely, it describes the amount of unclaimed variance that is explained by a variable. More specifically, η_p^2 is the squared partial correlation of the dependent variable (change in fluorescence) with the variables. When there are no higher order interactions between dependent measures and variables, this is the r^2 value. In the context of the strong significant stimulus-by-type interaction, it accounts for an $\eta_p^2 = .255$ of RE or$\eta^2 * \frac{RE}{SST} = 0.175$ or 17.5% of the error, clearly represented in Figure 4.3.10b as a larger change in response to E1+P1 and E1+P2 mixtures relative to E1 alone after glutamate blockade (also in t-tests Table 4.3.1).

In contrast to the E1 selective glomeruli, the P2 selective population, some of which are heterogeneously located in and out of the defined modules, experienced smaller but significant effects of glutamate feedback (4.3.10c-d). Utilizing the same corrections for multiple comparisons

and asphericity as reported for E1, we observed significant effect of stimulus type ($F(2, 174) = 36.1$, $p=7.55*10^{-14}$, effect size $\eta_p^2= 0.293$), an effect of condition ($F(1, 87) = 91.2$, $p=3.33*10^{-15}$, $\eta_p^2= 0.512$), and a significant stimulus by condition interaction ($F(2, 174)=18.9$, $p=3.84*10^{-8}$, $\eta_p^2=0.178$), with the first two factors combined accounting for a SSE = 0.0624 with a Residual Error (RE) of 0.169 and Sum Square Total (SST) of 0.2314. Heeding our own admonishments, we keep our partial correlation metric in context and observe that the interaction accounts $\eta_p^2 * \frac{RE}{SST} = 0.13$, or about 13% of the differences observed in this population. However, in contrast to the E1 population the total variance observed was about equivalent over three n=174 glomeruli as opposed to 53. This smaller magnitude but considerably consistent interaction is manifest as a linear offset above the diagonal of Figure 4.3.10d, indicating consistently greater response increase to mixtures than to P2 alone after glutamate blockade (also see p-values in Table 4.3.3).

The last of the selective response groups, the P1 selective glomeruli, gives a result that is very different from the preceding two. These glomeruli were observed to be relatively far from any other recruited by other stimuli in the set, and for this population we observed an effect of stimulus type ($F(2, 90) = 45.9$, $p=1.79*10^{-14}$, effect size $\eta_p^2= 0.51$), an effect of condition ($F(1, 45) = 12.4$, $p=0.001$, $\eta_p^2= 0.22$), and an insignificant stimulus by condition interaction ($F(2, 90)=1.39$, $p=0.255$, $\eta_p^2=0.030$). In this population of isolated glomeruli, we see that the stimulus properties, the ligand-receptor interactions in the sensory neurons, describe almost all of the variance and that the effect of glutamate is independent of stimulus: the inhibition driven by glutamate blockade does not vary with recruitment of activity in other glomeruli by during mixture presentation.

The final group, the aAOB All-Pregnanolone responsive glomeruli, were in a sense very different from the P1 population. The effect of glutamate blockade is apparent and large (see Figure 4.3.10e) while the effect of stimulus type is smaller. The All-Pregnanolone group responded to a broader set of relevant stimuli and mixtures relative to all other populations: All-Pregnanolone glomeruli were responsive to every stimulus in the set other than E1. Similar to the other aAOB

types, we observed a significant effect of stimulus type (F(4,72)= 3.14, p=0.024, effect size η_p^2= 0.15), a significant effect of glutamate condition (F(1, 18) = 12.8, p=.022, η_p^2= 0.42), and a non-significant and small stimulus by condition interaction (F(1, 18)=1.25 p=0.31, η_p^2=0.06). This lack of stimulus by condition interaction and small (the smallest of all populations) by stimulus effect are reflected in Figure 4.3.10e, on the right-hand side under glutamate blockade the stimulus responses largely plateau. The exception to this plateau effect (or rough equality of magnitude) is the mixture containing two ligands to which this population responds. This additivity was apparent in individual glomeruli and the VSNs (see Figures 4.3.9 and 4.3.7).

Table 4.3.1: E1 Selective Comparisons

Mean Difference / Significance	t(53)	aCSF +Vehicle			iGluR Blockade		
		E1	E1+P1	E1+P2	E1	E1+P1	E1+P2
aCSF + Vehicle	E1	X	0.16	$4.6e^{-5}$	-	-	-
	E1+P1	-	X	$2.8e^{-5}$	-	-	-
	E1+P2	-	-	X	-	-	-
iGluR Blockade	E1	$1.6e^{-7}$	0.25	$2.0e^{-11}$	X	0.15	0.062
	E1+P1	$1.9e^{-5}$	$3.4e^{-10}$	$6.5e^{-6}$	-	X	>0.75
	E1+P2	$9.8e^{-5}$	$2.8e^{-9}$	$2.8e^{-9}$	-	-	X

For clarity, as all measures are reciprocal, between conditions significance values are located below the diagonal while within condition significance measures are located above the diagonal. Each has been Bonferroni corrected for multiple comparisons, n =15. Values of 0 were significant beyond numerical precision.

Table 4.3.2: P1 Selective Comparisons

Mean Difference Significance t(45)		aCSF +Vehicle			iGluR Blockade		
		P1	E1+P1	P1+P2	P1	E1+P1	P1+P2
aCSF + Vehicle	P1	X	$3.0e^{-7}$	$4.2e^{-5}$	-	-	-
	E1+P1	-	X	$9.3e^{-4}$	-	-	-
	P1+P2	-	-	X	-	-	-
iGluR Blockade	P1	$3.2e^{-2}$	$4.9e^{-12}$	$3.5e^{-9}$	X	$6.4e^{-9}$	$1.8e^{-4}$
	E1+P1	$7.5e^{-2}$	$5.7e^{-2}$	>0.75	-	X	$2.3e^{-3}$
	P1+P2	>0.75	1.6^{-4}	$3.4e^{-2}$	-	-	X

For clarity, as all measures are reciprocal, between conditions significance values are located below the diagonal while within condition significance measures are located above the diagonal. Each has been Bonferroni corrected for multiple comparisons, n =15. Values of 0 were significant beyond numerical precision. Empty (-) locations were empty for display purposes (see the 2nd potential location. X indicates the diagonal and n.s. values were insignificant before correcting for multiple comparisons.

Table 4.3.3: P2 Selective Comparisons

Mean Difference Significance t(87)		aCSF +Vehicle			iGluR Blockade		
		P2	E1+P2	P1+P2	P2	E1+P2	P1+P2
aCSF + Vehicle	P2	X	$4.6e^{-12}$	$8.5e^{-8}$	-	-	-
	E1+P2	-	X	$4.3e^{-4}$	-	-	-
	P1+P2	-	-	X	-	-	-
iGluR Blockade	P2	$1.2e^{-6}$	0	0	X	>0.75	>0.75
	E1+P2	$7.9e^{-5}$	0	$3.3e^{-14}$	-	X	>0.75
	P1+P2	$1.12e^{-5}$	0	$3.3e^{-14}$	-	-	X

For clarity, as all measures are reciprocal, between conditions significance values are located below the diagonal while within condition significance measures are located above the diagonal. Each has been Bonferroni corrected for multiple comparisons, n =15. Values of 0 were significant beyond numerical precision. Empty (-) locations were empty for display purposes (see the 2nd potential location. X indicates the diagonal and n.s. values were insignificant before correcting for multiple comparisons.

Table 4.3.4: All-Pregnanolone Selective Comparisons

Mean Difference Significance	t(18)	aCSF +Vehicle					iGluR Blockade				
		P1	P2	E1+P1	E1+P2	P1+P2	P1	P2	E1+P1	E1+P2	P1+P2
aCSF + Vehicle	P1	X	n.s.	n.s	.54	n.s.	-	-	-	-	-
	P2	-	X	n.s	n.s	.74	-	-	-	-	-
	E1+P1	-	-	X	n.s	n.s.	-	-	-	-	-
	E1+P2	-	-	-	X	n.s.	-	-	-	-	-
	P1+P2	-	-	-	-	X	-	-	-	-	-
iGluR Blockade	P1	0.053	.0443	$8.9e^{-4}$	$2.3e^{-3}$	0.16	X	n.s	n.s.	n.s.	n.s.
	P2	0.22	0.074	$7.9e^{-3}$	0.012	0.35	-	X	n.s.	n.s.	n.s.
	E1+P2	0.50	00.30	0.038	0.049	n.s.	-	-	X	n.s.	n.s.
	E1+P2	n.s.	0.52	.086	0.042	n.s.	-	-	-	X	$3.3e^{-3}$
	P1+P2	0.017	0.013	$1.2e^{-3}$	6.3^{-4}	0.044	-	-	-	-	X

For clarity, as all measures are reciprocal, between conditions significance values are located below the diagonal while within condition significance measures are located above the diagonal. Each has been Bonferroni corrected for multiple comparisons, n =15. Values of 0 were significant beyond numerical precision. Empty (-) locations were empty for display purposes (see the 2nd potential location. X indicates the diagonal and n.s. values were insignificant before correcting for multiple comparisons.

4.4 Discussion

Processing mixtures of stimuli is an important task of any chemosensory system. We tested the change in responses to mixtures of a set of sulfated steroids, which are know to be important cues for the mouse accessory olfactory system (AOS). We hypothesized that chemosensory responses to stimulus mixtures could potentially be modulated at three distinct hierarchical stages in processing: first at the level of ligand-receptor interactions, second at the single within glomerulus level, and third at the level of local modules within the AOB map. All three of these potential stages of processing were tested at the primary sensory neurons terminals within glomeruli of the accessory olfactory bulb (AOB). However we explicitly tested for mixture interactions at both the circuit level (in the bulb) and the neuroepithelium level (in the nose) to be certain that responses under pharmacological ionotropic glutamate blockade would be representative of the raw input to the circuit (Fig1a-d).

Stimulus mixture responses diverge from responses to single component stimulus responses by circuit-dependent and independent mechanisms.

We first utilized single compounds and mixtures both to identify previously reported types of glomeruli ([36]) and to evoke responses in different combinations of those glomeruli. Although we have previously demonstrated that multiple classes can be activated by our three stimuli, there were four particular distinguishable classes located in the anterior AOB and relevant to our hypotheses (Figure 4.3.3): E1 selective, P1 selective, all pregnanolone responsive, and P2 selective. The populations present in the posterior AOB (pAOB) were likely derived from V2R expressing VSNs, while the those that occurred in anterior AOB (aAOB) and were assumed to be distinct and from the more numerous V1R expressing VSNs. The pAOB populations were easily segmented anatomically in our data sets by using both anatomical and surface features to define an 3-dimensional coordinate system with an anterior/posterior plane (as in Figure 4.3.2a-d). The remaining four types of glomeruli were located in the aAOB and were well segmented by the stimulus set, thus once again demonstrating the reproducibility of the functionally defined

stimulus map in the AOB, in keeping with our previous work[36].

While we hypothesized that there would be differential responses to mixtures of stimuli, this was not the only possibility. If all VSNs were responsive only to their particular odorant stimulus, or agonist, and simply reported this activity out to an AOB glomerulus relay, it was conceivable that these responses would only be simply additive (specifically additive but not linearly so, as described by previous modeling of VSN mixture responses[4]). In fact, after defining our ROIs, which we have previously shown roughly correspond to glomeruli, we then demonstrate that there are not only non-additive effects of mixtures but even mixture suppression in many cases. Further we demonstrate that we can split those observations into distinct categories: suppression at the ligand-receptor level and inhibition within the neural circuit.

Vomeronasal Sensory Neuron chemo receptor-ligand interactions underlie circuit independent mixture interactions.

The aAOB (but not pAOB) P1 selective ROIs representing the P1 odor component were subject to mixture suppression at level of the peripheral VSN. We observed this effect under all experimental conditions: AOB ionotropic glutamate receptor blockade experiments, AOB time-vehicle control experiments, and VNO neuroepithelium experiments. In contrast, the All-Pregnanolone (P1/P2) responsive neurons demonstrated mixture additivity, which is in keeping with the concentration response series in the previous mapping study.

The mechanisms by which there may be mixture mediated suppression in the VNO remains somewhat unclear. Receptor antagonism has been reported at least once in the olfactory system [71], despite which the existence of olfactory antagonism (explicitly either that or the carefulness of analyses in the field) has been questioned [96]. It is not yet clear whether this novel finding represents strict biochemical antagonism. An antagonism seems intuitive and has at least two easily testable mechanisms: "competitive antagonism" at the receptor-ligand binding site and allosteric modulation anywhere else on the receptor outside of the stimulus binding site. A careful set of experiments could differentiate these two possible mechanisms from a very high affinity, low

maximum response type interaction which could also give rise to our observations (and would be a form of agonism). However, given that we are observing a biological response in a cell with a large number of receptors, any such data fit analysis would involve a both single and mixed ligand concentration and would likely need to be analyzed using a Hill cooperativity model ([4]).

Ionotropic glutamate receptor mediated feedback mediates circuit dependent mixture interactions.

The release of glutamate at the VSN axon terminals drives the excitatory output of the AOB but also interneurons within the glomerular layer. In blocking ionotropic glutamate, we blocked the evoked feedback onto the raw input at the glomerular VSN axon terminals. We found that the once a mixture had been encoded by the VSNs, that each component of this response was subject to ionotropic glutamate dependent feedback. We found that the ROIs selective for the P1 component of stimuli, were subject to feedback inhibition. However, this feedback inhibition was best explained by a constant factor that didn't interact significantly with the stimulus type: recruiting other regions with mixtures did not result in different amounts of inhibition. Perhaps this is not so surprising, given our previous findings that P1 selective glomeruli are much farther than expected by chance from P2 selective glomeruli.

Inhibition may also play a more general role in glomerular response tuning.

The strongest effect of glutamate blockade was a baseline change in response magnitude to the preferred stimulus by glomeruli in both the aAOB and pAOB. VSN activity is reported as occurring as firing bursts with stimuli reducing interburst intervals ([3]). We also assume that one general computational function of glomeruli is to facilitate the thresholding of population averaged responses ([21]). This hypothesis is quite attractive, because the AOS would likely need to represent chemosensory information across orders of magnitude different concentrations. One hypothesis then, is that the observed intraglomerular inhibition may serve to bot threshold inputs and decorrelate activity across different types of glomeruli.

The role of spatial organization in the AOB processing remains understudied

In sum, in this chapter we have demonstrated that there are differential responses to mixtures versus single stimuli in the accessory olfactory system. These differential responses are mediated by circuit dependent and independent processes in at logical, hierarchical levels: initial interactions between a given VSN receptor and ligands in the VNO, very local within glomerulus auto-inhibition, and lateral between glomerulus inhibition. We initially identified a group of P1 responsive glomeruli that showed differential (mixture suppression) responses to mixtures that was not mediated by glutamate blockade. However, in other glomeruli we also found differential (mixture inhibition) responses that were mediated by glutamate blockade. Further analyses indicate that this later group comprised most glomerulus types found in modules, providing a substrate for circuit mediated inhibition.

Population based analyses indicated there was a large effect of mixture inhibition for the E1 glomeruli, which are consistently co-localized with other glomeruli (E1,All-Pregnanolone, and P2). In contrast, there was no such effect in P1 glomeruli which are consistently located individually, while the effect of mixture inhibition on the P2 population, with constituents located both in and out of the module studied, was intermediate. Overall, this supports the presence of spatially distinct effects of inter-glomerular inhibition mediating the divergence of mixture representations from their individual component parts on entry to the circuit.

While we argue that the presence of some spatial organization, such as spatially associated modules of glomeruli, is important in the interpretation of our results, it bears keeping in mind the biological null hypothesis that organization, when present, is a result of normal developmental patterns rather than serving an explicit function. Instead of utilizing proximity of neural responses for some purpose or computation, it is possible that the glomeruli in modules result from the condensation of whichever VSNs project through a given branch of vomeronasal nerve. However, that sort of random distribution should still contain all types of VSNs projecting to the anterior AOB (aAOB) unless it was somehow organized to the contrary.

In further argument against the the null hypothesis that organization in the AOB is entirely

a stochastic result of development is the dichotomous representation of the P1 component in P1 verses P1 + E1 stimuli. The P1 component representation across the bulb, as occurring in both the P1 selective and all pregnanolone glomeruli, is nearly silenced at the aAOB glomeruli outside E1 associated modules and thus the P1 component response becomes represented predominantly locally within the E1 associated modules. However what happens to this representation post-synaptically remains unknown, but this sort of dichotomous representation could have even more profound implications as representations cross from the presynaptic terminal to the postsynaptic targets.

Chapter 5

Conclusions

In conjunction with others, I conducted a series of studies in which we explored the spatial relationships between the presynaptic glomeruli within the accessory olfactory bulb (AOB) of the mouse accessory olfactory system (AOS). These relationships, defined over both ethological and synthetic stimuli, generate what appears to be a modular association map. In subsequent experiments, I probed the role of these modules in representing chemosensory information, testing the activity across the circuit during the presentation of both mixtures and individual components of those mixtures, in order to better understand the neural processing performed in the glomerular layer.

We observed modular spatial relationships between glomerular types in the AOB

In Chapter 3, we were able to assess receptive field response characteristics using both natural urine stimuli and sulfated steroids. The glomerular regions were defined by the patterns of responses across stimulus sets, and specific types of glomeruli demonstrated strong, statistically reliable tendencies (statistically relative to chance) to be spatially near or far from other types of glomeruli. Whether olfactory maps were defined by patterns of responses to natural or to synthetic stimuli, we observed modular spatial relationships between those patterns of responses

These results are remarkable when considering that the potential response space is defined by

the more than 300 VSN receptor types is clearly large. This either makes our choice of stimulus sets very fortuitous, or points to a strong organizing principle. It would be interesting to see the full set of all possible relationships between regions, as I believe there are likely many more nuanced hypotheses to test with regards to the modular organization observed.

A finer grained probing of the response space could potentially reveal sharp boundaries around modules, gradual transitions resulting from the aggregate relative relationships, or even different types or classes of modules each their own organization. Any one type of organization could be coincident with some type of symmetry between glomerular types, perhaps resulting in something as simple as pairing of particular module types.

In addition, retrospection makes it clear that we could further refine our definitions of receptive fields by acquiring maps under glutamate blockade conditions. In the specific module example from Figure 4.3.9, we see a glomerulus appearing responsive to two pregnanolone stimuli but seemingly much more responsive to one of them. After ionotropic glutamate dependent feedback is blocked, that apparent difference disappears.

Perhaps an even more compelling direction is to further define receptive fields utilizing time-courses. There were region specific patterns of bimodal responses within some clusters that persisted across control and glutamate blockade conditions. It is quite likely that these features could be useful in further grouping regions. It would also be unsurprising if we saw interesting features relating to baseline firing rate which could be elicited via various pharmacological manipulations.

Olfactory responses in neurally adjacent glomeruli drove circuit interactions.

Although I do not assert to have defined all potential olfactory or chemical space (see the Introduction for commentary on that concept), we did find features of that space that the nervous system both organized and utilized to perform lateral inhibitory interactions. In direct converse to the numerous claims that there was no lateral inhibition in the MOB, we observed significant lateral inhibition in the AOB.

The full characteristics of the inhibition remains to be elucidated. However, I have demonstrated cases of a module in which the E1 glomeruli exerted extraordinary inhibition on other components of the module, yet had a relatively small effect of inhibition by neighboring glomeruli.

On comparison of that module to the E1 glomeruli across all modules in the population scatter data, we see that those in this module would be points near the diagonal, that is they experienced equivalent inhibition when E1 was presented and when mixtures of E1 were presented. This was not an example of the mean but an example of rather of the diversity of potential interactions within modules

This does not mean that E1 glomeruli are not inhibiting one another in these modules. After all, E1 glomeruli undergo the single largest glutamate blockade condition-by-response shift of any population under study, rather it suggests that the inhibition may just be more complex.

The characteristics of inhibition should be directly testable by a series of models: a type based model, a stochastic local connectivity model, and a geometric model. The simplest result would be if the diversity observed is the result of a set of rules transforming activity, relative size, and distance into an effect of inhibition that just varies with the relative positions and sizes of glomeruli in different modules. A type based model of inhibition may be able to disambiguate this as "within type" increase in inhibition within specific modules, but that would be new information as we believe we have observed such module diversity in the population mean responses. The strength of the type based model would be to unify weaker observations of tendencies toward directional inhibition, for example some difficult to discern but strong general directedness of each glomerulus by type, such as E1->All-Pregnanolone->P2->E1.

While each individual model would have limitations, together they have the potential to test for parameters that can seed further testable hypotheses.

Sufficiently refined definitions of glomerulus type may provide insight into what role lateral inhibition plays in olfaction.

Perhaps most striking is the observation that the presentation of E1 suppresses a specific set of responses to P1 (allopregnanolone sulfate). Alone this phenomenon strongly indicates that further probing of the receptive fields should evaluate and utilize the effects of mixtures. Even stimulus sets using natural stimuli could potentially be better defined by including mixtures. However the effect become substantially more intriguing when considered in the context to of circuit mediated interactions.

The set of P1 glomeruli suppressed were those that occurred "outside" of the modules defined by our single and binary stimulus mixture set. However, the P1 stimulus was also represent in All-Pregnanolone glomeruli as well as in the pAOB glomeruli.

This effect could be an idiosyncrasy, or perhaps the single most striking observation of all. When P1 was co-presented with E1, we observed that at the population level the magnitude of E1 suppression of those "outside" P1 glomeruli greater than that of glutamate mediated feedback. As one can see from comparing respective columns in the population data, the effect of the E1+P1 mixture at the whole map level (in the aAOB) is to "shift" the brunt of the P1 mixture component activity into those E1 selective and All-Pregnanolone responsive glomeruli within modules, which may, in effect, force direct comparison of the two evoked responses.

If this "shift" effect between regions of glomerular representation were to generalize into other glomerulus or stimulus types, it may represent an olfactory mechanism for forcing decorrelation of chemical cues in a context specific manner– a logic gating for olfaction. This hypothesis is directly testable in the excitatory mitral cells that serve as the output from the circuit.

Alternatively the "shift" effect may be a more qualitative "don't miss" type of signal. If this is the case, we should not miss it. Given that many compounds sensed by the system are steroid hormone metabolites, the natural ligands that activate these distant suppressible glomeruli and are potentially silenced by E1 (or conversely those that silence activity in a manner analogous to E1) may be chemosensory cues that are particularly biologically relevant.

Regardless of whether this suppression phenomenon represents a "don't miss" signal or a more general "shift" mechanism to focal, within module comparisons, the ability to disproportionately alter activity across the bulb may be a major asset in testing hypothesis about circuit function. The dual activation of glomeruli and mixture-receptor suppression allows for simultaneous recruiting of activity in some regions while silencing it at the chemoreceptor in other regions. The potential asset is that this silencing would occur without evoking a coincident large circuit response, allowing more nuanced recruitment and silencing of glomeruli.

Summary

In the end, while I have defined some organizing principles in the chemosensory map of AOS as well as instances where the neuronal representations of olfactory space are utilized to drive lateral inhibition, there, as always, remains more to be learned. However, my experiences in studying, testing, and modeling the accessory olfactory system has fulfilled what I believe to be one of the fundamental purposes of academia: the generation and maintenance of a broad base of knowledge and skills. What we have striven to learn or do, in the end, is often far from within our control. In the introduction I mention, by way of Churchland and Sejnowski, the eighteenth century written work of two different men, each of whom was a strong proponent of their particular views on the fundamental process of vision. Neither was entirely right nor entirely wrong, but neither saw the full fruition of their ideas during their lifetime. Each hypothesis and experiment moves the field forward, one small bit of knowledge at time.

Bibliography

[1] Adelbert AMES and BS GURIAN. Electrical recordings from isolated mammalian retina mounted as a membrane. *Archives of Ophthalmology*, 70:837–41, December 1963.

[2] Armen C Arevian, Vikrant Kapoor, and Nathaniel N Urban. Activity-dependent gating of lateral inhibition in the mouse olfactory bulb. *Nature neuroscience*, 11(1):80–7, January 2008.

[3] Hannah A Arnson and Timothy E Holy. Chemosensory burst coding by mouse vomeronasal sensory neurons. *Journal of neurophysiology*, 106(1):409–20, July 2011.

[4] Hannah A Arnson and Timothy E Holy. Robust encoding of stimulus identity and concentration in the accessory olfactory system. *The Journal of neuroscience : the official journal of the Society for Neuroscience*, 33(33):13388–97, August 2013.

[5] V Aroniadou-Anderjaska, F M Zhou, C a Priest, M Ennis, and M T Shipley. Tonic and synaptically evoked presynaptic inhibition of sensory input to the rat olfactory bulb via GABA(B) heteroreceptors. *Journal of neurophysiology*, 84(3):1194–203, September 2000.

[6] J L Aungst, P M Heyward, A C Puche, S V Karnup, A Hayar, G Szabo, and M T Shipley. Centre-surround inhibition among olfactory bulb glomeruli. *Nature*, 426(6967):623–9, December 2003.

[7] M Behrens and W Meyerhof. Mammalian bitter taste perception. *Results and problems in cell differentiation*, 47:203–20, January 2009.

[8] L Belluscio and L C Katz. Symmetry, stereotypy, and topography of odorant representations in mouse olfactory bulbs. *The Journal of neuroscience : the official journal of the Society for Neuroscience*, 21(6):2113–22, March 2001.

[9] L Belluscio, G Koentges, R Axel, and C Dulac. A map of pheromone receptor activation in the mammalian brain. *Cell*, 97(2):209–20, April 1999.

[10] Y Ben-Shaul, L C Katz, R Mooney, and C Dulac. In vivo vomeronasal stimulation reveals sensory encoding of conspecific and allospecific cues by the mouse accessory olfactory bulb. *Proceedings of the National Academy of Sciences of the United States of America*, 107(11):5172–7, March 2010.

[11] K. P. Bhargava and K. S. Dixit. Role of the chemoreceptor trigger zone in histamine-induced emesis. *British journal of pharmacology*, 34(3):508–13, November 1968.

[12] Thomas Bozza, John P McGann, Peter Mombaerts, and Matt Wachowiak. In vivo imaging of neuronal activity by targeted expression of a genetically encoded probe in the mouse. *Neuron*, 42(1):9–21, April 2004.

[13] J Breuer. *Die Selbststeuerung der Athmung durch den Nervus vagus*. 1868.

[14] L Buck and R Axel. A novel multigene family may encode odorant receptors: a molecular basis for odor recognition. *Cell*, 65(1):175–87, April 1991.

[15] Sarah M Burke, Dick J Veltman, Johannes Gerber, Thomas Hummel, and Julie Bakker. Heterosexual men and women both show a hypothalamic response to the chemo-signal androstadienone. *PloS one*, 7(7):e40993, January 2012.

[16] C Bushdid, M O Magnasco, L B Vosshall, and a Keller. Humans can discriminate more than 1 trillion olfactory stimuli. *Science (New York, N.Y.)*, 343(6177):1370–2, March 2014.

[17] Matteo Carandini, David J Heeger, and J Anthony Movshon. Linearity and normalization in simple cells of the macaque primary visual cortex. *The Journal of neuroscience : the official journal of the Society for Neuroscience*, 17(21):8621–44, November 1997.

[18] Xiaoke Chen, Mariano Gabitto, Yueqing Peng, Nicholas J P NJP Ryba, and Charles S Zuker. A gustotopic map of taste qualities in the mammalian brain. *Science (New York, N.Y.)*, 333(6047):1262–6, September 2011.

[19] Ya-Hui Chou, Maria L Spletter, Emre Yaksi, Jonathan C S Leong, Rachel I Wilson, and Liqun Luo. Diversity and wiring variability of olfactory local interneurons in the Drosophila antennal lobe. *Nature neuroscience*, 13(4):439–49, April 2010.

[20] P S Churchland and T J Sejnowski. Perspectives on cognitive neuroscience. *Science (New York, N.Y.)*, 242(4879):741–5, November 1988.

[21] Thomas a T.A. Cleland. Early transformations in odor representation. *Trends in neurosciences*, 33(3):130–139, March 2010.

[22] Dorin Comaniciu and Peter Meer. Mean Shift : A Robust Approach Toward Feature Space Analysis. *IEEE Transactions of Pattern Analysis and Machine Intelligence*, 24(5):603–619, 2002.

[23] D F Cottrell and A Iggo. Mucosal enteroceptors with vagal afferent fibres in the proximal duodenum of sheep. *The Journal of physiology*, 354:497–522, September 1984.

[24] J de Olmos, H Hardy, and L Heimer. The afferent connections of the main and the accessory olfactory bulb formations in the rat: an experimental HRP-study. *The Journal of comparative neurology*, 181(2):213–44, September 1978.

[25] Karina Del Punta, Adam Puche, Niels C Adams, Ivan Rodriguez, and Peter Mombaerts. A divergent pattern of sensory axonal projections is rendered convergent by second-order neurons in the accessory olfactory bulb. *Neuron*, 35(6):1057–66, September 2002.

[26] Graciana Diez-Roux and Andrea Ballabio. Sulfatases and human disease. *Annual review of genomics and human genetics*, 6:355–79, January 2005.

[27] Wayne I Doyle, Gary F Hammen, and Julian P Meeks. Ex vivo preparations of the intact vomeronasal organ and accessory olfactory bulb. *Journal of visualized experiments : JoVE*, (90), January 2014.

[28] C a Dudley and R L Moss. Activation of an anatomically distinct subpopulation of accessory olfactory bulb neurons by chemosensory stimulation. *Neuroscience*, 91(4):1549–56, January 1999.

[29] M Ennis, F M Zhou, K J Ciombor, V Aroniadou-Anderjaska, A Hayar, E Borrelli, L a Zimmer, F Margolis, and M T Shipley. Dopamine D2 receptor-mediated presynaptic inhibition of olfactory nerve terminals. *Journal of neurophysiology*, 86(6):2986–97, December 2001.

[30] Marion E Frank and Thomas P Hettinger. An axis of good and awful in odor reception. *Nature neuroscience*, 14(11):1360–2, November 2011.

[31] Helene Freiser and Qing Jiang. Optimization of the enzymatic hydrolysis and analysis of plasma conjugated gamma-CEHC and sulfated long-chain carboxychromanols, metabolites of vitamin E. *Analytical biochemistry*, 388(2):260–5, May 2009.

[32] A P French and J C Warren. Sulfatase activity in the human placenta. *Steroids*, 8(1):79–85, July 1966.

[33] T a Fuller and J L Price. Putative glutamatergic and/or aspartatergic cells in the main and accessory olfactory bulbs of the rat. *The Journal of comparative neurology*, 276(2):209–18, October 1988.

[34] Luciane H Gargaglioni, Lynn K Hartzler, and Robert W Putnam. The locus coeruleus and central chemosensitivity. *Respiratory physiology & neurobiology*, 173(3):264–73, October 2010.

[35] Rafi Haddad, Rehan Khan, Yuji K Takahashi, Kensaku Mori, David Harel, and Noam Sobel. A metric for odorant comparison. *Nature methods*, 5(5):425–9, May 2008.

[36] Gary F. Hammen, Diwakar Turaga, Timothy E. Holy, and Julian P. Meeks. Functional organization of glomerular maps in the mouse accessory olfactory bulb. *Nature neuroscience*, 17(7):953–61, July 2014.

[37] Sarah R Hanson, Michael D Best, and Chi-Huey Wong. Sulfatases: structure, mechanism, biological activity, inhibition, and synthetic utility. *Angewandte Chemie (International ed. in English)*, 43(43):5736–63, November 2004.

[38] Abdallah Hayar, Sergei Karnup, Matthew Ennis, and Michael T Shipley. External tufted cells: a major excitatory element that coordinates glomerular activity. *The Journal of neuroscience : the official journal of the Society for Neuroscience*, 24(30):6676–85, July 2004.

[39] Jie He, Limei Ma, Sangseong Kim, Junichi Nakai, and C Ron Yu. Encoding gender and individual information in the mouse vomeronasal organ. *Science (New York, N.Y.)*, 320(5875):535–8, April 2008.

[40] David J Heeger. Modeling simple-cell direction selectivity with normalized, half-squared, linear operators. *Journal of neurophysiology*, 70(5):1885–98, November 1993.

[41] Rebecca C Hendrickson, Sandra Krauthamer, James M Essenberg, and Timothy E Holy. Inhibition shapes sex selectivity in the mouse accessory olfactory bulb. *The Journal of neuroscience : the official journal of the Society for Neuroscience*, 28(47):12523–34, November 2008.

[42] Ewald Hering. *Zur Lehre vom Lichtsinne (On the Doctrine of the Sensation of Light)*. Gerold's Sohn, Vienna, second, un edition, 1878.

[43] Terrence F Holekamp, Diwakar Turaga, and Timothy E Holy. Fast three-dimensional fluorescence imaging of activity in neural populations by objective-coupled planar illumination microscopy. *Neuron*, 57(5):661–72, March 2008.

[44] T E Holy, C Dulac, and M Meister. Responses of vomeronasal neurons to natural stimuli. *Science (New York, N.Y.)*, 289(5484):1569–72, September 2000.

[45] Fong-fu Hsu, Francesco Nodari, Lung-fa Kao, Xiaoyan Fu, Terrence F Holekamp, John Turk, and Timothy E Holy. Structural characterization of sulfated steroids that activate mouse pheromone-sensing neurons. *Biochemistry*, 47(52):14009–19, December 2008.

[46] D H HUBEL and T N WIESEL. Receptive fields, binocular interaction and functional architecture in the cat's visual cortex. *The Journal of physiology*, 160:106–54, January 1962.

[47] J S Isaacson and H Vitten. GABA(B) receptors inhibit dendrodendritic transmission in the rat olfactory bulb. *J. Neurosci.*, 23(6):2032–2039, 2003.

[48] Tomohiro Ishii and Peter Mombaerts. Expression of nonclassical class I major histocompatibility genes defines a tripartite organization of the mouse vomeronasal system. *The Journal of neuroscience : the official journal of the Society for Neuroscience*, 28(10):2332–41, March 2008.

[49] Yoh Isogai, Sheng Si, Lorena Pont-Lezica, Taralyn Tan, Vikrant Kapoor, Venkatesh N. Murthy, and Catherine Dulac. Molecular organization of vomeronasal chemoreception. *Nature*, 478(7368):241–5, October 2011.

[50] Brett A Johnson, Haleh Farahbod, Zhe Xu, Sepideh Saber, and Michael Leon. Local and global chemotopic organization: general features of the glomerular representations of aliphatic odorants differing in carbon number. *The Journal of comparative neurology*, 480(2):234–49, December 2004.

[51] Andreas Keller, Hanyi Zhuang, Qiuyi Chi, Leslie B Vosshall, and Hiroaki Matsunami. Genetic variation in a human odorant receptor alters odour perception. *Nature*, 449(7161):468–72, September 2007.

[52] Emi Kiyokage, Yu-Zhen Pan, Zuoyi Shao, Kazuto Kobayashi, Gabor Szabo, Yuchio Yanagawa, Kunihiko Obata, Hideyuki Okano, Kazunori Toida, Adam C Puche, and Michael T Shipley. Molecular identity of periglomerular and short axon cells. *The Journal of neuroscience : the official journal of the Society for Neuroscience*, 30(3):1185–96, January 2010.

[53] Egon P Köster, Per Mø ller, and Jozina Mojet. A "Misfit" Theory of Spontaneous Conscious Odor Perception (MITSCOP): reflections on the role and function of odor memory in everyday life. *Frontiers in psychology*, 5(February):64, January 2014.

[54] Hadas Lapid, Sagit Shushan, Anton Plotkin, Hillary Voet, Yehudah Roth, Thomas Hummel, Elad Schneidman, and Noam Sobel. Neural activity at the human olfactory epithelium reflects olfactory perception. *Nature Neuroscience*, 14(11):1455–1461, September 2011.

[55] Jorge Larriva-Sahd. The accessory olfactory bulb in the adult rat: a cytological study of its cell types, neuropil, neuronal modules, and interactions with the main olfactory system. *The Journal of comparative neurology*, 510(3):309–50, September 2008.

[56] Timothy R. Levine and Craig R. Hullett. Eta Squared, Partial Eta Squared, and Misreporting of Effect Size in Communication Research. *Human Communication Research*, 28(4):612–625, October 2002.

[57] Minmin Luo, Michale S Fee, and Lawrence C Katz. Encoding pheromonal signals in the accessory olfactory bulb of behaving mice. *Science (New York, N.Y.)*, 299(5610):1196–201, February 2003.

[58] Limei Ma, Qiang Qiu, Stephen Gradwohl, Aaron Scott, Elden Q Yu, Richard Alexander, Winfried Wiegraebe, and C Ron Yu. Distributed representation of chemical features and

tunotopic organization of glomeruli in the mouse olfactory bulb. *Proceedings of the National Academy of Sciences of the United States of America*, 109(14):5481–6, April 2012.

[59] W H Marshall, C N Woolsey, and P Bard. CORTICAL REPRESENTATION OF TACTILE SENSIBILITY AS INDICATED BY CORTICAL POTENTIALS. *Science (New York, N.Y.)*, 85(2207):388–90, April 1937.

[60] John P McGann, Nicolás Pírez, Melanie a Gainey, Christina Muratore, Adam S Elias, and Matt Wachowiak. Odorant representations are modulated by intra- but not interglomerular presynaptic inhibition of olfactory sensory neurons. *Neuron*, 48(6):1039–53, December 2005.

[61] Julian P Meeks, Hannah a Arnson, and Timothy E Holy. Representation and transformation of sensory information in the mouse accessory olfactory system. *Nature neuroscience*, 13(6):723–30, June 2010.

[62] Julian P Meeks and Timothy E Holy. An ex vivo preparation of the intact mouse vomeronasal organ and accessory olfactory bulb. *Journal of neuroscience methods*, 177(2):440–7, March 2009.

[63] Julian P Meeks and Timothy E Holy. Electrical recordings from the accessory olfactory bulb in VNO-AOB ex vivo preparations. *Methods in molecular biology (Clifton, N.J.)*, 1068:237–46, January 2013.

[64] N Mei. Vagal glucoreceptors in the small intestine of the cat. *The Journal of physiology*, 282(3):485–506, September 1978.

[65] M Meister and T Bonhoeffer. Tuning and topography in an odor map on the rat olfactory bulb. *The Journal of neuroscience : the official journal of the Society for Neuroscience*, 21(4):1351–60, February 2001.

[66] M M Merzenich, P L Knight, and G L Roth. Representation of cochlea within primary auditory cortex in the cat. *Journal of neurophysiology*, 38(2):231–49, March 1975.

[67] R L Moore. A STUDY OF THE HERING-BREUER REFLEX. *The Journal of experimental medicine*, 46(5):819–37, October 1927.

[68] Wouterlood FF Mugnaini E, Oertel WH. Immunocytochemical localization of GABA neurons and dopamine neurons in the rat main and accessory olfactory bulbs. *Neurosci Lett.*, 47(3):221–226, 1984.

[69] Venkatesh N Murthy. Olfactory maps in the brain. *Annual review of neuroscience*, 34:233–58, January 2011.

[70] Francesco Nodari, Fong-Fu Hsu, Xiaoyan Fu, Terrence F Holekamp, Lung-Fa Kao, John Turk, and Timothy E Holy. Sulfated steroids as natural ligands of mouse pheromone-sensing neurons. *The Journal of neuroscience : the official journal of the Society for Neuroscience*, 28(25):6407–18, June 2008.

[71] Yuki Oka, Masayo Omura, Hiroshi Kataoka, and Kazushige Touhara. Olfactory receptor antagonism between odorants. *The EMBO journal*, 23(1):120–6, January 2004.

[72] Tsviya Olender, Sebastian M Waszak, Maya Viavant, Miriam Khen, Edna Ben-Asher, Alejandro Reyes, Noam Nativ, Charles J Wysocki, Dongliang Ge, and Doron Lancet. Personal receptor repertoires: olfaction as a model. *BMC genomics*, 13:414, January 2012.

[73] Shawn R Olsen and Rachel I Wilson. Lateral presynaptic inhibition mediates gain control in an olfactory circuit. *Nature*, 452(7190):956–60, April 2008.

[74] A S Paintal. Vagal sensory receptors and their reflex effects. *Physiological reviews*, 53(1):159–227, January 1973.

[75] a J Pinching and T P Powell. The neuron types of the glomerular layer of the olfactory bulb. *Journal of cell science*, 9(2):379–409, September 1971.

[76] Nicolás Pírez and Matt Wachowiak. In vivo modulation of sensory input to the olfactory bulb by tonic and activity-dependent presynaptic inhibition of receptor neurons. *The Journal*

of neuroscience : the official journal of the Society for Neuroscience, 28(25):6360–71, June 2008.

[77] Joseph L Price. Comparative aspects of amygdala connectivity. *Annals of the New York Academy of Sciences*, 985:50–8, April 2003.

[78] TC Pritchard and R Norgren. Gustatory system. In G Paxinos and J Mai, editors, *The Human Nervous System.*, chapter Gustatory, pages 1171–1195. Elsevier, New York, NY, 2nd editio edition, 2004.

[79] K J Ressler, S L Sullivan, and L B Buck. Information coding in the olfactory system: evidence for a stereotyped and highly organized epitope map in the olfactory bulb. *Cell*, 79(7):1245–55, December 1994.

[80] I Rodriguez, P Feinstein, and P Mombaerts. Variable patterns of axonal projections of sensory neurons in the mouse vomeronasal system. *Cell*, 97(2):199–208, April 1999.

[81] P Rozin. "Taste-smell confusions" and the duality of the olfactory sense. *Perception & psychophysics*, 31(4):397–401, April 1982.

[82] B D Rubin and L C Katz. Optical imaging of odorant representations in the mammalian olfactory bulb. *Neuron*, 23(3):499–511, July 1999.

[83] F Scalia and S S Winans. The differential projections of the olfactory bulb and accessory olfactory bulb in mammals. *The Journal of comparative neurology*, 161(1):31–55, May 1975.

[84] Edward S Schelegle. Functional morphology and physiology of slowly adapting pulmonary stretch receptors. *The anatomical record. Part A, Discoveries in molecular, cellular, and evolutionary biology*, 270(1):11–6, January 2003.

[85] Z Shao, A C Puche, E Kiyokage, G Szabo, and M T Shipley. Two GABAergic Intraglomerular Circuits Differentially Regulate Tonic and Phasic Presynaptic Inhibition of Olfactory Nerve Terminals. *Journal of Neurophysiology*, pages 1988 –2001, 2009.

[86] Edward R Soucy, Dinu F Albeanu, Antoniu L Fantana, Venkatesh N Murthy, and Markus Meister. Precision and diversity in an odor map on the olfactory bulb. *Nature neuroscience*, 12(2):210–20, February 2009.

[87] Richard J Stevenson and Tuki Attuquayefio. Human olfactory consciousness and cognition: its unusual features may not result from unusual functions but from limited neocortical processing resources. *Frontiers in psychology*, 4(November):819, January 2013.

[88] C a Strott. Steroid sulfotransferases. *Endocrine reviews*, 17(6):670–97, December 1996.

[89] Yuji K Takahashi, Masahide Kurosaki, Shuichi Hirono, and Kensaku Mori. Topographic representation of odorant molecular features in the rat olfactory bulb. *Journal of neurophysiology*, 92(4):2413–27, October 2004.

[90] J B Tenenbaum, V de Silva, and J C Langford. A global geometric framework for nonlinear dimensionality reduction. *Science (New York, N.Y.)*, 290(5500):2319–23, December 2000.

[91] Igor V Tetko, Johann Gasteiger, Roberto Todeschini, Andrea Mauri, David Livingstone, Peter Ertl, Vladimir a Palyulin, Eugene V Radchenko, Nikolay S Zefirov, Alexander S Makarenko, Vsevolod Yu Tanchuk, and Volodymyr V Prokopenko. Virtual computational chemistry laboratory–design and description. *Journal of computer-aided molecular design*, 19(6):453–63, June 2005.

[92] Lin Tian, S Andrew Hires, Tianyi Mao, Daniel Huber, M Eugenia Chiappe, Sreekanth H Chalasani, Leopoldo Petreanu, Jasper Akerboom, Sean a McKinney, Eric R Schreiter, Cornelia I Bargmann, Vivek Jayaraman, Karel Svoboda, and Loren L Looger. Imaging neural activity in worms, flies and mice with improved GCaMP calcium indicators. *Nature methods*, 6(12):875–81, December 2009.

[93] Kazushige Touhara, editor. *Pheromone Signaling: Methods and Protocols*, volume 1068 of *Methods in Molecular Biology*. Humana Press, Totowa, NJ, 2013.

[94] S. Tryfon, Th. Kontakiotis, Eu. Mavrofridis, and D. Patakas. Hering-Breuer Reflex in Normal Adults and in Patients with Chronic Obstructive Pulmonary Disease and Interstitial Fibrosis. *Respiration*, 68(2):140–144, 2001.

[95] Diwakar Turaga and Timothy E Holy. Organization of vomeronasal sensory coding revealed by fast volumetric calcium imaging. *The Journal of neuroscience : the official journal of the Society for Neuroscience*, 32(5):1612–21, February 2012.

[96] L. Turin. *Rational Odorant Design*, chapter 11, pages 261–273. Blackwell Publishing Ltd., 2009.

[97] N Uchida, Y K Takahashi, M Tanifuji, and K Mori. Odor maps in the mammalian olfactory bulb: domain organization and odorant structural features. *Nature neuroscience*, 3(10):1035–43, October 2000.

[98] Einar Uggerud. Reactivity trends and stereospecificity in nucleophilic substitution reactions. *Journal of Physical Organic Chemistry*, 19(8-9):461–466, August 2006.

[99] Arnoldus J R van Gestel and Joerg Steier. Autonomic dysfunction in patients with chronic obstructive pulmonary disease (COPD). *Journal of thoracic disease*, 2(4):215–22, December 2010.

[100] Robert Vassar, S K Chao, Raquel Sitcheran, J M Nuñez, L B Vosshall, and Richard Axel. Topographic organization of sensory projections to the olfactory bulb. *Cell*, 79(6):981–91, December 1994.

[101] Jean-Charles Viemari and Andrew K Tryba. Bioaminergic neuromodulation of respiratory rhythm in vitro. *Respiratory physiology & neurobiology*, 168(1-2):69–75, August 2009.

[102] Dejan Vucinic, Lawrence B Cohen, and Efstratios K\ Kosmidis. Interglomerular Center-Surround Inhibition Shapes Odorant-Evoked Input to the Mouse Olfactory Bulb In Vivo. *Journal of Neurophysiology*, pages 1881–1887, 2006.

[103] Matt Wachowiak and Lawrence B Cohen. Representation of Odorants by Receptor Neuron Input to the Mouse Olfactory Bulb. *Neuron*, 32(4):723–735, November 2001.

[104] Matt Wachowiak, John P McGann, Philip M Heyward, Zuoyi Shao, Adam C Puche, and Michael T Shipley. Inhibition [corrected] of olfactory receptor neuron input to olfactory bulb glomeruli mediated by suppression of presynaptic calcium influx. *Journal of neurophysiology*, 94(4):2700–12, October 2005.

[105] Shlomo Wagner, Amy L Gresser, A Thomas Torello, and Catherine Dulac. A multireceptor genetic approach uncovers an ordered integration of VNO sensory inputs in the accessory olfactory bulb. *Neuron*, 50(5):697–709, June 2006.

[106] Jennifer D Whitesell, Kyle A Sorensen, Brooke C Jarvie, Shane T Hentges, and Nathan E Schoppa. Interglomerular lateral inhibition targeted on external tufted cells in the olfactory bulb. *The Journal of neuroscience : the official journal of the Society for Neuroscience*, 33(4):1552–63, January 2013.

[107] S Wray, S M Fueshko, K Kusano, and H Gainer. GABAergic neurons in the embryonic olfactory pit/vomeronasal organ: maintenance of functional GABAergic synapses in olfactory explants. *Developmental biology*, 180(2):631–45, December 1996.

[108] Claire Wyart, Wallace W Webster, Jonathan H Chen, Sarah R Wilson, Andrew McClary, Rehan M Khan, and Noam Sobel. Smelling a single component of male sweat alters levels of cortisol in women. *The Journal of neuroscience : the official journal of the Society for Neuroscience*, 27(6):1261–5, February 2007.

[109] Pei Sabrina Xu and Timothy E Holy. Whole-mount imaging of responses in mouse vomeronasal neurons. In *Methods in molecular biology (Clifton, N.J.)*, volume 1068, pages 201–10. January 2013.

[110] Junichiro Yonekura and Mineto Yokoi. Conditional genetic labeling of mitral cells of the mouse accessory olfactory bulb to visualize the organization of their apical dendritic tufts. *Molecular and cellular neurosciences*, 37(4):708–18, April 2008.

[111] Benjamin D Young, Andreas Keller, and David Rosenthal. Quality-space theory in olfaction. *Frontiers in psychology*, 5(January):1, January 2014.

[112] T. Young. Outlines of Experiments and Inquiries Respecting Sound and Light. By Thomas Young, M. D. F. R. S. In a Letter to Edward Whitaker Gray, M. D. Sec. R. S. *Philosophical Transactions of the Royal Society of London*, 90:106–150, January 1800.

[113] T. Young. The Bakerian Lecture: On the Mechanism of the Eye. *Philosophical Transactions of the Royal Society of London*, 91(January):23–88, January 1801.

[114] T. Young. An Account of Some Cases of the Production of Colours, not Hitherto Described. *Philosophical Transactions of the Royal Society of London*, 92(January):387–397, January 1802.

[115] T. Young. The Bakerian Lecture: On the Theory of Light and Colours. *Philosophical Transactions of the Royal Society of London*, 92(January):12–48, January 1802.

[116] Hatim A Zariwala, Bart G Borghuis, Tycho M Hoogland, Linda Madisen, Lin Tian, Chris I De Zeeuw, Hongkui Zeng, Loren L Looger, Karel Svoboda, and Tsai-Wen Chen. A Cre-dependent GCaMP3 reporter mouse for neuronal imaging in vivo. *The Journal of neuroscience : the official journal of the Society for Neuroscience*, 32(9):3131–41, February 2012.

[117] Wen Zhou, Xiaoying Yang, Kepu Chen, Peng Cai, Sheng He, and Yi Jiang. Chemosensory communication of gender through two human steroids in a sexually dimorphic manner. *Current biology : CB*, 24(10):1091–5, May 2014.

Appendix

Supplemental Method: Image flow and Laplacian Edge Weighting

The segmentation of volumetric neurobiological data for analysis is a necessary task in most imaging based datasets. Regardless of the methodology (such as time or activity correlations, cosine similarity, or magnitude similarity), the characteristics of the data sets can give rise to spurious results. In this case we were investigating chemosensory imaging data characterized by both volume and stimulus dimensions (3 spatial + 21 stimulus dimensions after temporal collapse), and we describe efforts to minimize erroneous lumping of obviously different regions within this high dimensional neurobiological data.

Most methods of segmenting volumetric neurobiological data (such as cosine similarity, magnitude similarity, and correlation) have inherent assumptions that require careful control. In order to best segment the neuronal responses into ROIs, we utilized two segmentation algorithms. We utilized a magnitude similarity (n-dimensional dot product) to flow or assign voxels towards the peak magnitude similarity. Magnitude similarity, like other correlation metrics, does not explicitly address edge features. The Laplacian of the magnitude similarity captured n-dimensional edges. Weighting the magnitude similarity metric allowed further segmentation of correlated yet distinct regions with distinct response properties.

Adjacent glomerular volumes in the AOBs, similarly to many sensory regions, can have over lapping yet distinct patterns of responses to a given set of stimuli. Volumetric level image analyses

require segmenting the image volume into Regions of Interest (ROIs) that have similar response properties within the 3-dimensional image volume. In theory, adjacent volumes (either ROIs or individual voxels) can be highly correlated, uncorrelated, or anti-correlated. In the mouse AOB, we observed each of these relationships in adjacent ROIs while recording changes in axonal calcium levels (as recorded by GCaMP2 fluorescence).

While analysis must be done in three dimensional Euclidean space, the high dimensionality of sensory space is an additional consideration. One approach is to consider how that sensory space changes over physical space. The Laplacian operator is defined as the divergence of the gradient(s) of a function, here a series of 3D images I(x), in Euclidean space.

Magnitude similarity image flow is accomplished by calculating the dot product of the each voxel with itself and each of the possible 26 neighbors and assigning the voxel accordingly. In this way, the assignments flow toward the point of maximum magnitude similarity cross all stimulus dimensions. So that for n-dimensional image vectors defined over space, $I(x)$, there is an assignment image $\tilde{I}(x)$ such that the n-dimensional vector dot product with the uphill assignment vector equals or exceeds those in the 27 voxel local neighborhood and thus maximizing the magnitude similarity θ.

$$
\begin{aligned}
\forall \text{I(i,j,k)} \qquad I(x,y,z)\cdot I(i,j,k) &\equiv \mathbf{u}\cdot\mathbf{v} \\
&= \|\mathbf{u}\|\,\|\mathbf{u}\|\cos\theta \\
\exists \mathbf{t} \qquad &= I\left(x,y,z\right)\begin{cases} x & \in \{i, i\pm 1\} \\ y & \in \{j, j\pm 1\} \\ z & \in \{k, k\pm 1\} \end{cases} \\
\ni I\left(\tilde{I}(i,j,k)\right)\cdot I\left(i,j,k\right) &= \mathbf{t}\cdot\mathbf{v} \\
&\geqq \mathbf{u}\cdot\mathbf{v}
\end{aligned}
\tag{5.0.1}
$$

$$\forall \tilde{I}(i,j,k) \tag{5.0.2}$$

$$\begin{aligned} \int_{i,j,k} \max\left(I(i,j,k) \cdot I(x,y,z)\right) &\leqq I(\tilde{I}(i,j,k)) \cdot I(i,j,k) \\ I(\tilde{I}(i,j,kz)) \cdot I(i,j,k) &= \|\mathbf{t}\| \, \|\mathbf{u}\| \cos\theta \begin{cases} i & \in \{i, x \pm 1\} \\ j & \in \{y, y \pm 1\} \\ k & \in \{z, z \pm 1\} \end{cases} \end{aligned}$$

Each region is defined as having assignments flowing to the same maxima. This assignment is easily accomplished in our data sets by creating a matrix of double precision values to identify each voxel, and then iterating over the voxels granting to each the value of that voxel (self or other-wise) which holds to equation 5.0.1 until it reaches a fixed solution to equation 5.0.2.

Edge weighting requires an intervening process in which the stimulus response dimensions are weighted in regions in which the second spatial derivative has a zero crossing. In order for the estimates of the calculating the spatial gradients of each stimulus response dimension composing the magnitude similarity. The estimate is calculated along 13 axes because image flowing (see diagram, hot colors represent greater magnitude) occurs along all possible 26 adjacent cube points. As the dot product is a between points metric, we use a forward derivative kernel in 13 of the 26 to estimate the gradient followed by a centered derivative kernel.

Given that the general shapes of the regions under consideration are geometrically convex (in other words they are closed shapes in the spatial sense), there are conditions under which even sharp edges might generate overlapping values. For example, we expect that when the edges are "close" the negative values from multiple edges may overlap in the center of a small sphere. These "close" circumstances would occur when the radius of the sphere is of about the same size as the smoothing kernel. Additionally, if the the sphere was actually hollow, such as a cell with fluorophore in the cytoplasm, the diminishing fluorescence would be a source of negative second derivative values.

There is a tradeoff between detecting edges and image flowing. This trade-off is smallest when the regions, for example cells, are of homogeneous size and both the edge signals from the cell cytoplasm and nucleus overlap. Even in this circumstance, there are cases where blurring in some part of the data may not give a real edge between cells. In this case, we may observe multiple partial correlations in our response dimensions across some number of neighboring cells. Even then in the case where our desired regions of interest (ROIS) have "real" edges and are of relatively homogenous size, they may flow together and defeat our simple algorithm.

It is desirable then to have edges detected in one dimension have an effect on other dimensions, so that if we utilize information about the sparseness of a spatial region without creating absolute stochastic edges as might happen if we just aggregated all "edges" across some large dimensional response space. Not only would we want to avoid absolute values or penalties, but even very large penalties could result in over-segmentation of areas.

To accomplish this, we sum the absolute values of the directional second derivatives. We used all directions, weighted by the pair-wise distances between center and surrounding voxels, because as described above imflow tested all adjacent voxels rather than just the three orthogonal axes. This total magnitude will be a normalizing value.

$$\nabla^2 I(j) = \left(\frac{d^2 I(j)}{d^2 x} + \frac{d^2 I(j)}{d^2 y} + \frac{d^2 I(j)}{d^2 z} \right)$$

Each stimulus dimension during imflow is weighted as follows, such that a modified image is subjected to imflow. Each stimulus dimension Laplacian is normalized over six standard deviations, such that all values less than -6σ are set to negative one and all values greater $+6\sigma$ are set to one. The three dimensional sum of the magnitudes of these normalized Laplacian matrice $L_{normMMag} = \frac{1}{stims} \sum_{k=1}^{stims} \|L(j)_{norm}\|$ is subsequently used as a factor in the final weighting of image to be flown $I(j)_w = I(j) \cdot (1 - L(j)_{norm} \cdot L(j)_{normMag})$. The result of which is an emphasis of the curvatures, effectively unweighting the edges along each dimension of the image to flow by magnitude correlation. This modification is sufficient to allow many smaller peaks in one or two dimensions to avoid being pulled by partial correlations with a large adjacent region.